Repeatability of joint-dominated deployable masts

Thesis by

Olive R. Stohlman

In Partial Fulfillment of the Requirements

for the Degree of

Doctor of Philosophy

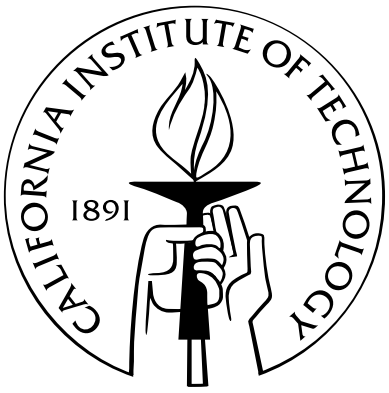

California Institute of Technology

Pasadena, California

2011

(Defended April 20, 2011)

To my grandparents, who have supported my education unconditionally.

Acknowledgements

The guidance of my thesis advisor, Prof. Sergio Pellegrino, must be acknowledged first and foremost.

Thanks to my parents and brothers.

The Jet Propulsion Laboratory provided the sample mast that made this work possible. Fiona Harrison and Yunjin Kim are gratefully acknowledged for involving the Space Structures Laboratory in the NuSTAR project.

The GALCIT machine shop, John Van Deusen of the mechanical engineering shop, S. Case Bradford, and Maen Alkhader made essential contributions to the experimental work of this thesis.

I must note the use of Daniel M. Zimmerman's Caltech thesis formatting class, Norman Gray's `textpos` package, and Till Tantou's fantastic documentation of TikZ & PGF. Special thanks to Paco López Jiménez and Vincent Zeng for their help in editing this thesis.

Dr. Dan Harris of the Harvard-Smithsonian Center for Astrophysics and Prof. John Krupczak of Hope College have continued to encourage my academic aspirations long after I left my summer internships. My advisor and mentor from Carnegie Mellon University, Prof. Stephen Garoff, introduced me to laboratory work at Carnegie Mellon's Interfacial Physics Laboratory.

Matt Longnecker showed me that I could operate a power tool and still hope to come away with all my fingers. Without my teammates and seniors from buggy—especially (but far from exclusively) Sonia Balsky, Shafeeq Sinnamohideen, Shandor Dektor, Justin Burstein, and Sean Kelly—I would never have gained the confidence to make foolish errors or reach for success in design.

Without the early encouragement of my algebra teacher, Mr. Ohlson, none of my academic success would have been possible. I cannot sufficiently express my gratitude for the kindness and dedication shown by teachers throughout my time in school, and Mr. Ohlson's impact on my life has been immeasurable.

Abstract

Deployable masts are a class of structure that can be stowed in a small volume and expanded into long, slender, and stable booms. Their greatest benefit as space structures is their packing ratio: masts can typically be packed to a fraction of their deployed length at a diameter only modestly wider than their deployed width. This thesis is concerned with precision deployable masts, which can be stowed and deployed with repeatability of the tip position of better than 1 mm over 60 m. The methods of investigation are experimental measurements of a sample mast and numerical modeling of the mast with specially attention to hysteretic joints.

A test article of an ADAM mast was used for the experimental work. Two categories of experiment were pursued: measurements of mast components as inputs to the model, and measurements of full bays as validation cases for the model. Measurements of the longeron ball end joint friction, cable preload, and latch behavior are of particular note, and were evaluated for their variability. Further measurements were made of a bay in torsion and a short two-bay mast in shear, showing that there is residual displacement in this mast after shear loading is applied and released.

The modeling approach is described in detail, with attention to the treatment of the mast latches, which lock the structure in its deployed configuration. A user element subroutine was used within the framework of the Abaqus finite element analysis solver to model the behavior of the latches with high fidelity.

Validation cases for the model are presented in comparison with experimental observations of a two-bay mast. These cases show that the model captures a number of important and complex nonlinear effects of the hysteretic mast components. Parametric studies of the impacts of component behaviors and modeling practices are explored, emphasizing the impacts of part variability and the idealization of the mast latching mechanisms.

Contents

List of Figures

List of Tables

Chapter 1

Introduction

Deployable masts are a class of structures that can be stowed in a small volume and expanded into long, slender, and stable booms. Their greatest benefit as space structures is their packing ratio: masts can typically be packed to under 5% of their deployed length[1]. This thesis is concerned with precision deployable masts, which can be stowed and deployed with repeatability of the tip position of better than 1 mm over 60 m. Whether or not repeatability of hundreds of microns over tens of meters is adequate depends, of course, on the application.

Figure 1.1: Artist's depiction of the Shuttle Radar Topography mission above the earth (NASA image [33]). A mast was used to deploy and stabilize the outboard antenna (foreground) at a distance of 60 m from the orbiter.

A prominent high-precision application is in telescopes, where optical parts must be kept at a reliable distance from the telescope detector. The limitations of the optical system often demand a very long focal length, and the limitations on the size of the detector and the depth of focus demand excellent alignment of the two bodies. At the same time, the volume and mass of the complete

spacecraft drives the cost of the launch vehicle. Masts with position control systems and mastless formation flying systems are possible, but every added level of complexity is a potential point of failure and drives up the risk, cost, and power consumption of the mission. Precision deployable masts are often, therefore, the technology of choice for telescopes and other very long spacecraft.

As focusing optics, light collection area, and detector quality improve, the precision of a telescope mast must also improve. The depth of focus—that is, the region in which the detector must be located to produce a well-focused image—is inversely proportional to the resolution of the system; if the density of pixels at the focal plane increases by a factor of two, the range of focal distances that allow an unblurred image decreases by half. At the time of this writing, the only high-precision telescope application of a deployable mast is the upcoming NuSTAR mission, which will require no ongoing focus adjustment [28], despite anticipated thermal extension of the mast of as much as millimeters over its 10-m length.

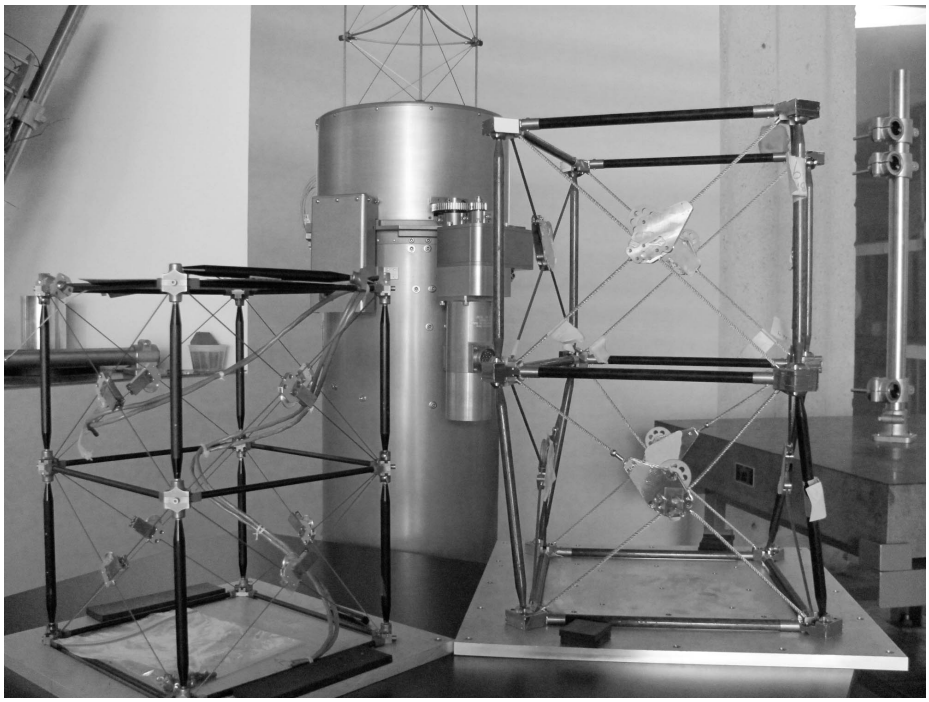

Figure 1.2: Deployable masts in the Space Structures Laboratory at Caltech, from left to right: two bays of the WSOA sample mast; Coilable boom in canister; two partially deployed bays of IPEX-II.

Mast designs range from telescoping poles to coilable trusses. The design that this study will focus on is patented by Able Engineering and called ADAM. Two example of this mast design are shown in Figure 1.2. ADAM is a mast design of special interest because it has been used as a precision element in multiple space missions. It is lighter than a telescoping design of equivalent stiffness

and requires less volume than a coilable truss of equivalent stiffness. However, its heavily jointed design raises the possibility of complex friction effects. How reliable is a joint-dominated structure in precision applications, and what design factors impact friction behavior? These questions have guided this research, and their answers will drive design decisions in large and precise formation structures of the future.

1.1 Motivation and goals

Tip position is the fundamental measurement of a deployable mast's performance. This is the position, in six degrees of freedom, of the outboard tip of the mast relative to the base. A given mission will often have particular requirements that the tip position must meet: it must be known to a certain precision at crucial moments in the mission, and it must fall within a certain range during operations. McEachen [31] describes the qualification testing of a deployable mast, which includes modeling of a variety of sources of tip position error. One such source is the cumulative errors of joint misalignments along the structure, a subject of focus in this thesis.

There are many sources of variation in a mast's tip position. Dynamic effects are their own complete area of study, but even within that field, complete static and quasi-static characterization of a mast may be required to avoid exciting resonant modes during use. Static position errors are dominated by thermal effects, which are present in every type of mast; they are not a special concern of joint-dominated masts. Secondary to thermal distortions are mechanical sources of static position error. Aside from catastrophic mechanical failures, the mechanical sources of change in the tip position are history-dependent material properties and history-dependent interfaces. As with thermal distortions, all masts are similarly subject to material plasticity, strain hardening, and cyclic damage. It is joint-dominated masts in particular that are subject to friction and other interface effects.

While a mast could be composed of unique parts (and some low-aspect-ratio and telescoping masts are), most slender space masts are based on modular designs. This means that they contain many nominally identical parts, and those parts will have a certain spread in their properties. With many properties, this sort of spread is not consequential; the effect is often very small, or averaged out over many bays, or revealed and accounted for after ground testing. It is not obvious, however, that this is true of *every* stochastic property of mast parts.

Two effects, joint-driven hysteresis and the impact of stochastic part properties, are the subjects of this study. They are concerns characteristic of modular, joint-dominated structures, and under-

standing the magnitude of their impact on mast performance is the broad goal of this work. More specifically, this thesis will characterize the impact of hysteretic parts and stochastic properties on the linearity and hysteresis of a mast under transient quasi-static load. The framework for this characterization will be applicable to a range of mast designs beyond the particular ADAM mast of this study.

1.2 Approach

The approach of this study is rooted in experiment and modeling. The ultimate product is a framework for modeling a mast with stochastic properties, friction, preloaded cables, and nonlinear part response. The computational model presented here is valid for large displacements, including those displacements that engage the nonlinear effects of the deployment locking mechanism. Joint-driven hysteresis will be addressed through measurements and modelings of two key parts: the longeron joints and the locking mechanism. The effects of stochastic part properties will be addressed through measurements of these two parts and the cable preload.

Two types of experiments are needed to build a mast model: part characterization and mast characterization. Part characterization is the measurement of the properties of individual components, such as the spring stiffness of the diagonal cables. The part characterizations presented here focuses on hysteretic and stochastic properties, in keeping with the study goals. In particular, longeron joints, cable preload, and the complex constitutive relationship of the latch were characterized for both their average behaviors and the variability between parts.

Mast characterization comprises measurements of the behavior of an assembled mast of one or more bays. These measurements are essential to the model validation. Two levels of mast motion were measured: a stow-and-deploy cycle that covered a bay's deployment path, and shear loading of a short two-bay mast. The shear loading results explore the possibilities for tip displacement during use.

Standard commercial software was used as the backbone of the numerical model, but the most important nonlinear and stochastic part properties required special programming. To perform parametric or Monte Carlo studies with randomly generated properties, the mast model must be generated from a database of possible part properties and their distributions. The mathematics software Matlab was used to manage this database and create input files for the finite element solver Abaqus. The most complex moving part, the reversible deployment locking mechanism, is the subject of a special subroutine within the finite element model, allowing complete control over its nonlinear and

hysteretic behavior.

The marriage of detailed characterization of the mast as it is and extensive control over the modeled mast makes it possible to investigate which properties of the mast govern its performance. Analyzing a mast at this level of detail may establish a high degree of confidence in its future behavior and focus design and manufacturing effort on the areas of greatest impact.

1.3 Outline

The remainder of this thesis is organized as follows.

In Chapter 2, the literature on deployable masts and jointed trusses is reviewed. The second part of the background section introduces the particular mast that is the subject of this work.

Chapters 3 and 4 describe two categories of experiment: measurements of mast parts as inputs to the model, and measurements of full bays as validation cases for the model. Chapter 3 deals with the experimental properties of mast parts, specifically measurements of the longeron ball end joint friction, cable preload, and latch behavior. Chapter 4 presents measurements of a bay in torsion and a short two-bay mast in shear.

The modeling methods are overviewed in Chapter 5, with a detailed description of the most important elements. The model of the bay locking mechanism is addressed.

Chapter 6 includes a selection of parametric studies. The parametric studies are focused on the case of a two-bay mast in shear, as in the experiments of Chapter 4.

The validation of the model is presented in Chapter 7, returning to the experimental measurements of Chapter 4.

Finally, Chapter 8 discusses the results of the preceding sections.

Chapter 2

Background

This chapter begins with a literature review which addresses a number of studies of trusses, deployable masts, and joint-dominated structures, including the influences of realistic moving joints and the space environment. Particular masts have been characterized through a number of experimental methods. Important tools for laboratory and in-flight mast characterization include laser rangefinding and videogrammetry, and masts of varying levels of precision and stiffness have been addressed. Studies and missions using the ADAM mast are presented in Section 2.4.1.

2.1 Analysis of trusses and deployable masts

Trusses are a classical topic in mechanics, addressed at length by Timoshenko and Young [48] and others. A deployable jointed truss is first idealized as a pin-jointed truss. This idealization provides a first pass at the stiffness of the mast, and can give a starting point for the required range of material stiffnesses and member lengths that an application will demand. Other researchers have extended this analytical approach to include advanced beam theory, including port-buckling behavior (e.g., Peek and Triantafyllidis [35]).

Many precision deployable masts feature a foldable skeleton of stiff beams. A system of cables or thinner beams is then used to triangulate the structure, eliminating internal degrees of freedom of the mast. The mechanisms of the skeleton are of interest because they will define the softest deformations of the rigidized mast. As demonstrated by Pellegrino [37], the mechanisms and states of self-stress of a truss can be found by singular value decomposition of the equilibrium matrix that relates element stress resultants to external nodal forces. Kwan and Pellegrino [24] presented a matrix treatment of masts and structures without the limitation of pin joints, and also integrated active cable deployment and the effects of preloaded cables.

Within the limitations of linear analysis, there are some basic design parameters that can be identified (or at least bounded) analytically. Greschik [15] describes some of the concerns that arise when rigid elements of a truss are replaced with cables. In particular, it is noted that the cable should be preloaded to at least the maximum stress of the theoretical member it replaces. This also implies that "for a tendon to be used in lieu of a strut, its extreme load after sufficient pretensioning will be at least twice that associated with an equivalent strut with no prestress applied."[15, p. 559]' This observation highlights the importance of accurately assessing any nonlinearities in the cable behavior that might appear at high loads. Greschik also notes that asymetric prestressed elements can cause shape eccentricity in an otherwise unstressed truss. This shape eccentricity may go on to impact the stiffness of the structure, essentially prebuckling the previously straight line of longerons.

Tan and Pellegrino [47] presented a computational analysis of a pantographic mast. The finite element package ABAQUS was used, with beam elements rather than a detailed solid model. They followed this up with a custom Matlab model, using Guyan reduction to produce a manageably sized model for correlation studies. Results from the Matlab model, which used linear properties for all components, are instructive:

> According to [the Matlab model], increasing the active cable pretension has the effect of softening the mast, and the reduction in natural frequencies is approximately linear with the active cable tension. However, experiments had shown the opposite effect and hence it can be concluded that to properly simulate the actual behavior of the model structure it is necessary to consider the effects of the component nonlinearities on the overall vibration behavior.[47]

Using equivalent stiffness matrices to model the nonlinear behavior of the joint friction, a new iterative matrix model is presented. The authors reported that the method of equivalent stiffnesses and an iterative treatment to match the linear matrices to the nonlinear joint behavior produces a simulation "300 times faster than a full nonlinear simulation." Ultimately, this model showed good agreement with the experimental peak frequencies and damping factors. Predicted and observed values were within 1-2%, and damping factors generally identified to 20-30%. The full-spectrum response of the system was reproduced to only a modest degree. This paper shows that limited computing resources can model a nonlinear system that has been very carefully characterized.

2.2 Effects of materials and joints

To improve the level of accuracy in predictive modeling of a mast, thermal and micromechanical effects must be included. Thermal expansion can be quite significant, and is a driver of material selection, motivating efforts to match the expansion of metal joints with the contraction of composite members. Kegg [22] describes materials selection that balances graphite rods with metal joints for a low net coefficient of thermal expansion in a deployable mast of the FASTMast design [3]. The negative coefficient of thermal expansion (CTE) of P75 graphite epoxy, at $-1 \times 10^{-6}/°\text{C}$, was balanced against the positive coefficient of $8.3 \times 10^{-6}/°\text{C}$ in the titanium joints. When some additional connecting parts were made of ultra-low-CTE Invar, the total mast was able to achieve a CTE of $0.68 \times 10^{-6}/°\text{C}$. Using parts with such mixed properties raises questions of bond strength, also addressed by Kegg. A broad review of stability in space structures has been presented by Edeson et al. [11] and includes a great deal of information on the choice of materials for reliability on the space environment, among other topics.

While thermal effects are an essential area of study for space structures, this thesis will focus on the mechanical sources of error that arise from friction, which affect every stage of mast function. It is occasionally possible ameliorate the effects of friction in the joints by designing solid-state hinges, which have their own limitations. Tape-spring hinges are often quite nonlinear in their behavior [41, 29] and may suffer from the stresses of long-term storage [25]. Tape-spring-based booms are increasingly widely used and well-developed [46], constituting their own class of deployable mast; the applications of these very lightweight masts generally have different demands from the applications for joint-dominated masts. In heavily jointed structures, hysteresis in deployment results in an unpredictable final deployed configuration, especially if gravity has an effect on the hysteretic behavior. This severity of the difference between the expected and realized shapes is compounded if the hysteresis produces an identical error in every joint. ADAM booms, for example, are designed so that its bays are deployed in alternating directions, in the hopes that this will cause deployment errors to cancel one another over the length of the mast. Once a mast is deployed, its resonant frequency and damping factors depend upon friction. The magnitude of friction forces will again depend on gravity and the preload in joints.

Folkman et al. [14] demonstrated dramatic effects of gravity and joint play on the behavior of a jointed trust in a twang test. They found that, in a loosely jointed structure, “damping rates can change by a factor of 2-5 as a result of simply changing the orientation of a truss” with respect to gravity. Folkman et al. also found that unlocked joints greatly increase the damping in a structure,

presumably through frictional losses. These qualitative observations make it clear that the direction and presence of gravity can be an essential factor in the behavior of a truss, especially the dynamic behavior of a truss without preloaded joints, where the force in the joint due to gravity is much more substantial than loads internal to the truss. Beyond the effects of gravity, many space-qualified lubricants behave differently depending on the atmosphere in which they are tested. For example, Fleischauer [13] described the complications of testing with the solid lubricant molybdenum disulfide, which is sensitive to moisture, asserting that "It is imperative that ground testing and storage of devices lubricated with MoS_2 films be effected in a protected environment, either vacuum or inert gas." The lifetime of a spacecraft with fluid lubricants can be limited by the time it takes for them to escape under vacuum, inviting sealed joint designs that increase the complexity of the spacecraft.

Despite the significance of friction in jointed structures, advanced tribology is not generally applied to their analysis. Generally, the only forms of friction considered are Coulomb friction and viscous damping. Warren et al. [50] consider an analytical model of a latching joint with a simple deadband. They concluded that "this modeled behavior replicates not only the magnitude of the lurches that were observed in the experiments, but also the convergence rate observed in the data." However, the analytical model was one-dimensional, and thus of only limited relevance to the study's small deployable structure. Advanced treatments of tribology demand a computational approach and detailed characterization of moving parts.

Friction is a leading source of unpredictable behavior in the transition from the ground to orbit. Friction, in combination with thermal expansion, is known to cause transient motion. This phenomenon, known as "thermal snap," occurs when two surfaces are held in static friction and thermal expansion overwhelms the frictional force. As a joint is suddenly released from static friction and then resticks in a new position, it shows an acceleration profile with an impulsive start and damped harmonic ringing. Thermal snap has been produced in a laboratory setting [21], and was studied in orbit with the IPEX-II boom. IPEX-II identified transient thermal snaps as causing accelerations around 120 μg at a frequency around 50 Hz [27, p. 4].

Thermal expansion may be predicted with detailed finite element models and manufacturing defects can be measured after manufacture and, therefore, can be accounted for. In contrast, tribology and friction can be severely impacted by the transition to the space environment (which changes lubricant properties[13] and joint load[14] at the same time). These many factors conspire against a complete treatment of high-precision jointed structures. Any study that wishes to include frictional effects requires a full experimental characterization of the particular joints used in a structure.

Chapman [6] included modal response data of joints and struts with nonlinear behaviors, including free play and hysteresis in joints, in a numerical model for a mast. This complex model, based on detailed experimental characterization of the damping factors and other behaviors of many mast components, produced good agreement with experimental characterization. Subsequent work has been done [7] to better integrate for the many effects of joints on the dynamic responses of joint-dominates structures. Lake et al. [26] presented a summary of a number of concerns relevant to large deployable structures with an eye to stability and microdynamics, common theme in the study of precision and joint-dominated deployable structures.

2.3 Metrology and experimental methods

Experiments on actual flight articles are a necessary pre-flight confirmation of their quality. Ground testing equipment may be required to approach the sensitivity of telescope optics to measure any structural effect that would impact the optical configuration. Sometimes, this requirement can be avoided; the NuSTAR telescope will be launched with a one-time adjustment motor [19], which will slightly reposition the optics to account for errors in the ADAM mast that separates the optics bench and the detectors. An adjustment mechanism like this motor relaxes the mast repeatability requirements, but adds an additional critical, powered, moving part.

Laser distance measurements and MEMS accelerometers are common methods for high-precision experimental observations. Accelerometers can generally only be applied to frequency studies; direct measurements of displacement are preferred for static tests. Lasers have a limited range of detection, so larger motion has often been measured through photogrammetry. Photo- and videogrammetry compare the locations of particular markers on a structure as they move. For complete force-response data, force transducers and shakers are combined with these measurements of the structure position or acceleration response.

2.3.1 Lasers

Laser rangefinders can be used for distance measurements and are a tool of choice for measuring the final deployed length of a boom. A modified off-the-shelf rangefinder was used to monitor the axial motion of the 60-m mast of the Shuttle Radar Topography mission with a precision of approximately 1 mm at a rate of 0.2 Hz [10].

Lasers will also be used, alongside a star tracker, in the NuSTAR metrology system. This

configuration is described by Liebe et al. [28]. The metrology system will determine the position of the mast tip in three degrees of freedom using a set of two lasers and two position sensitive detectors. The lasers are fastened to the outboard tip of the mast, and aimed at detectors on the main spacecraft bus. By reading the position of the laser dots at a rate above the major natural frequencies of the mast, the metrology system will provide crucial data about the pointing of the mast at all times during observation. Because the x-ray detectors record the time and impact position of each incoming photon, the reconstructed images can be corrected to account for motion of the mast tip, even if vibrational modes of the mast are excited during observation. These corrections will allow the system to achieve a resolution that would otherwise demand exceptionally stable pointing of the 10-m mast.

2.3.2 Photogrammetry and videogrammetry

SRTM[9] and the ST8 SAILMAST[32] experiment both made use of photogrammetry. Both of these systems consisted of a "constellation" of LED lights and a camera. In the case of SRTM, a modified star tracker (an Advanced Stellar and Target Reference Optical Sensor) was used to reduce the quantity of output data. The star tracker's internal software reduces the amount of information output from a full-field image to a set of point locations.

It is generally possible to get sub-pixel resolution of the position of a bright point target with photogrammetry. Generally, this is done by slightly defocusing the camera so that each point is spread over a number of pixels. Then, the center of the circle this forms can be found to precision finer than the size of a pixel. This means that a camera need only have a moderate resolution for modest precision goals. For example, McEachen et al. [32] used a 720 x 576-pixel PAL-video CCD camera and achieved <2 mm resolution at a 40-m distance.

2.3.3 Other methods

Accelerometers were the primary tool of the Interferometry Program Experiment II (IPEX-II), and used in previous investigations of thermal snap [20]. In this experiment, an ADAM mast was observed in the space environment under various thermal and vibrational loads. IPEX-II was mounted on ASTRO-SPAS, a free-floating experimental platform, so it was free of major dynamic loads and subject only to intentional loading, thermal loading, and the motion of the data recording tape drives. Accelerometers have also been used for regular modal analysis, as in [14] and [47].

Very advanced gravity offload systems are associated with dynamic and large-deformation studies.

Greschik and Belvin [16] proposed a system of fly beams to support large structures during dynamic testing with minimal disturbance to the vibrational mode shapes.

2.4 ADAM mast

Proposed mast geometries and packing methods are quite diverse. Mast designs can be distinguished from one another by their deployment method and the deformations that the bays undergo during stowage and deployment. Partially and fully strain-energy-deployed masts exist in a number of geometries, and include FASTMast [3], Coilable [2], the MARSIS antenna [30], and Astromast [12]. Aside from the jointed FASTMast, these designs all feature some type of continuous longitudinal members or solid strain-deformable hinges. Another class of deployable masts requires entirely powered deployment, often working against strain energy in parts that will be provide preload in the deployed state. ADAM is one such mast, and perhaps the most prominent in space applications.

The ADAM mast is a deployable truss structure, patented in 1993 [8]. It has since been used in a number of space missions and studies. The design is modular and jointed. ADAM must be deployed from a motorized canister and includes a reversible locking mechanism on each face of each bay. Each bay locks independently, allowing the mast to be deployed one or two bays at a time. Because the bays are jointed, the longerons can be relatively wide and stiff, unlike the deformable longerons of a Coilable [2] or Astromast [12], achieving a given stiffness in a container of smaller radius than a continuous-longeron mast. The ADAM design can be understood as a deformable box-shaped structure of stiff members, shaped and rigidized by cables and an integrated latching system.

Definitions of terms A number of terms will be used to describe parts and subassemblies of an ADAM mast. They are described hierarchichally in Figure 2.1.

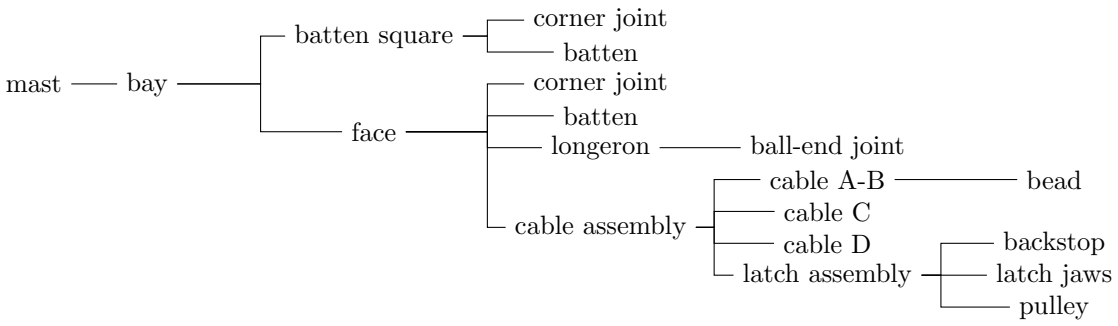

Figure 2.1: Hierarchy of mast subsystems and parts.

This hierarchy is further illustrated in Figures 2.2, 2.3, and 2.5. The mast is composed of repeating bays, with longerons in the axial direction and battens providing perpendicular spacing. Diagonal cables A, B, C, and D on each face carry tension when the mast is fully deployed.

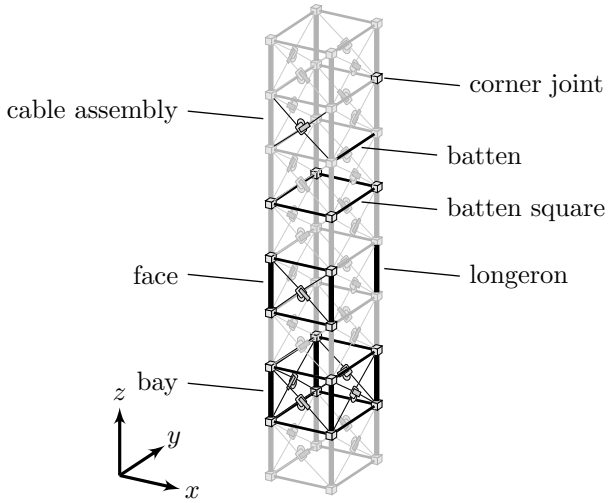

Figure 2.2: Definition of terms on the mast. Note that latch orientations alternate with each bay.

The cable assemblies contain the passive reversible latching mechanism that allows powered deployment and retraction of the mast. As shown in Figure 2.3, a bead is fixed to cable A-B, which runs over a pulley in the latch assembly. A photograph of these parts is shown in Figure 2.4. When this bead is locked in the latch jaws, the face is triangulated and cannot deform. When the bead is outside these jaws, cable A-B can flow freely over the pulley, and a parallelogram deformation, as seen in Figure 2.3b, of the face is possible.

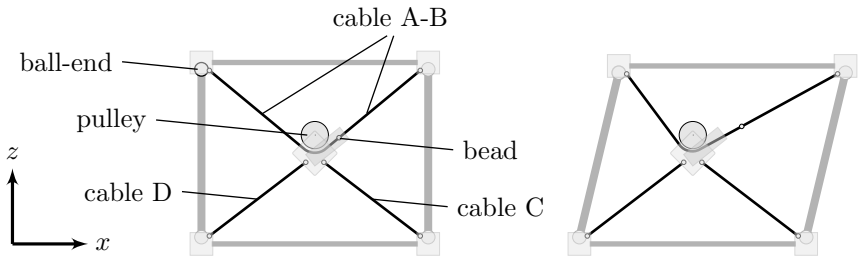

(a) (b)

Figure 2.3: Notation for a face of an ADAM mast. A latched face is shown in (a) and an unlatched deformation in (b).

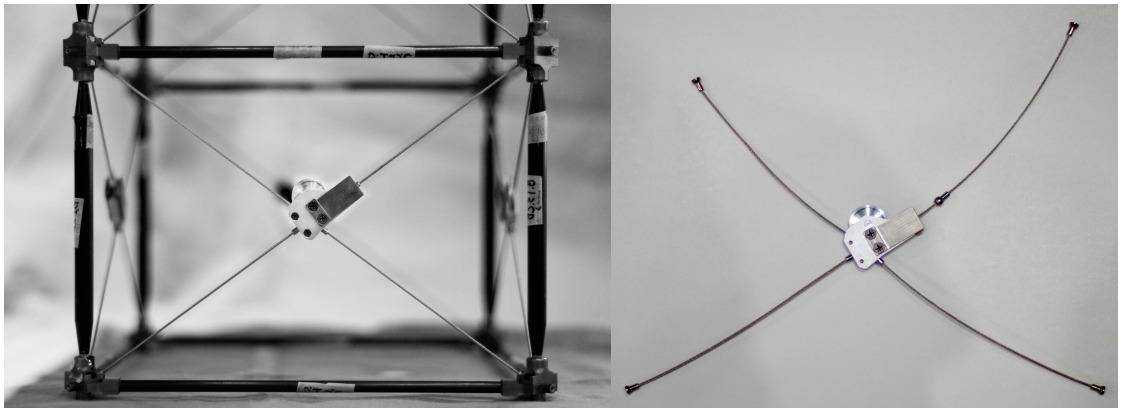

(a) (b)

Figure 2.4: Closeup of an ADAM mast bay face (a) and cable assembly (b).

When the latch assembly is viewed in detail from the side, as in Figure 2.5, the mechanism of capture is more clearly seen. While the bead is locked in the jaws, it is generally being loaded against a cone-shaped backstop by the rollers. To move in or out of the latch, the bead must be forced through the jaws by a tension difference between sections A and B of cable A-B. This relationship is examined in detail in Section 3.3 and included in the computational model of Section 5.2.

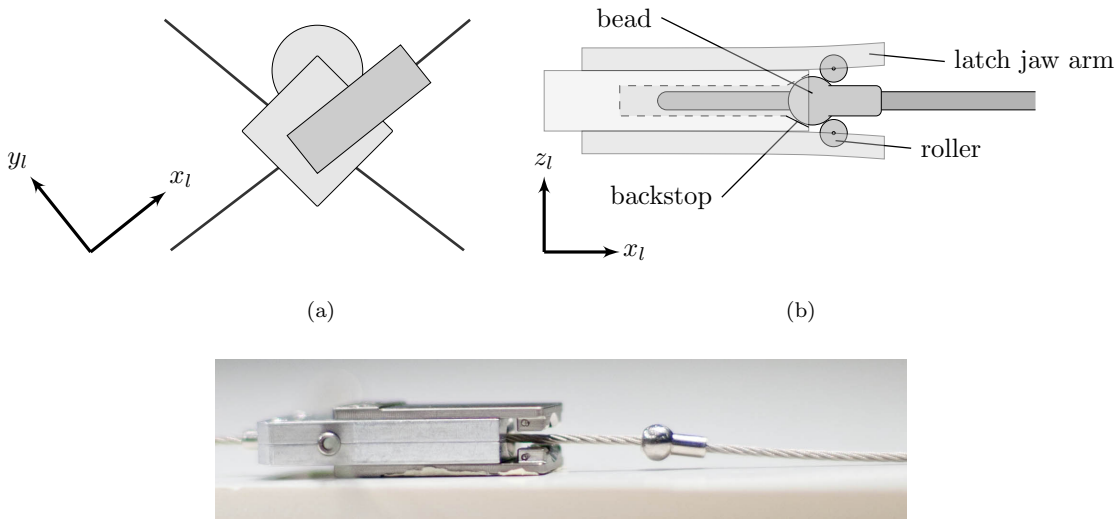

Figure 2.5: Definition of terms in the latch. Note that while in the fully latched position, seen in the side view (b), the bead is preloaded against the backstop by the rollers. A photograph of a latch from the sample WSOA mast is shown in (c).

The battens and longerons are relatively stiff members and form a box, which can deform without resistance in two ways, as shown in Figure 2.6. The ADAM mast, with its cables removed, has three mechanisms throughout most of its deployment process, which can be identified intuitively in the fully deployed state (see Section 2.4). One of these mechanisms, which deforms the bay by twisting, is used to stow the mast. Deployment is managed by the interaction of the cables and locking mechanism with this twisting motion. The cable assemblies, which triangulate each face of each bay, rigidize the structure by preventing these mechanisms. The cable assemblies include a reversible locking mechanism, allowing the bay to be packed flat through a torsional deformation.

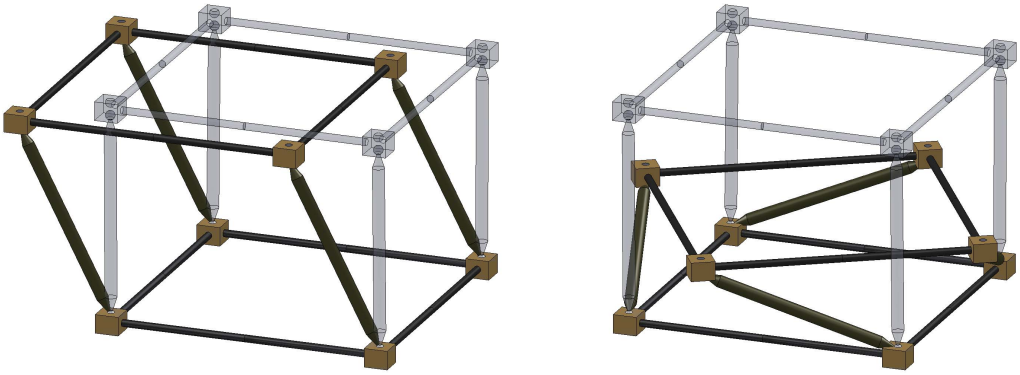

(a) Shear mechanism.

(b) Torsion mechanism.

Figure 2.6: The mechanisms of motion of a bay without diagonals. The simple shearing mechanism (a) is active in both shear directions. The torsional mechanism (b) is used to stow the bay.

Because of the different structural roles of the battens, longerons, and diagonals, the mast's resistance to bending and axial deformations is driven by the stiffness of the battens and longerons, while its resistance to torsion and shear is driven by the stiffness of the diagonals. Hence, torsional and shear motions are more likely to interact with the locking mechanisms on the cable assemblies. In extreme cases, such interactions could cause catastrophic failure of the mast by unlocking a bay side, but before that occurs, the elasticity of the mast will become nonlinear and hysteretic effects in the latch may create persisting changes in the overall shape of the mast.

All ADAM masts are deployed using motorized canisters, which deploy and lock one bay at a time, while a second bay is held partially deployed and the remainder of the mast is stowed. A deployment canister for the NuSTAR mast is shown in Figure 2.7. The stiff-soft cable system that is planned for this mission can be seen in this view; unlike the WSOA sample mast used in this study, the NuSTAR mast uses rigid members in the positions of cables B and D (defined in Figure 2.3).

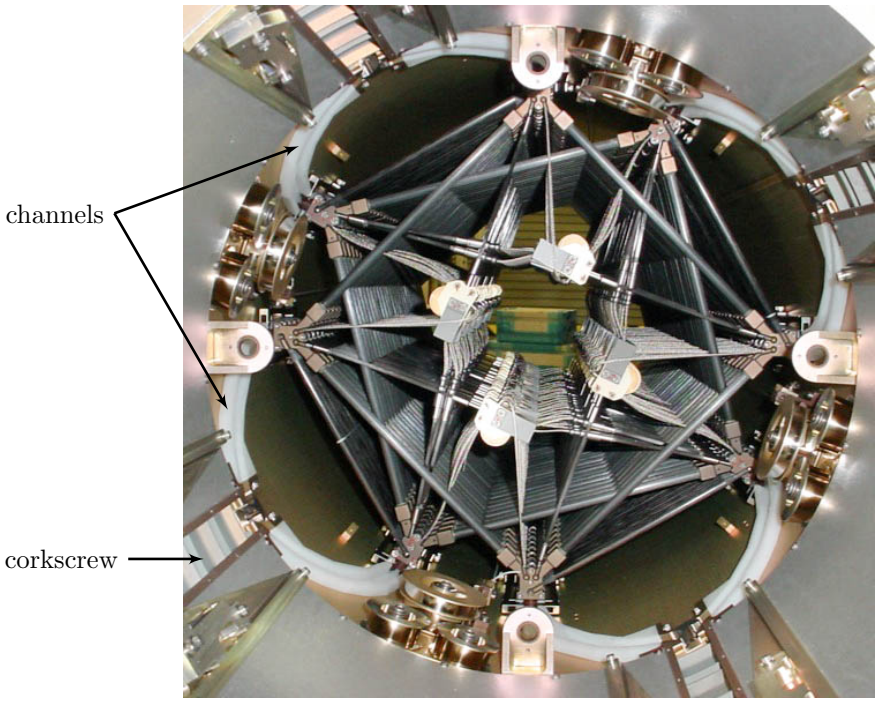

Figure 2.7: Top view of the completely stowed NuSTAR mast in its deployment canister (NASA image [5]). The corners of the top bay follow a set of white channels to the motorized corkscrew, where it continues towards full deployment while the next batten square enters the opposite set of white channels.

2.4.0.1 WSOA sample mast

The experiments were performed on a sample ADAM mast. This test article is shown in Figure 2.8. It was loaned to the Space Structures Laboratory by the Jet Propulsion Laboratory for the duration of this study, and was originally manufactured by AEC-Able of Goleta, California. It is a completely functional six-bay mast, and was used as a sample specimen for the design of the Wide Swath Ocean Altimeter (WSOA) project [38]. The Wide Swath Ocean Altimeter sample mast was originally produced as a possible design for an interferometric altitude mapping project [39]. Its dimensions are shown in Table 2.1.

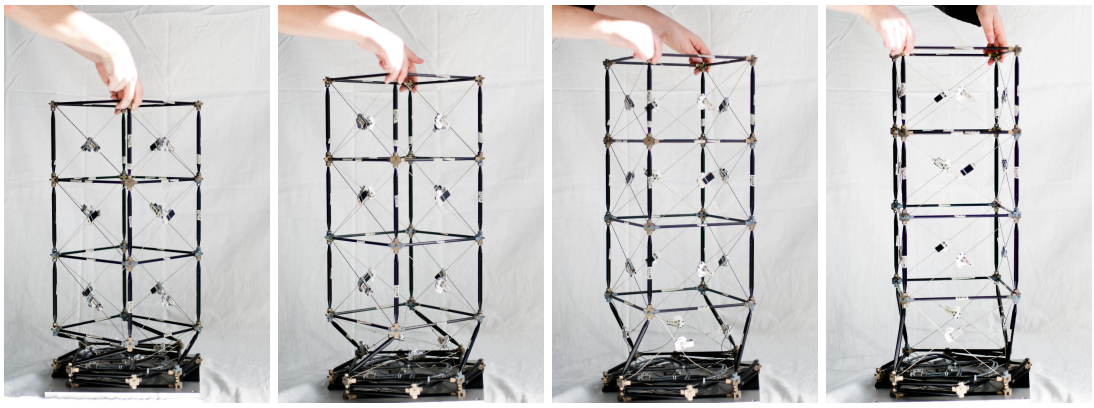

Figure 2.8: The WSOA sample mast, shown with three fully deployed bays and a single partially deployed bay.

Table 2.1: Sizes of WSOA sample mast parts.

Bay width (longeron ball end to ball end	230 mm
Bay height (center of latch to center of latch)	170 mm
Longeron length (ball end to ball end)	150 mm
Stowed height per bay	15 mm
Stowed radius (including joints)	350 mm

No engineering data about the sample mast was available, requiring initial estimates of the stiffness of parts. The battens, shown in Figure 2.9, are made of a carbon composite, which was assumed to be solid. The longerons, shown in Figure 2.10 appear to be aluminum. The longerons are taped at either ends, and each have a mass of 32 g with the end fittings, with a length of approximately 146 mm and a radius of approximately 5 mm; assuming they are made of aluminum, these dimensions give an expected mass of approximately 31 g for solid aluminum, consistent with the measured mass. Further analysis of, and adjustments to, these assumptions is presented in Section 6.1. As summarized in Table 2.2, the battens and longerons are on the order of 100 times stiffer than the cables, and hence the behavior of the sample mast is not highly sensitive to their actual stiffness values.

The magnitude of the torque required to stow or deploy the bay depends on both the strength of the latch assembly and the pre-tension and stiffness of the cables in the deployed state. In practice, the latch assembly makes a larger contribution, accounting for approximately 20 N-m of the 30 N-m torque required for deployment of the sample mast. A more detail analysis is presented in Sections 4.1 and 7.1.

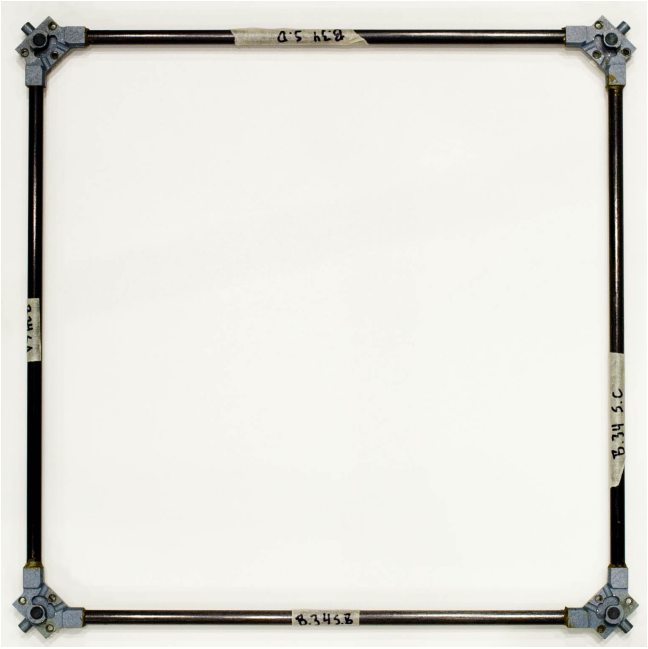

Figure 2.9: Batten square of the WSOA sample mast.

(a)

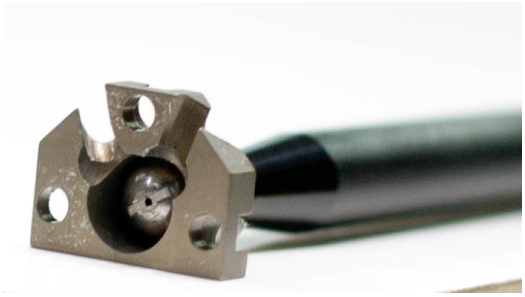

(b)

Figure 2.10: Longeron (a) and longeron ball end joint (b) of the WSOA sample mast.

Table 2.2: Characteristic stiffnesses of mast parts.

Part	Axial stiffness (kN)	Young's modulus (GPa)	Radius (mm)
Battens	6500	220[a]	3.1
Longerons	5000	70[b]	4.8
Cables	73	-	-

[a] Indirectly calibrated, see Section 6.1.1
[b] Estimated

2.4.1 Applications of ADAM

2.4.1.1 IPEX-II

IPEX-II flew on the Space Shuttle Discovery in August of 1997. Its purpose was purely the study of truss behavior in the space environment [27]. One of the primary goals was to observe thermal snap in orbit, so it was outfitted with high-sensitivity accelerometers. It demonstrated that thermal snap (slipping against static friction in a joint due to thermal expansion) occurred in an ADAM mast when it moving into and out of sunlight. The IPEX-II mast has also been used as test hardware in a number of studies on mast dynamics [34] and micromechanics. Hardaway and Peterson [18] used the IPEX-II mast to demonstrate that a jointed bay, under shear loads much lower than those that would cause frictional slippage, would produce very subtle vibrations in its shear mode. This was attributed to "the sudden release of strain energy stored in the hysteretic mechanisms and/or the materials of the structure." [18, p. 2076]

An early version of ADAM, IPEX-II was not produced for a specific structural use and lacks certain features of later systems, such as a reliable latch backstop. It was used for some preliminary testing in this project, but the WSOA sample mast was preferred because it is a later model with a variety of performance advantages.

2.4.1.2 Shuttle Radar Topography Mission

The Shuttle Radar Topography Mission (SRTM) was flown by the Space Shuttle Endeavour as a part of STS-99 in February of 2000. SRTM used an ADAM boom to create a long 60-m separation between two parts of its interferometric synthetic aperture radar system [17]. This radar system was used to generate an elevation map of the majority of the earth's surface in greater detail than had been previously available.

SRTM demonstrated the necessity of on-orbit monitoring of structures. With a 60-m-long boom (Figure 2.11), its normal modes could cause significant dynamics, and estimates produced before launch were expected to be accurate to only 20% [52]. Further, a damping subsystem failure damaged the dynamic behavior of the mast, requiring the use of redundant systems to maintain control of the boom. Umland [49] presented an investigation of the damping subsystem failure, which is believed to have arisen from the expansion of a component of the damping system between testing and use. The leading explanation was that a combination of incorrect tolerances and stress relaxation lead to the closing an unintentionally small clearance in the damping canisters, locking them. A secondary theory was that the damping canister material may have expanded by absorbing silicone fluid. In

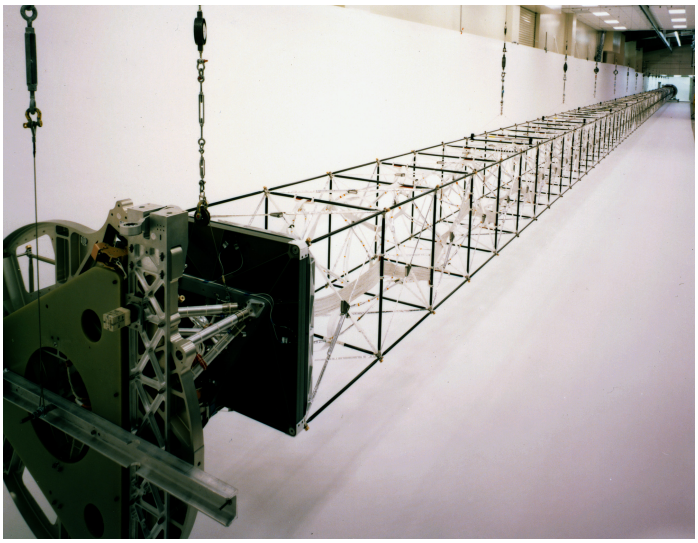

Figure 2.11: The SRTM mast (NASA image [33]). The mast is approximately 1 m wide and 60 m long when fully deployed.

either case, Umland describes a failure that resulted from minute changes in a tightly toleranced moving part during the time spent in storage.

Despite this difficulty, the SRTM experiment produced an altitude map of 80% of the earth's surface. Calibration of the radar data [52] required simultaneous tracking, through the metrology system, of the position and attitude of the outboard antenna. GPS and ground telemetry for the shuttle orbiter were also integrated for production of the final map.

At the time of this writing, the SRTM mast is on display in the Smithsonian Air and Space Museum[44]. It is, at 60 m, the longest rigid structure ever flown in space [33].

2.4.1.3 NuSTAR

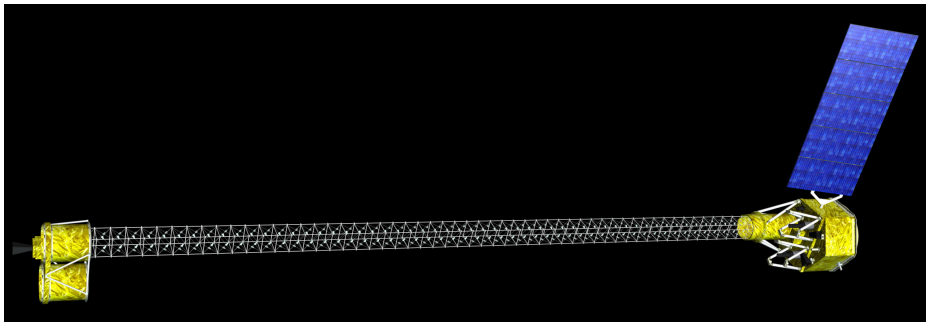

Figure 2.12: Artist's image of NuSTAR, with the optics at left and detectors/spacecraft bus at right (NASA image [5]).

NuSTAR (Figure 2.12) is an x-ray telescope, scheduled to launch in 2012, which will dramatically improve astronomers' ability to resolve objects in the hard x-ray spectrum. It will take observations in the range of 10-79 keV with 40 arcsecond resolution [5]. X-ray focusing optics, unlike visible light optics, rely on reflective elements oriented at grazing angles to the incoming rays [23], and the focal length of this telescope is consequently quite long in comparison to the diameter of its optics. The optics will be deployed and held 10 m away from the detectors by an ADAM boom. NuSTAR is the highest-precision use of this technology to date, and also arguably the highest-precision application currently possible. The focusing requirements of this system are not very stringent, requiring accuracy of millimeters in the axial separation between the optics and the detectors [28].

> Because the absolute deployment location of the mast is difficult to measure on the ground, due to complications associated with complete gravity offloading, an adjustment mechanism is built into the last section of the mast to enable a one-time alignment to optimize the location of the optical axes on the focal plane. This mechanism provides two angular adjustments as well as rotation. The mast is not perfectly rigid, but undergoes thermal distortions particularly when going in and out of Earth shadow (the mission is deployed in a low-Earth orbit) that translate into changes in telescope alignment of 1–2 [arcminutes].[19, p. 5]

Moving beyond the demands of NuSTAR will require even more predictable structures. Previously neglected mechanical effects need to be enumerated, characterized, and included in predictive modeling. The remainder of this thesis will observe and model some of these under-characterized effects.

Chapter 3

Experimental properties of mast components

This section presents experimental measurements of the longeron ball-end joint friction, the in situ cable preload, the cable stiffness, and the latch behavior.

Characterization of the latches occupies a substantial portion of this chapter because they are the most complex single part on the mast, and because their behavior is very difficult to model from first principles. Because the latches are typically under tension during use, and because of the relatively large displacements they can undergo, the support rigging for latch measurements required special attention.

3.1 Longeron ball-end friction

Friction in the ball-end joints of the mast resists rotation of the longerons in their sockets. A very low friction can lead to behavior that resembles a mast with pin joints, while very high friction approaches the behavior of an unjointed structure. The load required to guarantee sticking or slipping is dependent on joint friction coefficients, so this parameter works in concert with the cable preload to determine whether there will be joint slippage and the range of positions the joint can maintain against the restoring forces at work in the mast.

This experiment attempted to isolate the friction in individual longeron ball-end joints. A separate calibration of the joint friction to measurements of an assembled mast was also performed, and the calibrated value was substantially lower than the range of experimentally observed values. Possible inadequacies in this experimental approach are discussed at the end of this section.

3.1.1 Experiment

The ball-end joint friction was measured using an MTS material testing machine, model 358.xx, with axial-torsional load cell model 110.19. This is a pneumatic machine and can simultaneously control torsion and axial load, with a load cell capacity of 3300 lbf (15 kN) in axial force and 1500 in-lbf (170 N-m) in torsion. One longeron and its two batten corner fittings were tested at once (therefore, it is expected that the results describe slippage of whichever end had less friction). The batten corner fittings cannot be detached from the batten squares, so remained connected during the tests, as can been seen in Figure 3.1. The head was adjusted to provide between 75 and 400 N of compressive force on the vertical longeron.

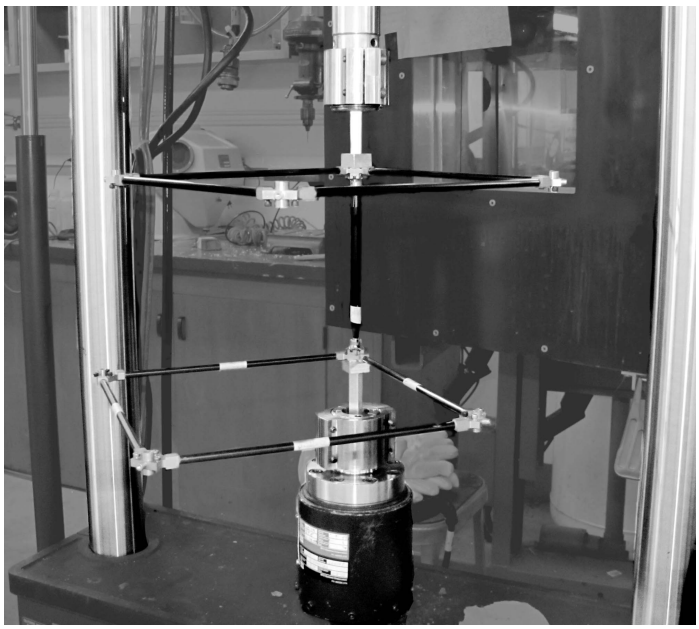

Figure 3.1: Experimental setup for longeron ball end friction test.

With the longeron under compression, the vertical position of the moving head was fixed and the head was rotated through 0.5° and back to its starting position. No rate dependence was observed, and all data presented here was gathered under a rotation rate of 0.25°/m. A typical time series is shown in Figure 3.3. At a fixed head height, the compression measurement wandered over a range of approximately 50 N, indicating that there might be a slight dependence between the angle of the longeron in its fitting and the functional length of this member. An alternate explanation is that the load cell or the machine control system may not have this level of sensitivity, especially over this very large rotation range. An acknowledged weakness of this method is that it measures the resistance to twisting about the axis of the longeron, which is not the primary component of the

rotation in actual use.

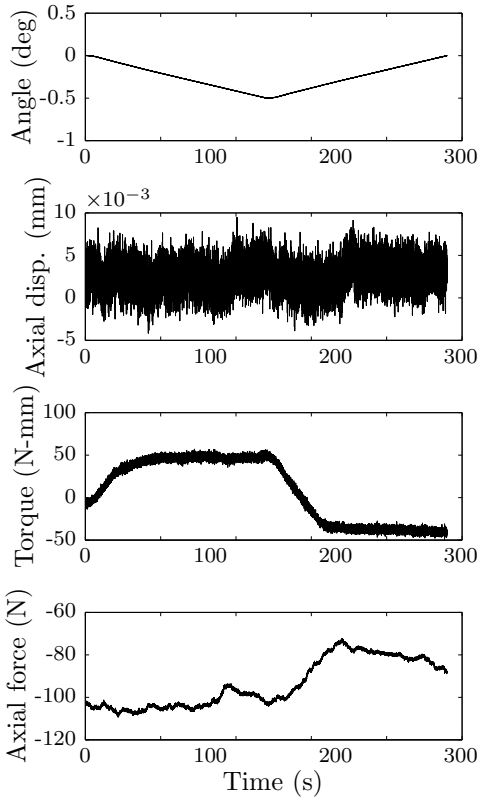

Figure 3.2: Time series of displacements and loads for torsion testing of friction.

Four longerons were tested. These were the longerons from the four corners of the top bay of the WSOA mast. The top two bays were used in all the full-bay experiments.

3.1.2 Results

Figures 3.4 and 3.5 show the results of the torsion testing of longerons under compressive load. The effect of friction can be reduced to the ratio τ/F_{axial}, which ranged from $\tau/F_{\text{axial}} = 0.2$ to 0.6 mm, for torque τ and axial load F_{axial}.

The ball-end radius was 4 mm, but due to the cone angle of the socket, the circle of contact between the ball and the cone has a radius of 2.3 mm. This indicates an angle between the cone and the axis of the longeron of 55°.

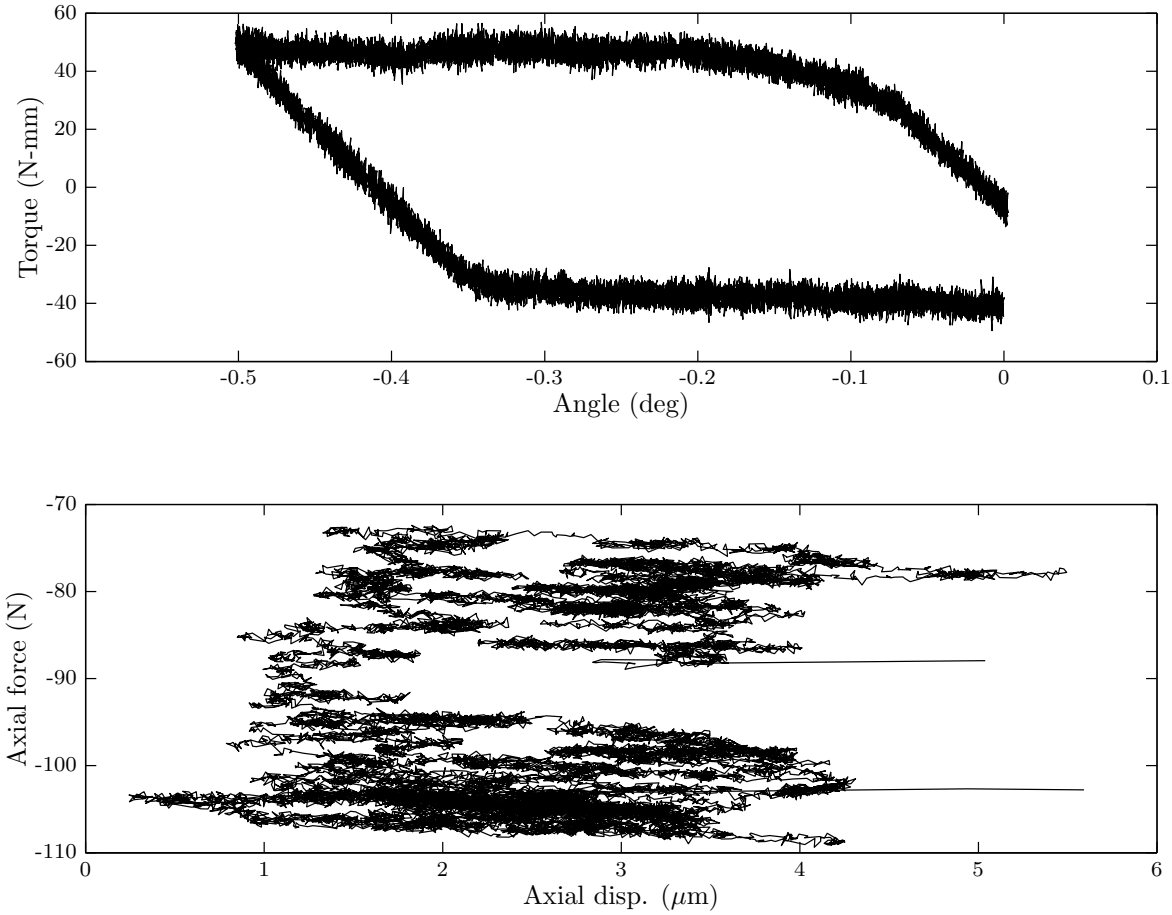

Figure 3.3: Force vs. displacment and torque vs. angle curves.

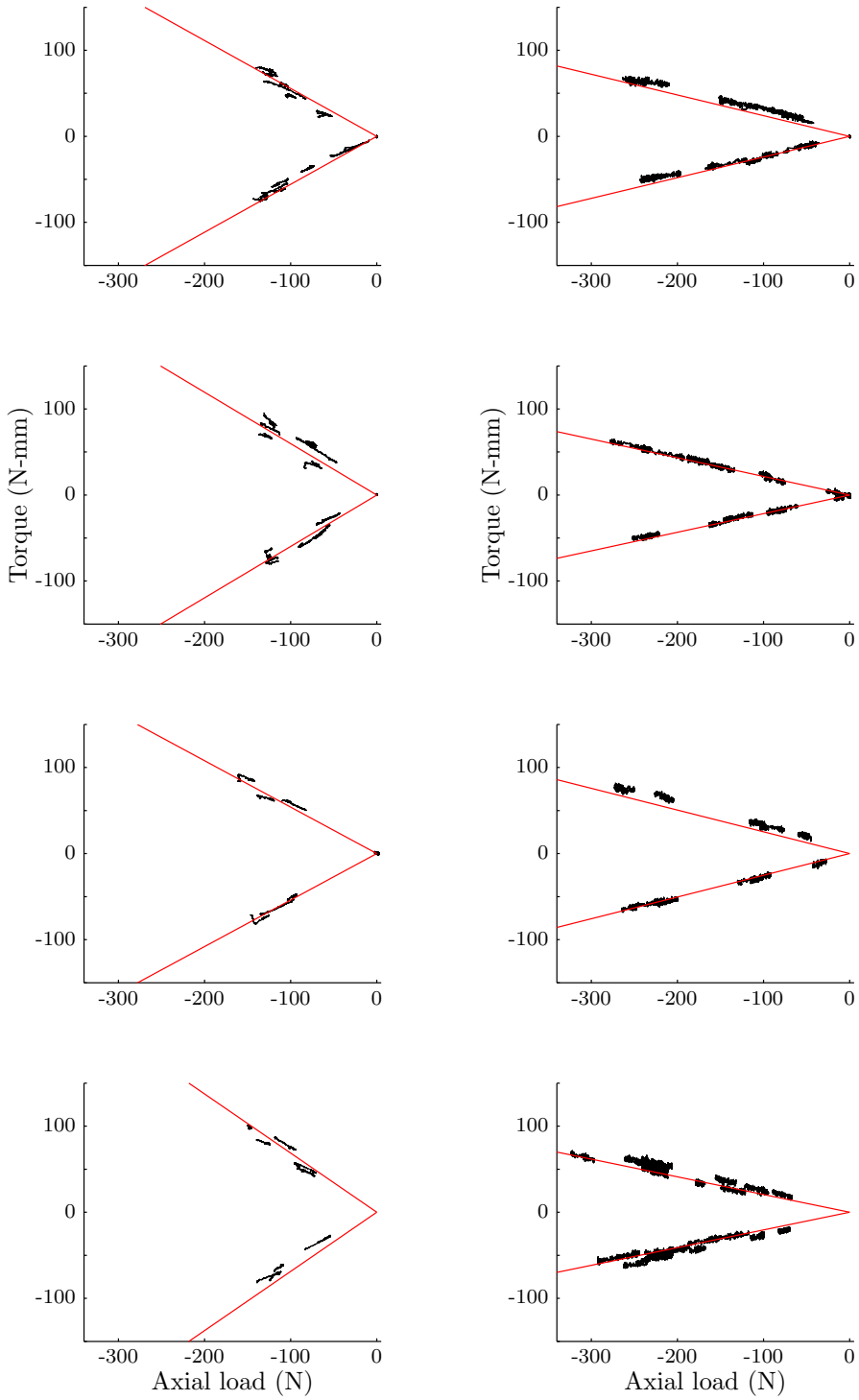

(a) Corner BC

(b) Corner DA

Figure 3.4: Results of friction testing. Each corner was tested four times, and the longeron rotated to a new position for each of the four tests. The straight lines (——) are fit values of Coulomb friction. Experimental data for the twelve tested longerons is shown in black.

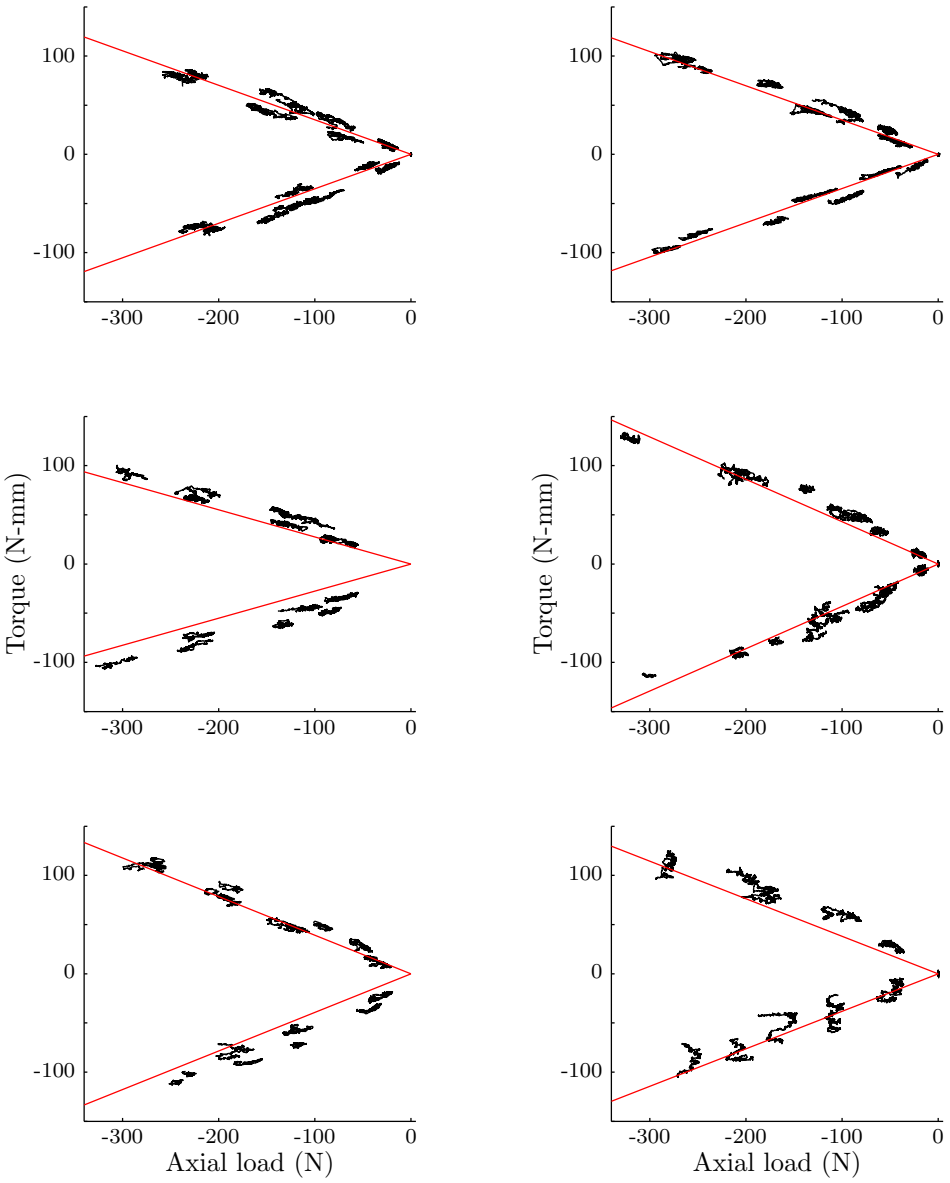

(a) Corner CD

(b) Corner AB

Figure 3.5: Results of friction testing. Each corner was tested three times, and the longeron rotated to a new position for each of the three tests. The straight lines (——) are fit values of Coulomb friction. Experimental data for the twelve tested longerons is shown in black.

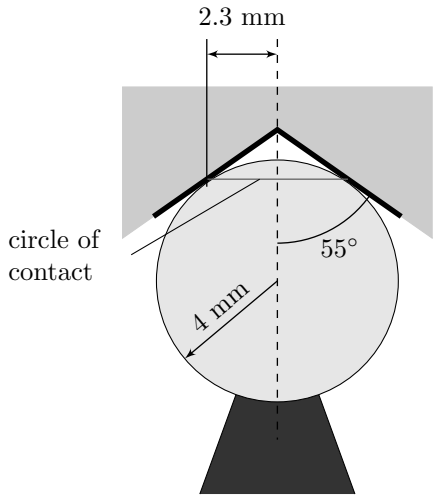

Figure 3.6: Geometry of the longeron ball-end joint

Assuming uniform friction around the contact circle, it is possible to approximate the metal-on-metal kinetic friction as follows.

$$F_f = \mu_{\text{metal}} F_n \tag{3.1}$$

$$F_n = \frac{F_{\text{axial}}}{\sin(55^\circ)} \tag{3.2}$$

$$(2.3 \text{ mm}) F_f = \tau \tag{3.3}$$

$$\mu_{\text{metal}} \approx \frac{\tau}{F_{\text{axial}}} \frac{\sin 55^\circ}{2.3} \tag{3.4}$$

This corresponds to a range from $\mu = 0.08$ to 0.21 for the metal-on-metal friction in the joint. This result is of the order of magnitude of friction coefficients for unlubricated metal-on-metal friction.[1] Several things are noteworthy about these results. As mentioned, the compression varied throughout each experiment; while this was not intended, it revealed that the data does show some resemblance to the idealized frictional behavior, in the sense that there are at least locally linear relationships, passing through $(0, 0)$, between the compression and the torque.

There is a notably large spread in the data, and even within the data on any given longeron. This is somewhat related to the length of the test, or the number of cycles of torsional motion the longeron undergoes in a given data set. For example, Figure 3.7 shows the fifteen cycles used to characterize corner DA at one angular position. All tests produced the same effect: the joints appear

[1] For example, $\mu \approx 0.5$ for brass on mild steel [51, p. 139], although no information about the specific materials used in the sample mast is available.

to increase in friction as they are worked back and forth over a number of cycles.

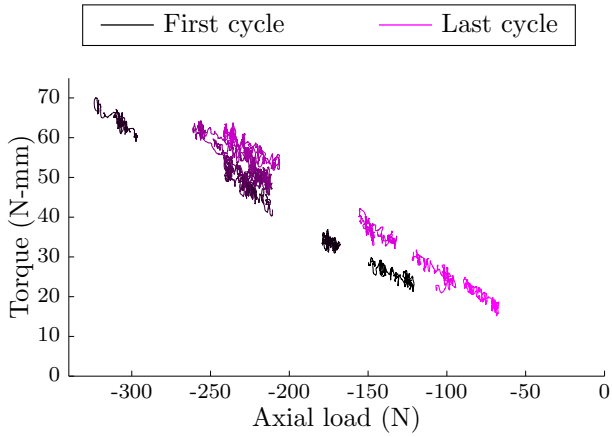

Figure 3.7: Close view of the fourth data set for corner DA.The friction value appear to increase with each cycle of torsional motion.

Table 3.1: Summary of friction values.

Corner (number of longeron rotations)	mean $\tau/F_{\text{axial}}\pm$ st. dev.	mean $\mu\pm$ st. dev.
AB (3)	0.39 ± 0.04 mm	0.12 ± 0.02
BC (4)	0.60 ± 0.07 mm	0.21 ± 0.02
CD (3)	0.36 ± 0.06 mm	0.14 ± 0.01
DA (4)	0.23 ± 0.02 mm	0.081 ± 0.008
Four corners	0.39 ± 0.15 mm	0.14 ± 0.05

The ball-in-cone shape of the joint creates a dilemma in modeling the friction, even under the assumption that the ball joint reliably rests loaded against the cone. The distance from the axis of rotation of the ball to the circle of contact with the cone is dependent on the axis of rotation. As described in Section 5.1.3, this effect is ultimately disregarded in the computational model, as further calibration of the friction values was done.

Both the magnitude of the friction and the apparent quality of the data varied between corners and between tests on the same corner. The surfaces were not cleaned before measurements, and had been used to many years prior, and therefore the uncontrolled environment and the possibility that the joints were damaged or dirty are believed to be the primary causes of the scatter in the frictional measurements. This measurement range is also very close to the limit of the sensitivity of the torsional load cell, which is a plausible additional contribution to noise and unrepeatability in the data. The impact of the longeron joint friction is discussed from a parametric perspective in Section 6.1.2, which finds that the overall mast behavior better matches a substantially lower

friction value of $\mu \approx 0.03$. The implementation of the idealized but varied friction values is discussed in Section 5.3.1.

Measurements of the longeron joint friction could be improved with a more involved approach to these measurements. More repeatable alignment of the parts in a testing rig may be possible, and more controlled surface cleanliness and ambient conditions would be ideal. It would be useful to measure the friction reaction for different directions of joint rotation. The possibility of angle-dependent friction exists as well, due to the surface flaws in these joints and sockets. It would also be possible to measure the response of a bay skeleton, without cables, in simultaneous axial and torsional loading, which would exercise the most common direction of motion for the longeron joints. The study of the ball-end joint behavior could be greatly expanded, but the approach pursued here did not produce successful a priori knowledge of the longeron ball-end joint friction for the mast model.

3.2 Cable preload

The diagonal cables on the face of each bay carry tension in the fully deployed and locked configuration. Under normal operating conditions, the cables should always be tensioned and never slack. A number of manufacturing conditions affect the range of cable preloads, including the elastic modulus of the cable, the length of the cable, and the sizing of all the surrounding parts, which in tandem determine the final position of the face corners.

The level of preload in the cables is an important input to the model, affecting the state of the latches and friction in the longeron end joints. Although the cable preload in this structure was evaluated primarily for its relationship with friction, preloads in the general case can be noteworthy for their effects on structural stiffness, as discussed by Pellegrino [36], and the subject is of general importance in predicting structural performance. The primary goal of these experiments was to identify the mean and standard deviation of the cable tensions in a deployed mast. This was later transformed into a statistical distribution of initial cable lengths for the finite element model.

3.2.1 Empirical relationship between tension and vibration frequency

Because of the relatively short length of the cables and the initially unknown tension range, commercially available three-point tension meters were unsuitable. Therefore, a vibration method was chosen to measure the cable tension in the fully deployed structure. This method depends on the

existence of a simple relationship between the tension in the cables and the restoring force against out-of-plane motion on a face.

Assuming that the latch assembly is suspended in the plane of the bay face by four cables of equal length L and tensions T_1 through T_4, it will experience a restoring force F_r at the center of the latch assembly for a small out-of-plane displacement δ of

$$F_r = \sum_{i=1}^{4} T_i \frac{\delta}{L}; \tag{3.5}$$

which, further assuming massless cables and a latch mass m, can be connected to the resonant frequency for small vibrations, ω, through Equation 3.6

$$\omega^2 = \frac{F_r}{m\delta} = \frac{\sum_{i=1}^{4} T_i}{Lm} \tag{3.6}$$

Equation 3.6 is the guiding relationship for the identification of cable preload. No attempt will be made to identify true values of L or m, only the overall coefficients that define the relationship between $f = \omega/2\pi$ and $T_{\text{mean}} = \sum_{i=1}^{4} T_i/4$. Simultaneous measurements of f and T_{mean} produced the coefficients of a quadratic polynomial that is used in Section 3.2.2 as the calibration curve for in situ cable preload measurements.

3.2.1.1 Calibration experiment

The measurement procedure consisted of applying a vibrating force to the latch at the center of a bay face and identifying the bay side's resonant frequency in out-of-plane motion. There is a monotonic relationship between cable tension and resonant frequency, which had to be quantitatively identified before in situ cable tensions could be measured. Because of the difficulties inherent in measuring the tension of a stranded cable in situ, a mock bay side (shown in Figure 3.8) with space for inline force sensors (Futek model LCM300, with a capacity of ±250 lbf [1110 N]) was built.

The mock bay side holds the cable assembly in the same geometry as the actual bay side. The end position of each cable is adjustable so that the cables could be tensioned to different levels. In general, it is difficult to unbalance the tensions in the cables, and only the average tension of the four cables will be considered here.

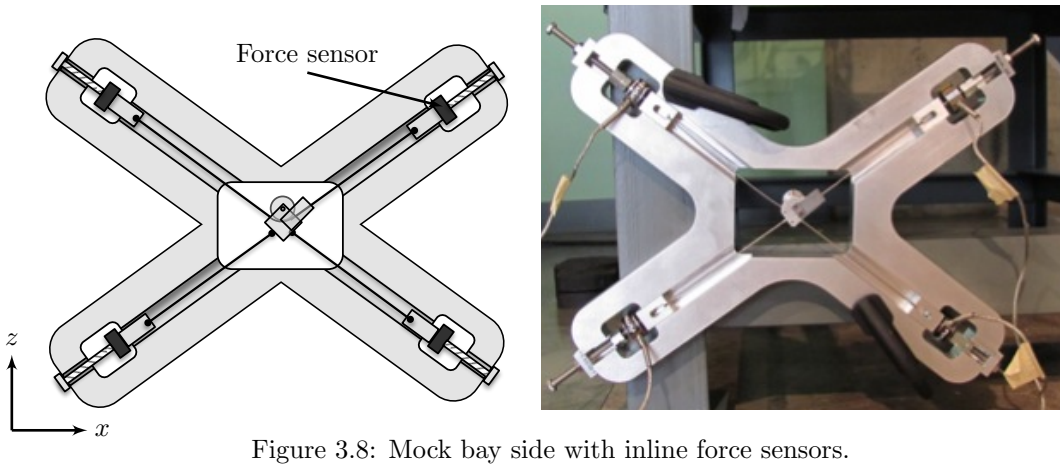

Figure 3.8: Mock bay side with inline force sensors.

The latch at the center of the cable assembly was excited by a Labworks, Inc., model ET-132 shaker performing a sine wave sweep from 50 to 100 Hz over 5 minutes. This range was selected after a number of preliminary sweeps established the typical peak locations. A force sensor at the end of the shaker sting measured the applied force, while a Keyence model G157 laser rangefinder tracked the out-of-plane motion of the latch. The positions of the shaker, force sensor, and laser can be seen in Figure 3.9. Data was recorded at 1000 Hz. Dividing the fast Fourier transform (FFT) of the displacement by the FFT of the applied force, a clear peak can be identified. A set of typical peaks obtained for different cable preloads is shown in Figure 3.10.

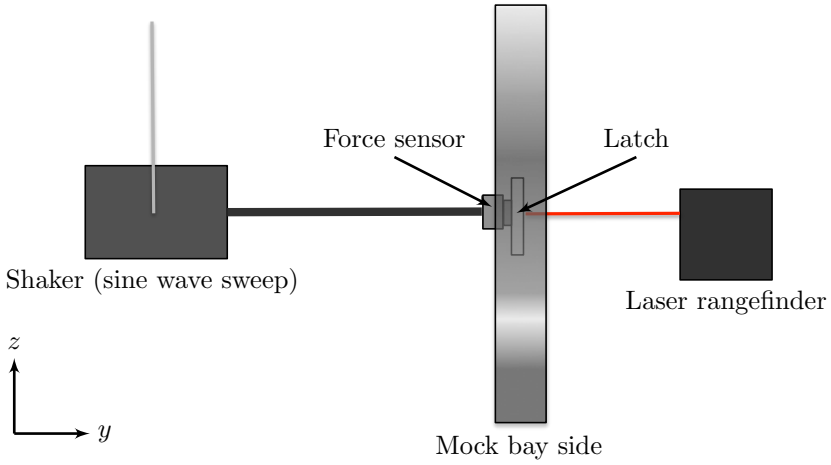

Figure 3.9: Mock bay (side view) with vibration testing equipment.

Rather than using the location of the maximum, the resonant frequency was identified through a weighted average. This improved the agreement between multiple measurements of the same bay face, where peaks were sometimes split or less well-defined. The weighting formula was

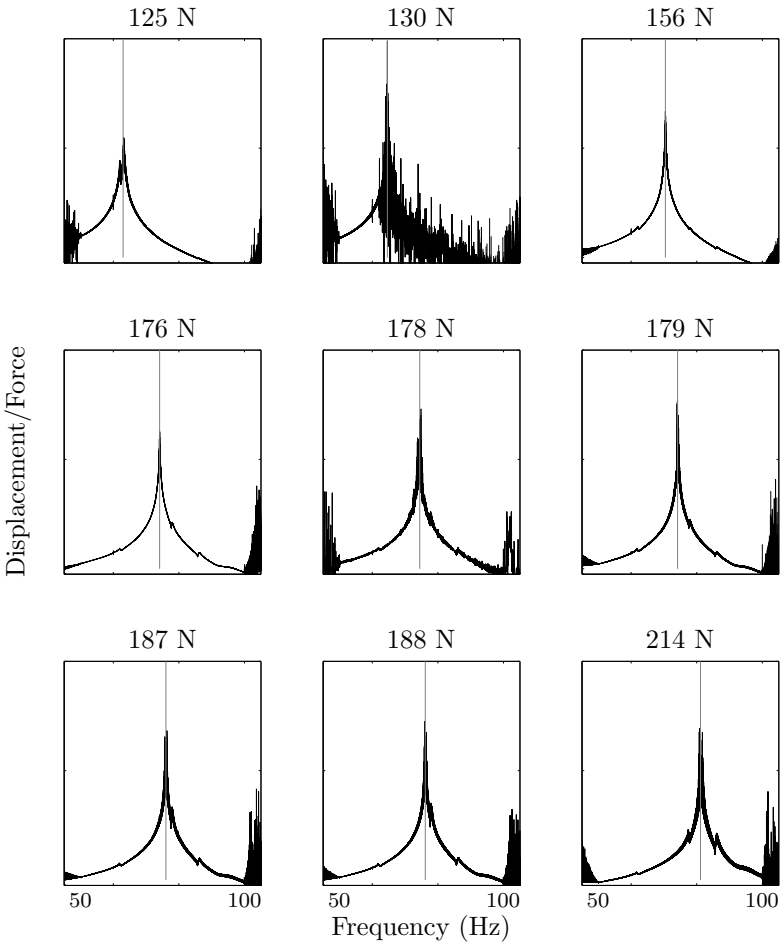

Figure 3.10: Resonance peaks of nine experimental data points. The vertical axis uses a log scale. Peak values used for the fit are highlighted with vertical lines.

$$\mathbf{y} = \frac{|\mathcal{F}(\mathbf{x})|}{|\mathcal{F}(\mathbf{F})|} \tag{3.7}$$

$$f_{\text{peak}} = \frac{\sum_i y_i^2 f_i}{\sum_i y_i^2} \tag{3.8}$$

where $\mathcal{F}$ denotes the FFT, $\mathbf{x}$ is the displacement output by the laser displacement sensor, $\mathbf{F}$ is the force as reported by the dynamic force sensor, y_i is the ratio of displacement to force at frequency f_i, and f_{peak} is the calculated peak location. The values found with this weighting procedure differed from the locations of the maximum values by an average of 0.16 Hz, and at most by 0.4 Hz (in the 178 N dataset of Figure 3.10). The advantage of this weighted peak is more apparent in the in situ data, where split peaks appeared.

3.2.1.2 Results

The peak locations were used to identify a quadratic polynomial that relates the cable tension T_{mean} to the resonant frequency of a side f_{peak}. The polynomial, by least-squares fitting, is

$$T_{\text{mean}} = 0.0362 f_{\text{peak}}^2 - 0.2396 f_{\text{peak}} - 4.5611 \tag{3.9}$$

for T in N and f in Hz. The root mean squared deviation, calculated as $\sqrt{\sum (T_{\text{meas.}} - T_{\text{calc.}})^2/(9-3)}$ for the nine data points and three fit parameters of Figure 3.10, was 1.5 N.

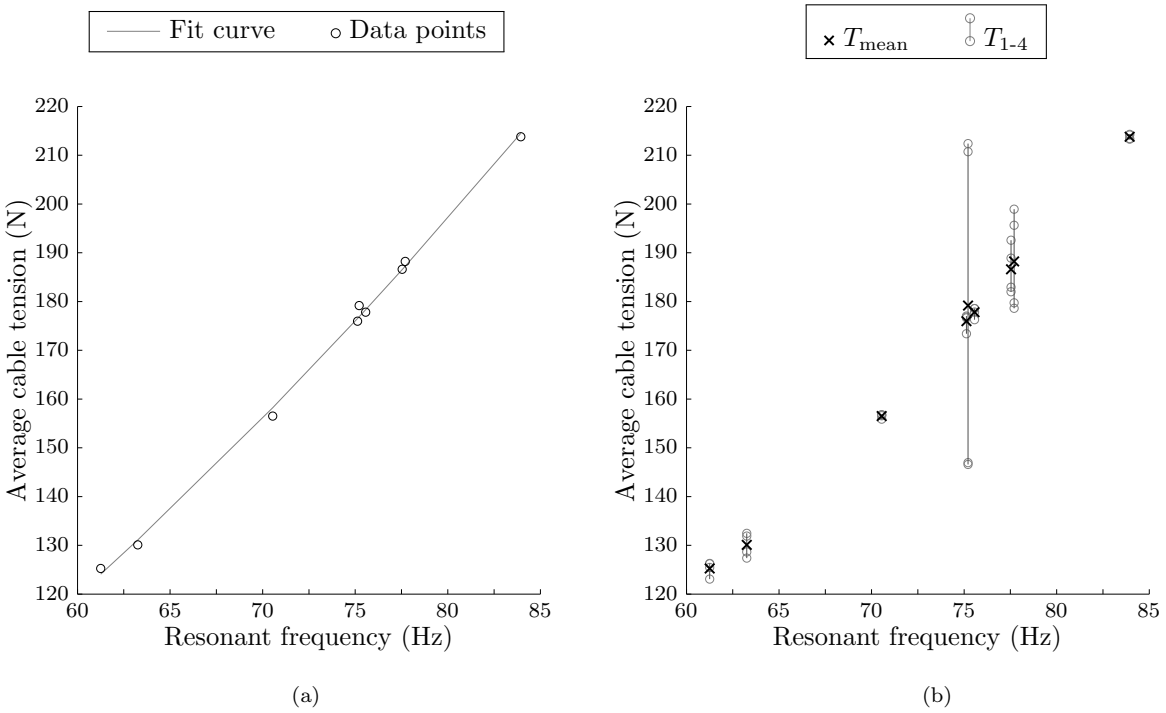

Figure 3.11: Data for empirical fit for the vibration method. Plot (a) shows the data points and the empirical fit of Equation 3.9; (b) shows the same averaged tensions with the four constituent tensions.

This method characterizes the *average* tension in the four cables that meet at the latch. By deliberately adjusting the rig such that $T_1 \neq T_2$, we can affirm that this is the measured quantity. Figure 3.11b shows the spread of cable tensions around each averaged point. A spread in cable tensions does not have any clear effect on the resonant frequency of the cable assembly.

3.2.2 In situ measurements of cable preload

Armed with the empirical relationship between resonant frequency and cable tension, the cable tensions of an actual mast can be collected. This is the data that should be reflected in the finite element model of the mast, and is ultimately encoded as a mean and variance in the unstretched lengths of the cables.

3.2.2.1 Experiment

A four-bay subsection of the WSOA mast was bolted by the pre-existing threaded holes in its base joints to a 1/2-in-thick aluminum plate, which was in turn bolted to a granite table, as shown in Figure 3.12. The four bays were numbered 1-4 from bottom to top, and the faces lettered counterclockwise as A, B, C, and D. Different bays' faces were excited and observed by adjusting the height of the shaker and laser, and different faces of the same bay were accessed by unbolting the aluminum baseplate rotating it 90°, and reattaching it.

The shaker was suspended by a cotton rope approximately 64 cm below a horizontal bar supported by an adjustable-height stand. To measure bay 4, the rope was shortened so that the pendulum arm length was approximately 44 cm, because the stand could not be adjusted to the height of this bay. The force sensor was connected to the approximate center of the latch with wax, and the shaker was able to push and pull on the latch through this connection.

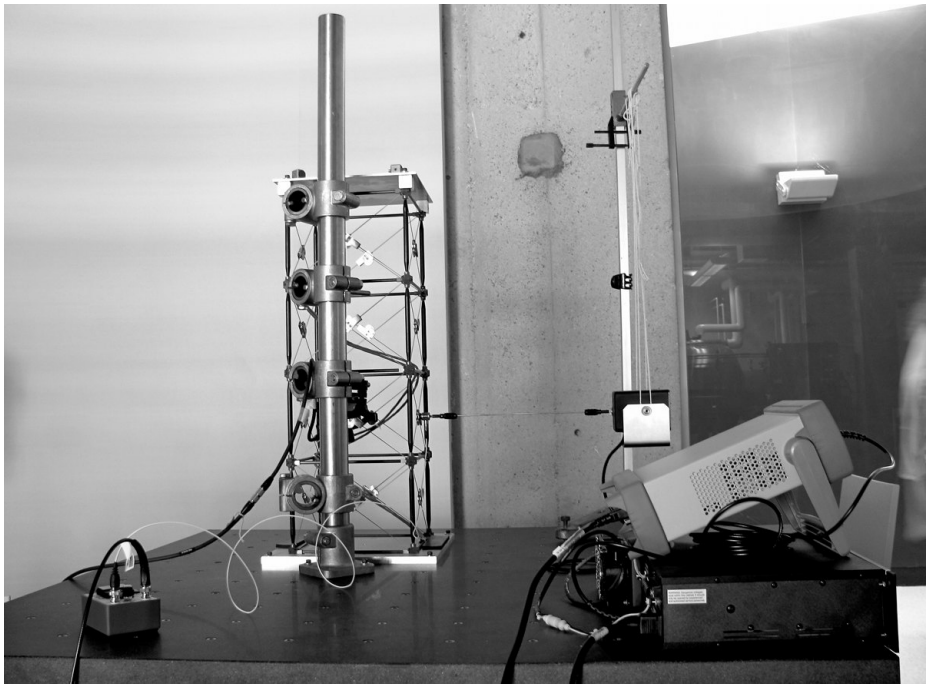

Figure 3.12: The four-bay mast and vibration measurement setup.

The shaker was run though a logarithmically distributed sine sweep from 50 to 100 Hz over periods ranging from 300 to 500 s for each data point.

As a brief investigation of the effect of load history on cable tension, a simple load was applied between two vibration tests of a single side of the bottom bay. The mast was loaded with a shear of approximately 90 N at its tip, in the $\pm x$ and $\pm y$ directions. The tension in the cables on the measured face did not measurably change after any of these transient loads. This supports the assertion that we have measured a fundamental property of this particular mast, rather than a highly variable or transient property.

3.2.2.2 Results

Resonant frequencies of sixteen total bay sides range from 60 to 100 Hz, corresponding to average diagonal tensions of 132-331 N. A set of typical results is shown in Figure 3.13.

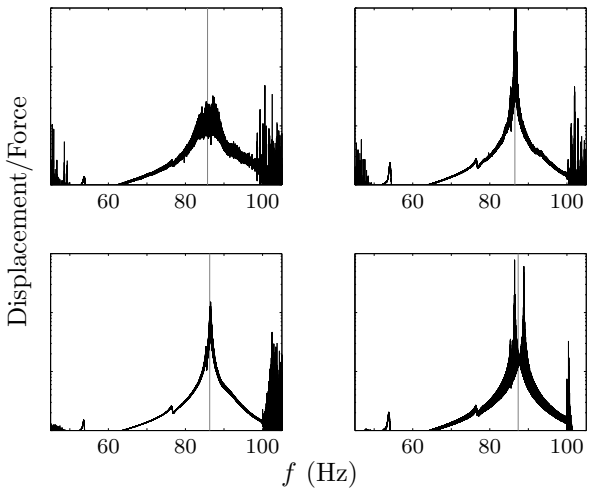

Figure 3.13: Four representative sweeps of Bay 2, Side A. The weighted peak is located at the vertical grey line. When all twelve samples are included, the standard deviation of weighted peak locations is 7.3 N, while the standard deviation of the simple maximum peak locations is 11.7 N.

Sample distribution The data presented in Table 3.2 was taken with incidental handling of the mast and readjustment of the experimental setup over the course of two days.

Table 3.2: Summary of face resonant frequency data from the four sides of four bays of WSOA. n denotes the number of trials; when n is given as (a) b, there were a trials of which b produced usable data.

	Side A		Side B		Side C		Side D	
	n	T (N)	n	T (N)	n	T (N)	n	T (N)
Bay 1	15	233.4 ± 5.3	(3) 2	238.5 ± 3.1	25	274.7 ± 7.2	2	221.4 ± 0.1
Bay 2	12	244.1 ± 7.3	2	235.2 ± 2.0	8	318.6 ± 4.4	2	177.1 ± 0.004
Bay 3	2	220.7 ± 2.6	2	205.3 ± 0.9	8	234.5 ± 3.0	2	205.5 ± 0.7
Bay 4	1	186.4	2	187.2 ± 0.3	5	132.7 ± 4.2	2	170.0 ± 0.2

While these frequencies are only reproducible to a standard deviation of a couple of Hertz, they differ from one another from fives or even tens of Hertz (standard deviation of the 16 mean fs was 8.4 Hz), and therefore some variability in cable pretension between faces and bays is established. The average standard deviation of measurements within a single side was 6 N, while the standard deviation of the sixteen mean measurements was 47 N, as illustrated in Figure 3.14.

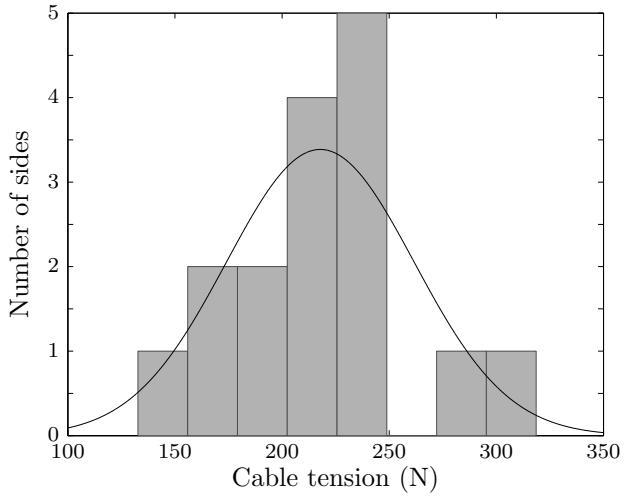

Figure 3.14: Histogram of sixteen face preloads. The overlaid curve is the normal distribution with the same mean and standard deviation.

These results are included in the model as described in Section 5.3.1, and it will be shown in Section 6.2.2 how the cable preload variability impacts on the modeling results. The experimental results are notable in their own right because of the great range of values that were found. The preload range is an indirect measurement of the range of lengths in the manufactured parts. A 100 μm variation in cable length is approximately equivalent to the observed 50 N variation in cable preload, and is certainly a plausible degree of error in the manufacturing of these cables (see Figure 3.22 for a closer view of a cable).

3.3 Latch and cable behavior

The most complex subsystem of the mast is the latching mechanism located at the center of each cable assembly. This is one of the least stiff parts of the mast, and demonstrates behavior that is nonlinear, hysteretic, and nonrepeatable on the micron level. The latch experiments were designed to isolate the latch so that the data would be useful in parametric studies, and at the same time maintained a geometry and external load levels similar to a latch in use.

Ultimately, the most important outcome of the latch studies is the constitutive relationship between the position of the bead (which is fixed on cable A-B) and the force applied to the bead. This force is assumed to be equivalent to $\Delta T = T_B - T_A$. In Section 5.2.2, a method for integrating this data into a finite element model is presented.

3.3.1 Stiffness of cables

The stiffness of the cables was measured using an Instron (model 5569) material testing machine. Using fittings that bolted together to hold the cable terminating beads, the ends of cables A and C of one bay face were connected to the testing machine and stretched and released at a rate of 0.6×10^{-5} strain/s, or 0.1 mm/minute. The results of this test are shown in Figure 3.15.

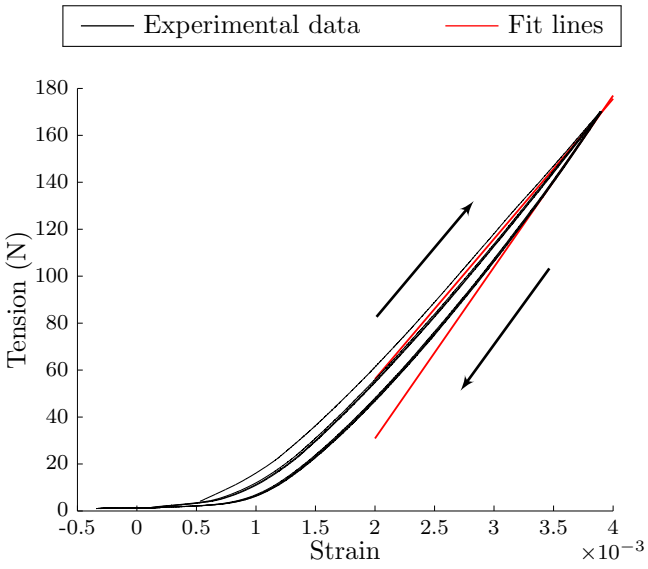

Figure 3.15: The measured force-strain relationship for the cables. The first cycle of stretching and releasing the cable shows a slightly lower stiffness, while all subsequent cycles are indistinguishable. Lines of slope 60 and 73 kN are underlaid, and fit the loading and unloading curves, respectively.

Because the cables operate under tension the vast majority of the time, the single value of 73 kN

was used for a linearly elastic approximation of this behavior in the model.

3.3.2 Latch behavior experiment

Ideally, the behavior of the cable assembly should be broken down into the behavior of the cables (as simple 1-D elements) and the behavior of the latch. The isolation of these two behaviors makes it possible to adjust them independently during modeling, and evaluate their individual impacts. The goal of these experiments was to identify a constitutive relationship for the latch of the form $\Delta T = \Delta T(x, T_A, T_B)$, where ΔT is the difference in tension between cables A and B (i.e., $\Delta T = T_B - T_A$, with T_A, T_B the tensions in cables A and B), and x is the distance from the center of the bead (which is fixed to cable A-B) to the center of the rollers in the latch, as depicted in Figure 3.19.

A rig, shown schematically in Figure 3.16 and in the photograph of Figure 3.17, was used to maintain a level of tension similar to that of a deployed bay in all cables. A weight of approximately 170 N was hung over a pulley to tension cable A. The termination of cable D was fixed to the base of the testing machine, and the termination of cable B to the load cell, which is collocated with the moving head of the testing machine. The termination of cable C was supported by the same piece of rigging as the pulley and weight.

The rig was aligned manually such that opposing cable pairs A-C and B-D formed straight lines. The angles were adjusted to within 5° of the angles of an actual bay side.

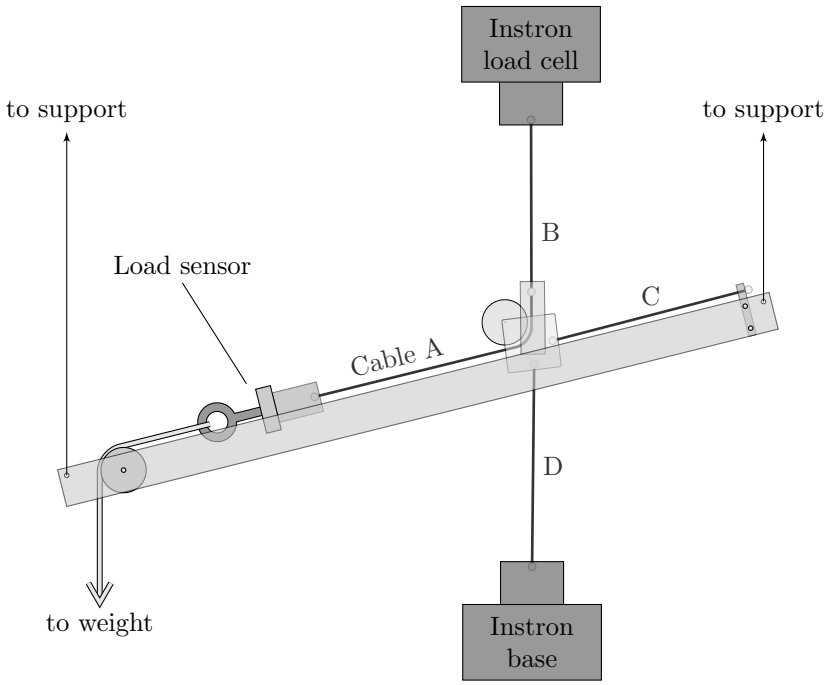

Figure 3.16: The latching mechanism setup. Two support methods were used without impact on the results: suspension from above and a combination of a hinged support at the weight end with a simple vertical support at the other end.

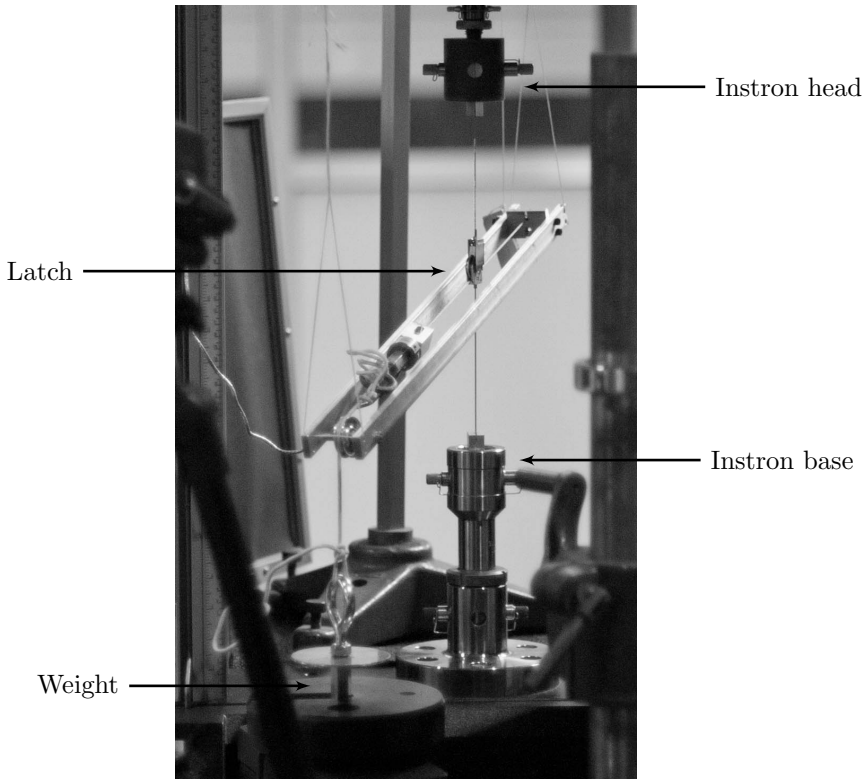

Figure 3.17: Photograph of the latch rig in the material testing machine.

The displacement between the bead and the rollers was measured with a laser extensometer (Electronic Instrument Research model LE-05). This extensometer measures the vertical distance between two horizontal retroreflective strips. One strip was located near the center of the latch, and one was located on a small metal tab that had been glued to the cable, butting against the top of the bead. Neither the glue nor the metal plate were in contact with any part of the latch at any time, as the back end of the bead remains outside the jaws of the latch at all times. A photograph of the retroreflective strips is shown in Figure 3.18.

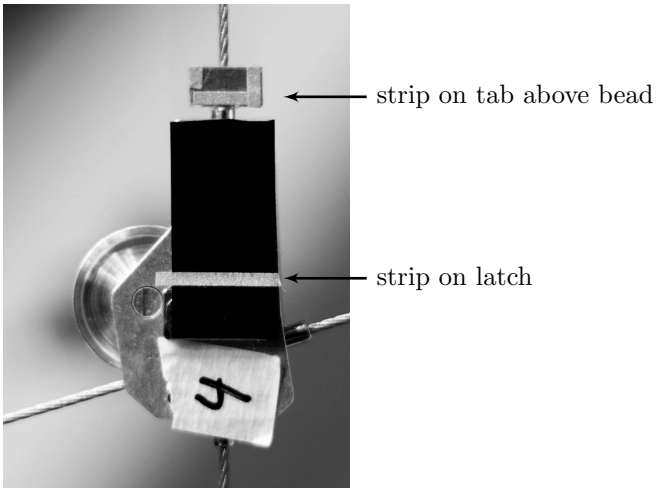

Figure 3.18: Placement of retroreflective strips on the latching mechanism. The top strip is applied to a metal tab, which is fixed to the cable and the back of the bead; the bottom strip is fixed to the body of the latch and away from the jaws, which would deform slightly during bead capture. The bottom strip was applied over black electrical tape to reduce stray reflections.

The load cell head was cycled up and down to move the bead in and out of the latch. At rates ranging from 0.1 to 4 mm/min, no rate dependence was observed. Twelve latches were tested, with each being removed from and remounted in the rig for multiple sets of measurements.

3.3.3 Analytical model of latch

As described in [45] and Section 5.2.2.1, an idealized theoretical behavior for the latch can be derived from a set of simple assumptions about the shapes and behaviors of its parts. Assuming that the bead moves along the centerline between two cylindrical rollers, subject to a linearly elastic pinching force from the roller jaws and Coulomb friction opposing the motion of the rollers, the relationship between the tension differential ΔT and the bead position x, illustrated in Figure 3.19, is:

$$\delta = \sqrt{(r+R)^2 - x^2} - h - r \tag{3.10}$$

$$\Delta T = \begin{cases} -2k\delta\left(\frac{x+\mu(h+\delta+r)}{h+\delta+r-\mu x}\right) & dx < 0 \\ -2k\delta\left(\frac{x-\mu(h+\delta+r)}{h+\delta+r+\mu x}\right) & dx > 0 \end{cases} \tag{3.11}$$

where k is the stiffness of the jaws, h is the initial separation between the rollers, r is the radius of each roller, R is the radius of the bead, and μ is the coefficient of friction governing the roller behavior. The geometric variables can be seen in Figure 3.19. r, R, k, μ and the zero points of x and ΔT were fit to the experimental data using least-squares criteria. $R + r$ and $h + r$ were treated as single variables, as R, r, and h are not independent variables in these equations. $R + r$ is the distance from the center of the bead to the center of each roller when the bead is just touching the roller, and $r + h$ is the distance from the centerline of the latch to the center of each roller when the jaws are relaxed. A typical fit is shown in Figure 3.20.

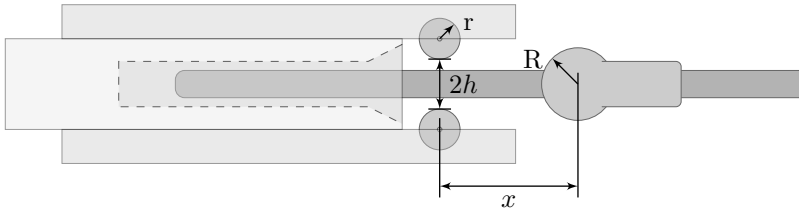

Figure 3.19: Latch variables (side view).

3.3.4 Results

As mentioned, the product of these measurements is a relationship between x and $\Delta T = T_B - T_A$. Examining the experimental results, it becomes clear that a fit curve is not sufficient to describe the detailed behavior of the latch. Deviations from the fit are especially prominent in the crucial area near the backstop.

3.3.4.1 Fit data

Since the distance from the roller center to the bead center, x, was not directly measured, the extensometer measurements were offset as part of the curve fitting.

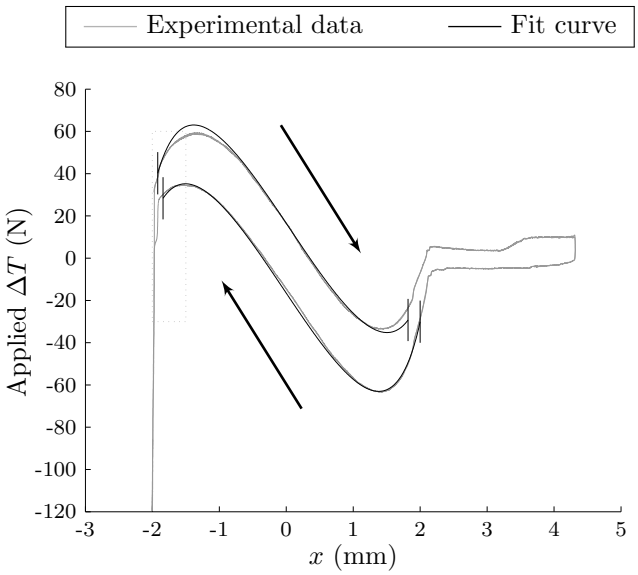

Figure 3.20: Experimental and fit data for two load displacement cycles of one latch. Only the data between pairs of vertical lines was used in the fit. A closeup of the near-vertical section around $x = -2$ mm is shown in Figure 3.21

The data shown in Table 3.3 was fit from several trials of each of eight latches. These fits show that, at best, these parameters of the latches have been distinguished from one another only marginally. For example, the fit values of k for latches 2A and 2D are 51.4 and 60.2 N/mm, with standard errors on the means of 3.4 and 1.9 N/mm, respectively. It is possible that these fit values would be definitively distinguishable with more experimental trials.

Table 3.3: Fit values for eight tested latches.

Bay side (# trials)	k (N/mm) ($\pm$ st. dev.)	μ	$R + r$ (mm)	$h + r$ (mm)
1A (2)	59.2 ± 2.8	0.1332 ± 0.0045	2.610 ± 0.046	1.557 ± 0.066
1B (1)	56.2	0.1310	2.615	1.540
1C (2)	54.2 ± 1.1	0.1319 ± 0.0032	2.556 ± 0.012	1.424 ± 0.025
1D (2)	50.2 ± 1.3	0.1352 ± 0.0091	2.523 ± 0.016	1.379 ± 0.018
2A (4)	51.4 ± 6.8	0.1541 ± 0.0044	2.487 ± 0.110	1.366 ± 0.190
2B (3)	57.7 ± 2.9	0.1143 ± 0.0035	2.599 ± 0.041	1.518 ± 0.067
2C (3)	51.2 ± 4.7	0.1374 ± 0.0130	2.508 ± 0.110	1.353 ± 0.170
2D (4)	60.2 ± 3.9	0.1255 ± 0.0059	2.736 ± 0.072	1.693 ± 0.098
3A (2)	50.2 ± 1.5	0.1230 ± 0.0052	2.546 ± 0.040	1.402 ± 0.053
3B (1)	50.0	0.1572	2.530	1.393
3C (1)	56.0	0.1428	2.655	1.620
3D (2)	53.2 ± 9.6	0.1338 ± 0.0150	2.541 ± 0.130	1.425 ± 0.230
All bay side means (12)	54.1 ± 3.7	0.1349 ± 0.0120	2.575 ± 0.071	2.575 ± 0.071
All samples (27)	54.4 ± 5.3	0.1340 ± 0.0140	2.576 ± 0.100	1.473 ± 0.160

3.3.4.2 Deviation from fit shape

The most important area of the bead's motion in the latch is the zone near the backstop, because after deployment this is the only range that is visited during normal operation of the mast. Perfect latch behavior would require an absolutely rigid backstop and perfectly repeatable seating of the bead, but experimental measurements deviate from this idealization. The most significant deviations are visible in Figure 3.21. The cause of the stepping behavior seen around $x = 1.9$ mm in this figure is not known, but it has a significant impact on the near-backstop behavior. Further, the exact backstop location measurement seems to lack repeatability on the level of tens of microns.

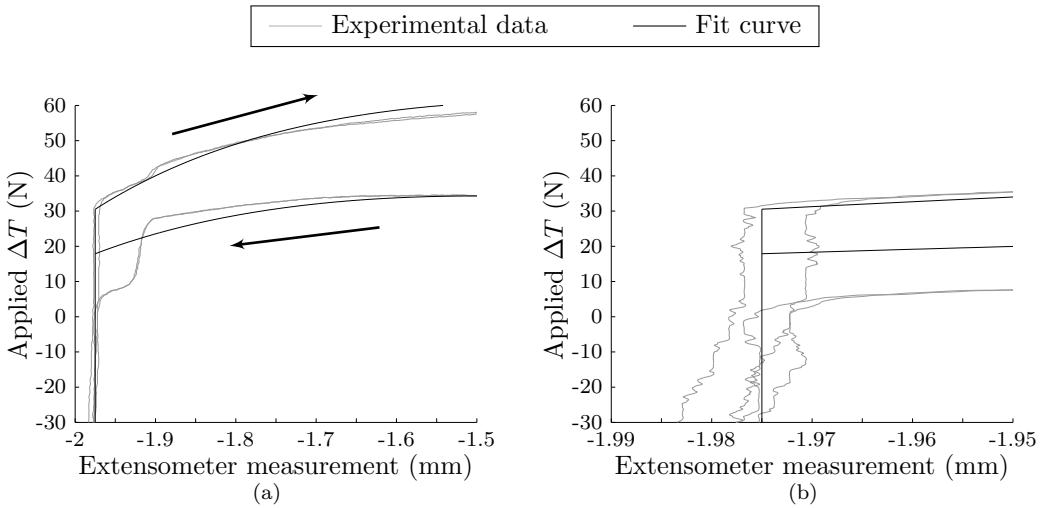

Figure 3.21: A closeup of the experimentally measured latch behavior (grey) in contrast with idealized near-backstop behavior overlaid (black). The figure on the right shows an extreme close up of backstop behavior. Two repetitions of the same loop of bead motion within the same trial are shown.

These deviations from an ideal profile may be caused by deviations from the idealized shape or from the idealized kinematics. When the bead is against the backstop, the latch jaws are resting on the curved bead back surface, so contact between nonspherical bead surfaces and the jaws is not a primary concern. However, the front surface of the bead and the precise shape of the backstop are both visibly nonideal, as shown in Figure 3.22. It is also possible that the bead and cable may not be perfectly centered in the latch, making small stick-slip events possible. Further, unexpected changes in the angle of the retroreflective strip that indicated vertical bead position could have caused movement in other directions to be misinterpreted as the expected vertical motion.

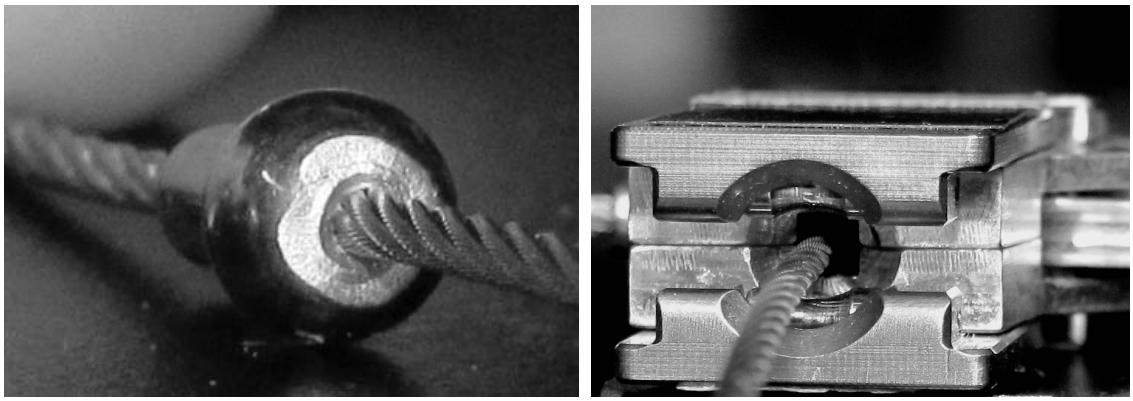

(a) (b)

Figure 3.22: Deviations from idealized shapes of the bead and backstop. A closeup of the front of a bead, which contacts the backstop, is shown in (a), and (b) shows a closeup of a backstop.

The integration of these results with the finite element model is discussed in Section 5.2.2.2. In order to incorporate the true near-backstop behavior, a selection of experimental data was processed into lookup tables, which are used to define the relationship between x and ΔT over a range of values of x before the peak of unlatching force. The lookup table data transitions into an analytical representation of the latch model, which is used for the latch behavior far from the backstop. The more complicated lookup table is shown to have a significant effect on the results in Section 6.2.4.

Chapter 4

Experimental properties of mast bays

The following experiments were designed to validate the computational model. One- or two-bay mast segments were subjected to various loading conditions while their tip displacements were tracked, producing force-displacement curves for the segments. While a more conventional structural identification would be matching the stiffness of the bays, this study is more concerned with frictional effects. In the validation experiments and the matching simulations, capturing the shapes of the hysteresis loops is one key goal; another is to achieve some level of accuracy in the residual displacements at zero load, or the range of resting positions. This range of possible residual displacements is important because it is an upper bound on the severity of a static error in the mast due to friction.

First, a torsion test wherein one bay was stowed and redeployed was performed. This torsional movement exercised a small rotation of the longeron joints and the full range of motion of the latches. Results from this test will be used in Section 7.1 to confirm the validity of the latch models.

The second set of experimental observations of bay behavior were shear load tests. Shear testing tracked residual displacements and coupling between modes of deformation under more modest load than the torsion test, at a level that did not induce bay collapse or latch release. Shear loads are carried by the cables and latches more than, for example, axial loading, and therefore emphasize the behavior of the specific components of the mast that are considered most important to this study.

In all full-bay experiments, the position of the top batten square was tracked using six rangefinding lasers (Keyence models G87 and G157). These lasers measure the change in distance (within a certain range) to a surface. This data was transformed into three components of translation and three components of rotation by the method described in Appendix A.

4.1 Stowage and deployment

The bay was stowed and deployed by twisting the top batten frame relative to the base. By measuring the applied torsion throughout this motion, a moment-angle relationship for the complete bay in torsion was identified. This record of the moment required to deploy a bay resembles the torque that could be provided by a deployment motor. It is not a perfect representation of the bay's reaction to a deployment motor in actual use, because the bays would be deployed from a canister that constrains the off-axis motion of the bay.

4.1.1 Experiment

Using six rangefinding lasers, the position and orientation of the top batten square was tracked at 200 Hz. The arrangement of these lasers is shown in Figure 4.1. Assuming that the top batten frame and attached plate are effectively rigid, all six components of the batten's motion can be assessed from this data.

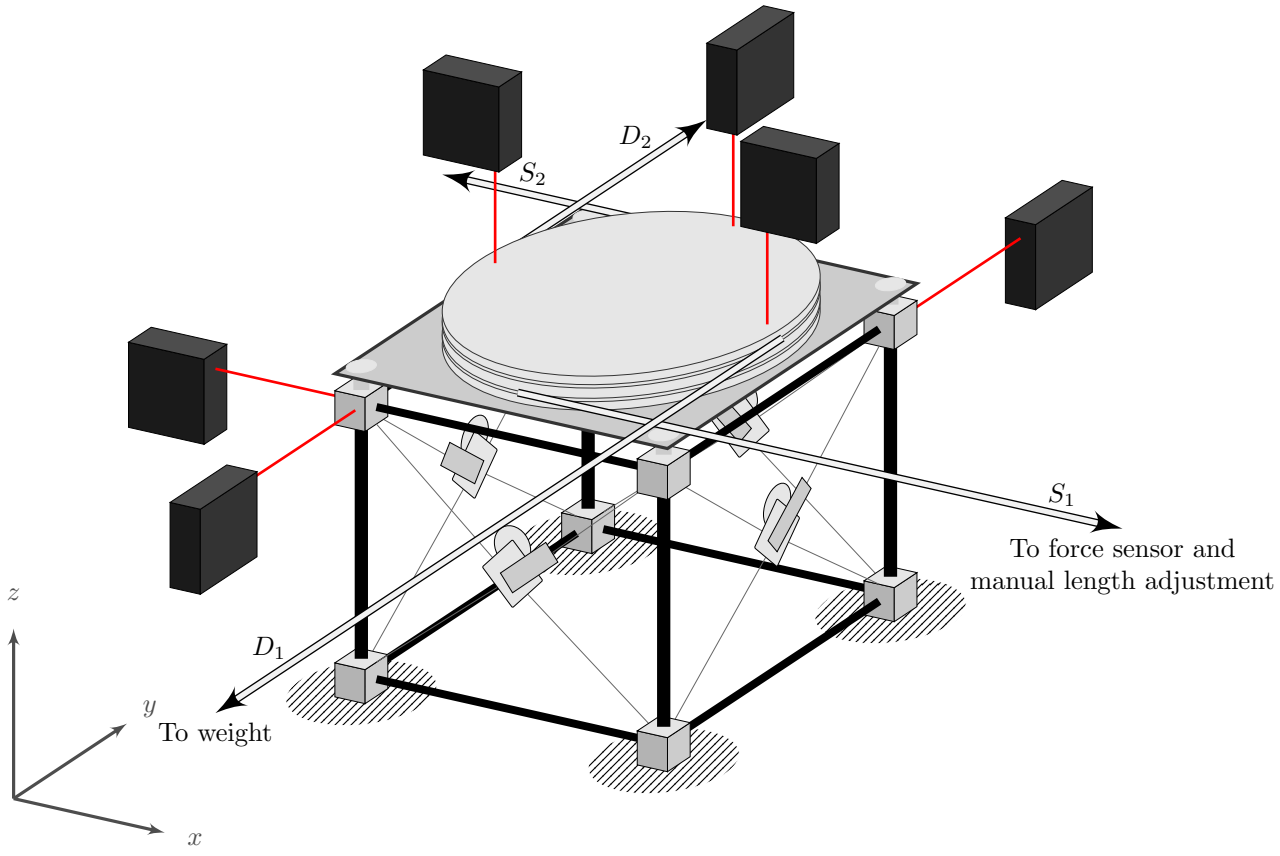

Figure 4.1: Experimental setup for torsion test, showing laser arrangement.

The torquing forces were applied through two sets of cables. The cables were wound around and each individually attached to a wheel, which was, in turn, bolted to the top batten square. The deployment cables, D_1 and D_2, were loaded by weights at the end of each cable and provided a constant torque in a clockwise sense, i.e., towards the deployed configuration. The stowage cables, S_1 and S_2, were each connected to a manual length-adjustment mechanism. This set of cables loaded the top batten square in a counterclockwise sense, toward the stowed configuration, and included inline force sensors so that the net torque could be calculated from the two force measurements and the two constant loads.

This setup made it possible to apply a moment continuously, without a dead band at zero moment. It should be noted that the loading arrangement did not provide any constraint keeping the bay aligned or symmetric. As discussed in the following sections, this complicates the modeling problem.

Each experiment was carried out starting in the fully deployed state with the full load of the weights applying a moment of 35 N-m about the $-z$ axis. The cables in line with the force sensors were then shortened, in steps of a fraction of a millimeter, over a period of approximately 15 minutes. These cables were adjusted by drawing an eyebolt at the end of each cable into a nut. The bolts were turned one at a time, alternating quarter-turns between cables S_1 and S_2. At about 3° of rotation, three of the four latches had unlatched and the bay no longer provided any resistance to further motion. At this point in the experiment, the motion was reversed by gradually lengthening the adjustable cables. This allowed the weighted cables to apply a deployment torque and return the bay to its original deployed configuration.

4.1.2 Results

The hand-turned adjustment of the cable lengths produced an irregular pattern in the loading. The stepping behavior seen in the time series of Figure 4.2 is caused by the pauses between turns of the bolts that controlled the lengths of cables S_1 and S_2. All six degrees of freedom of the top batten square are involved, although the motion is primarily twist about the z-axis.

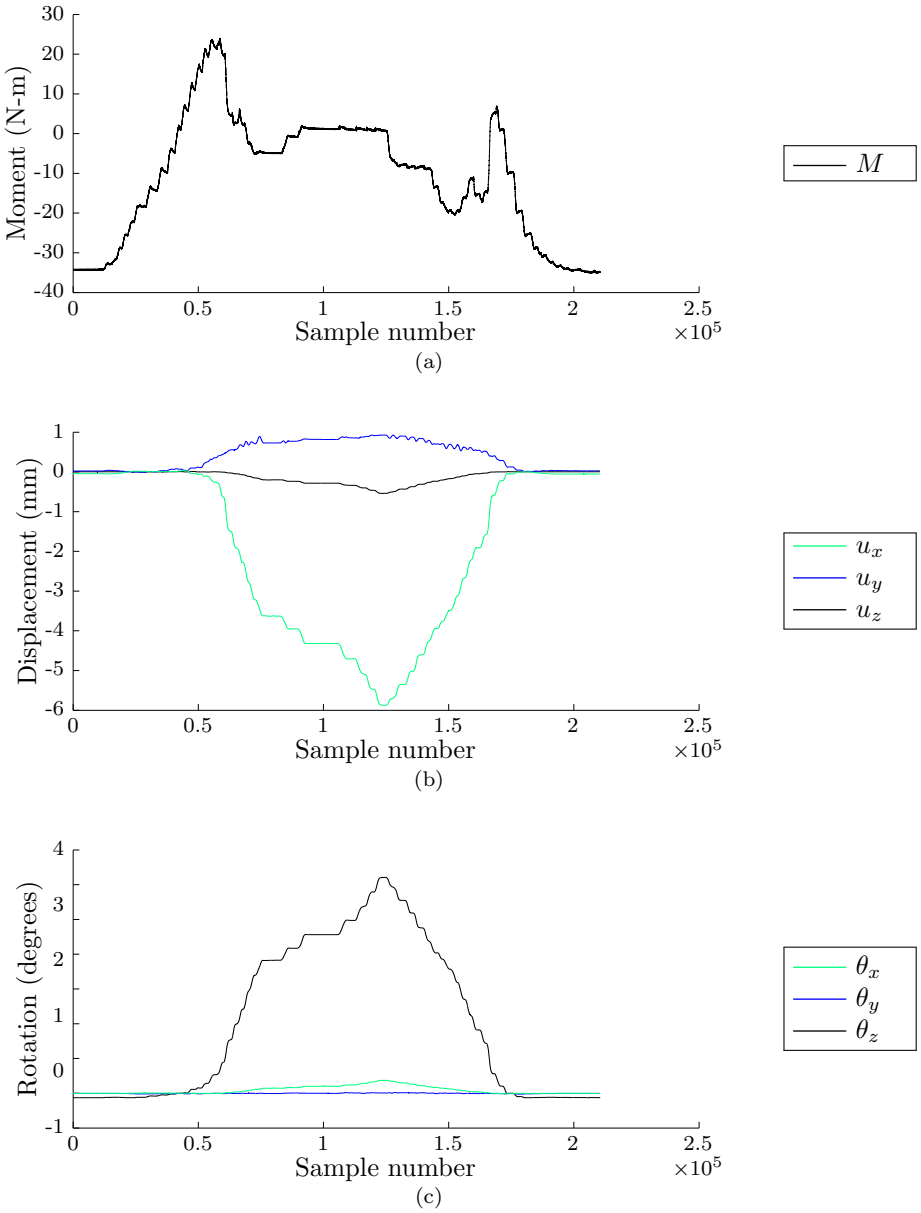

Figure 4.2: Six degrees of freedom defining the motion of the top batten square.

The moment-angle relationship through a cycle of stowage and deployment is quite nonlinear and hysteretic, as seen in Figure 4.3. Asymmetries in loading and in the behavior of the components of the bay may be a partial reason. When there is no constraint forcing a perfectly symmetric collapse, the sides will unlatch one at a time. Symmetry-breaking sequential unlatching was observed in these experiments.

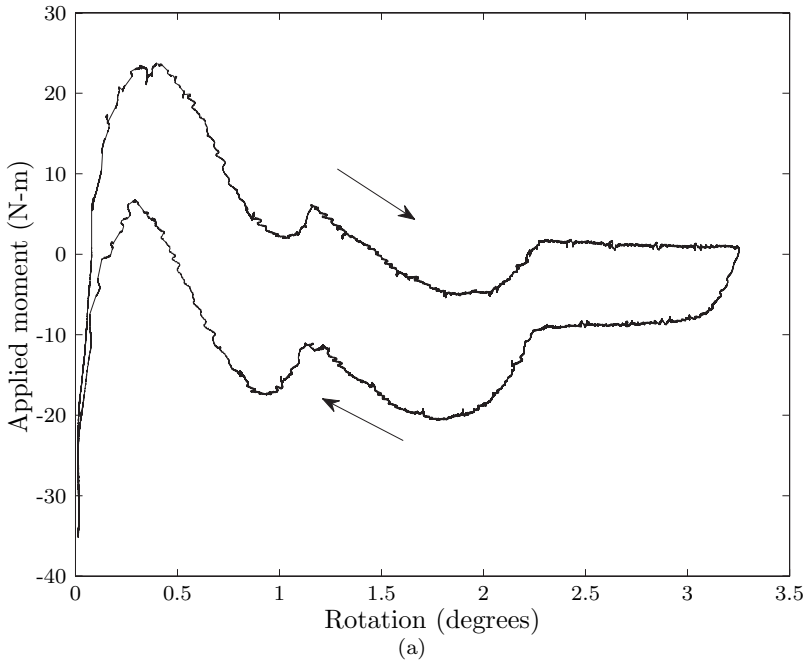

(a)

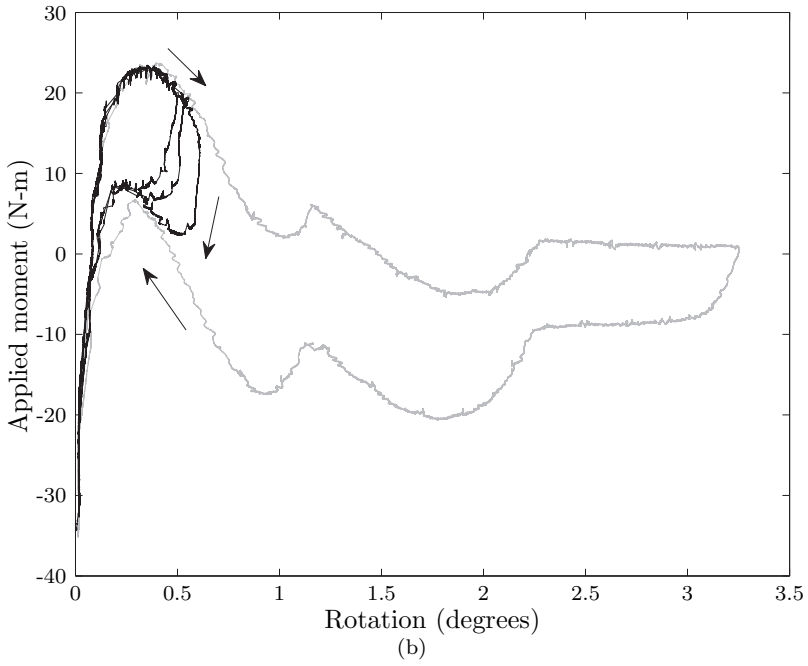

(b)

Figure 4.3: Moment-angle relationship in a single bay. A full stowage and deployment cycle is shown in (a), while in (b) a set of three smaller loops, without any delatching, is superimposed on the same full cycle.

Figure 4.3a requires some explanation. First, the gap between the stowage and deployment paths is attributed to friction in the latches and joints. It can be seen in Figure 4.3b that, if the rotation

is reversed earlier in the cycle, it rejoins the same deployment path. Secondly, there are three major regions: from 0 to 1°, the latches dominate the response. This is the stiffest region because it requires the locking force provided by the latches to be overcome. From 1 to 2.5°, the stretching of the cables dominates the behavior. Beyond this, the mast is nearly free to move.

Figure 4.4 illustrates some of the substantial off-axis motion that the mast undergoes during this experiment. This figure traces the path of the node at the center of the top batten square through its displacements u_x and u_y in the x-y plane. Through cross-referencing with the time histories of Figure 4.2 and the moment-angle plot in Figure 4.3a, we can see that the wavy patterns in the path to the left of $u_x \approx -2$ occur after the peak of moment, i.e., after the bay has at least partially delatched. The looping pattern may be due to the very compliant partially deployed mast responding to the intermittent nature of the load.

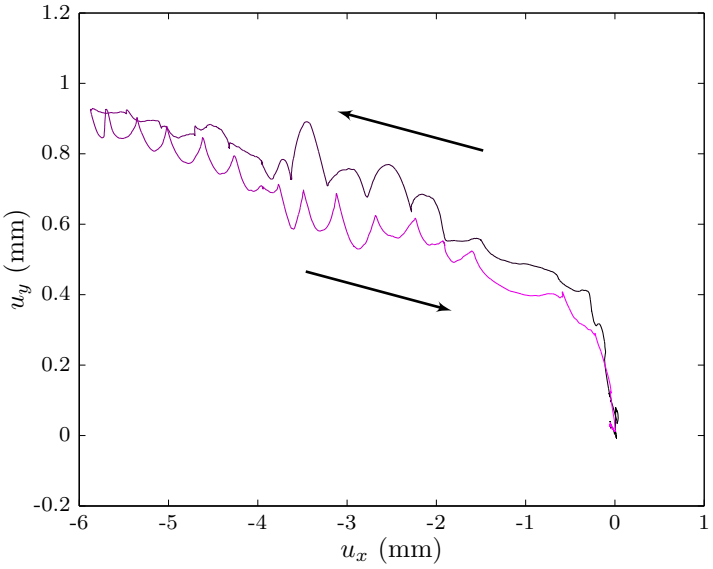

Figure 4.4: Path of the centerpoint of the top batten square in the x-y plane.

4.2 Shear loading

Transient loading cases are a central focus of this modeling problem. One of the goals of this study is to address the question of what happens to the resting shape of a mast when it is loaded and unloaded. During a slewing maneuver in space, a mast would see transient loads and be expected to return to an acceptable position after the maneuver. If the mast can maintain a shape that puts it outside the acceptable range, it would then be required to limit the rate of attitude adjustment

in use.

In order to explore the limiting load cases, a two-bay mast was loaded to very near the limit of collapsing and allowed to relax back to a neutral position. Small residual displacements were measured during this loading sequence.

4.2.1 Experiment

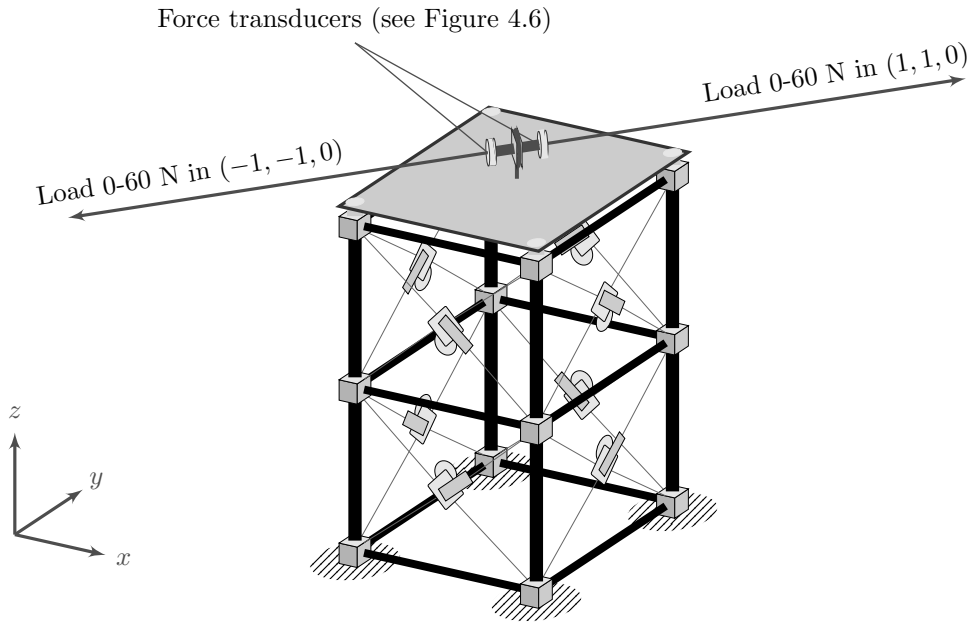

Figure 4.5: Schematic of shear loading experiment. The loading cables lie in a plane 57.5 mm above the center of the top batten square.

A two-bay mast was bolted at its four bottom corners to a granite table and loaded in shear, as shown in Figure 4.5. The loads (of approximately 60 N magnitude) were applied in the x-y plane through an eyebolt fixed at the center of an aluminum plate, which was bolted to the joints of the top batten square. Two colinear cables were attached to force sensors at the eyebolt, and each cable was strung over a pulley so that loads could be applied using lead shot. Displacements were measured at the top of the two-bay mast, using rangefinding lasers in the same method described in Section 4.1.1.

The loading weight was provided by lead shot. A bucket with a removable cap in its base hung at the end of one loading cable, and then lead shot was poured into this bucket through a funnel. At the maximum load, the shot was drained from the loading bucket by unscrewing the cap. A typical loading pattern, as recorded by the inline force transducers (Figure 4.6), is shown in Figure 4.7.

Three experiments were carried out by this method, with the bay rotated by 90° between ex-

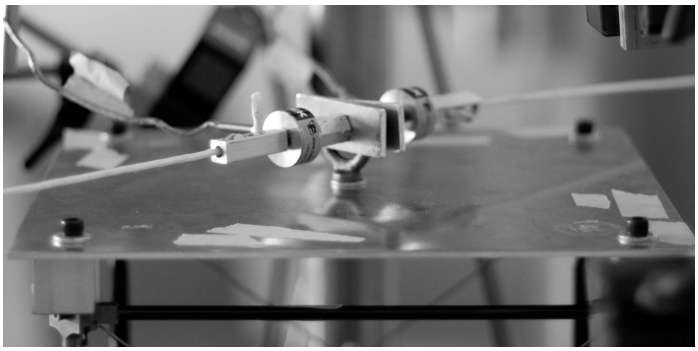

Figure 4.6: Detail of force sensors.

periments. The results for 0° and 180° should therefore correspond to identical loading cases in the frame of the mast, but they appear to differ, as will be discussed.

4.2.2 Results

Figures 4.8 and 4.9 show the relationship between load and displacement, and the path that the center of the top batten square was observed to take in the x-y plane. The 0° and 180° cases are not obviously more similar than the 0° and 90° cases. This may point to some irregularity in the measurement or loading systems that was not accounted for, or it may be due to a genuine unpredictability in the structure. These possibilities are explored computationally in Sections 6.2.5 and 7.2, with the ultimate result that the waviness of the x-y path was not reproducible through modeling. It is therefore concluded that this effect is not an accurate reflection of the mast behavior, but caused by either systematic error in the measurement of the displacements or in the establishment of the boundary conditions of the experiment.

An illustrative example of the dangers of incorrect assumptions about the measurement system was generated in earlier shear loading tests, where the load was applied to the corners of the top batten square, without the stiffening top plate. The deformation of the top batten square was of the same order of magnitude as the x and $y$displacements of the top center, leading to an intriguing but ultimately incorrect load-displacement profile (Figure 4.10). By assuming that the top batten square had only six degrees of freedom, the measurement and processing method lead to a puzzling set of data.

From this accidental result, we have a demonstration that the batten squares cannot be depended to act as rigid at these loads. A secondary benefit is an indirect measurement of the stiffness of the battens in bending. The battens are permanently fixed to the bay corners and their stiffness, based on this data, is investigated as a parametric study in Section 6.1.1.

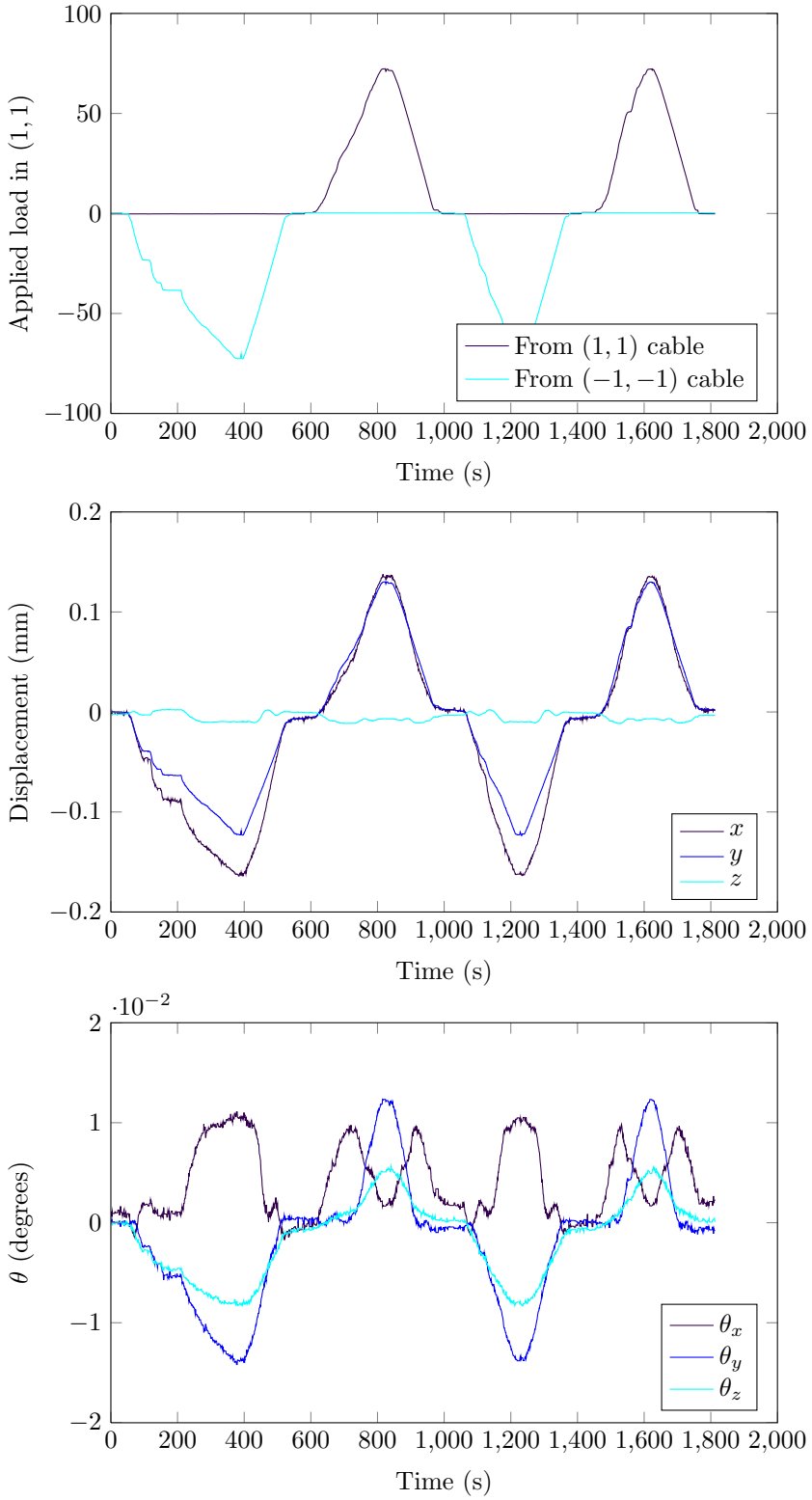

Figure 4.7: Loading and displacement patterns for the shear experiment at 0°.

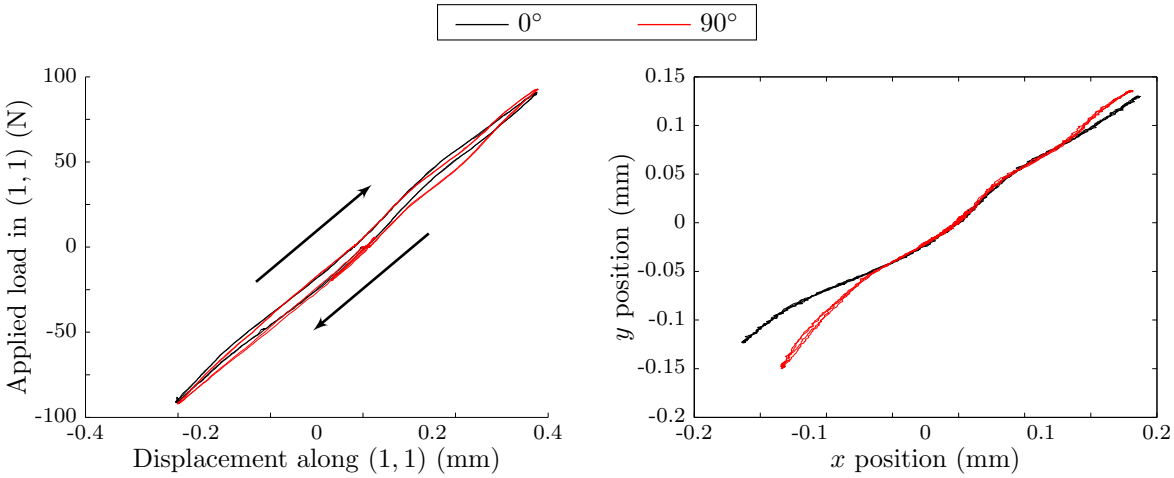

Figure 4.8: Load and displacement relationships for shear experiments at 0° and 90°. The orientation of the mast was shifted by 90° about its z axis between these two sets of data.

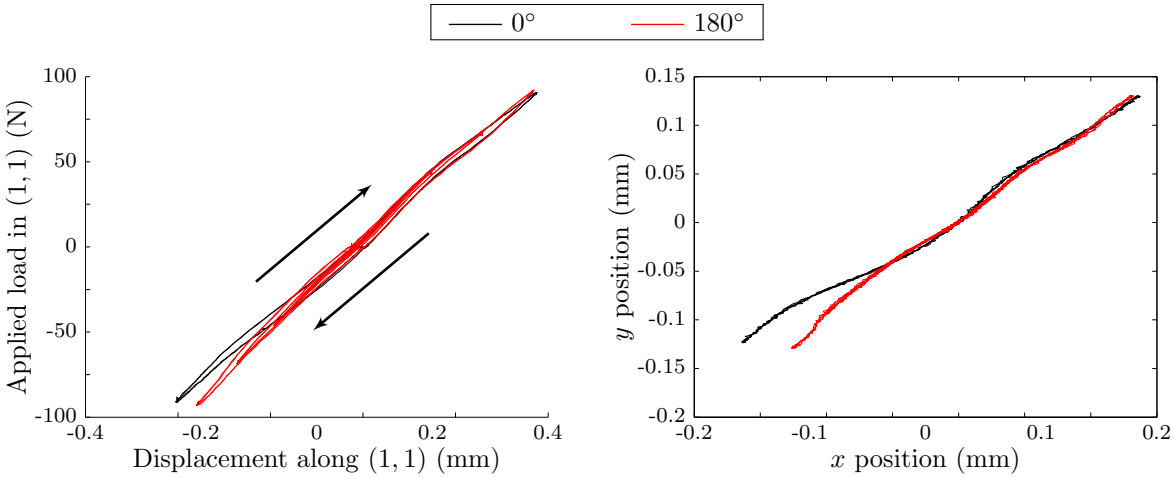

Figure 4.9: Load and displacement relationships for shear experiments at 0° and 180°. Positions from the 180° experiment have been inverted so that the plotted coordinates are in the mast frame.

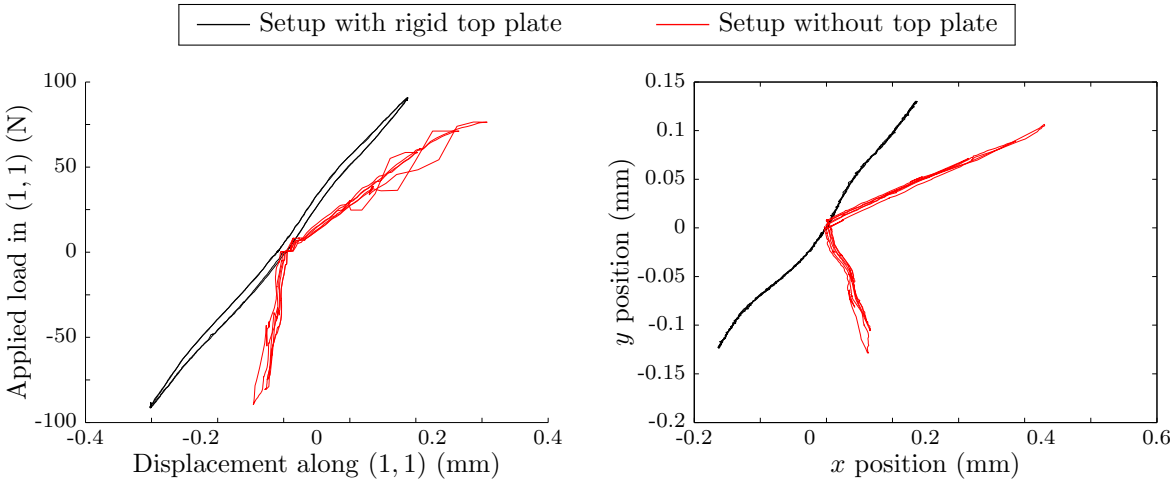

Figure 4.10: Loading and displacement patterns for an experiment with loading of the top plate and a set with loading at the batten square corners. The bend that appears in the data at zero load is a spurious result that arose from the assumption of rigidity of the top batten square, which was actually deforming out of square.

4.3 Biaxial shear loading

One important question is whether and to what degree a preload (such as the loading due to gravity) affects the mast response to transient loads. If the mast were highly sensitive to simultaneous loading of this type, it would imply a need for relatively sophisticated gravity offload systems during testing. In order to investigate this possibility, a second shear experiment was performed.

4.3.1 Experiment

The setup for the biaxial shear experiment used the same parts and methods as the simple shear experiment, with the addition of a third load cable in the $-y$ direction.

A static preload was applied in the $-y$ direction by a weight over a pulley. Loads were applied by weights of approximately 40 N on a metal hanger, and so were of magnitude $0, 53$, and 95 N, sequentially. The two-bay mast used in these experiments would spontaneously unlatch and collapse at between approximately 80 and 130 N of shear force, so these values were very near the edge of the tolerable loads for such an experiment. The transient loads were applied in $\pm x$ by the method describes in Section 4.2.1. Four sets of data were taken in a single session, with static loads of $0, 53, 95$, and 0 N in succession. A time history of the final experiment, under 0 N, is shown in Figure 4.12.

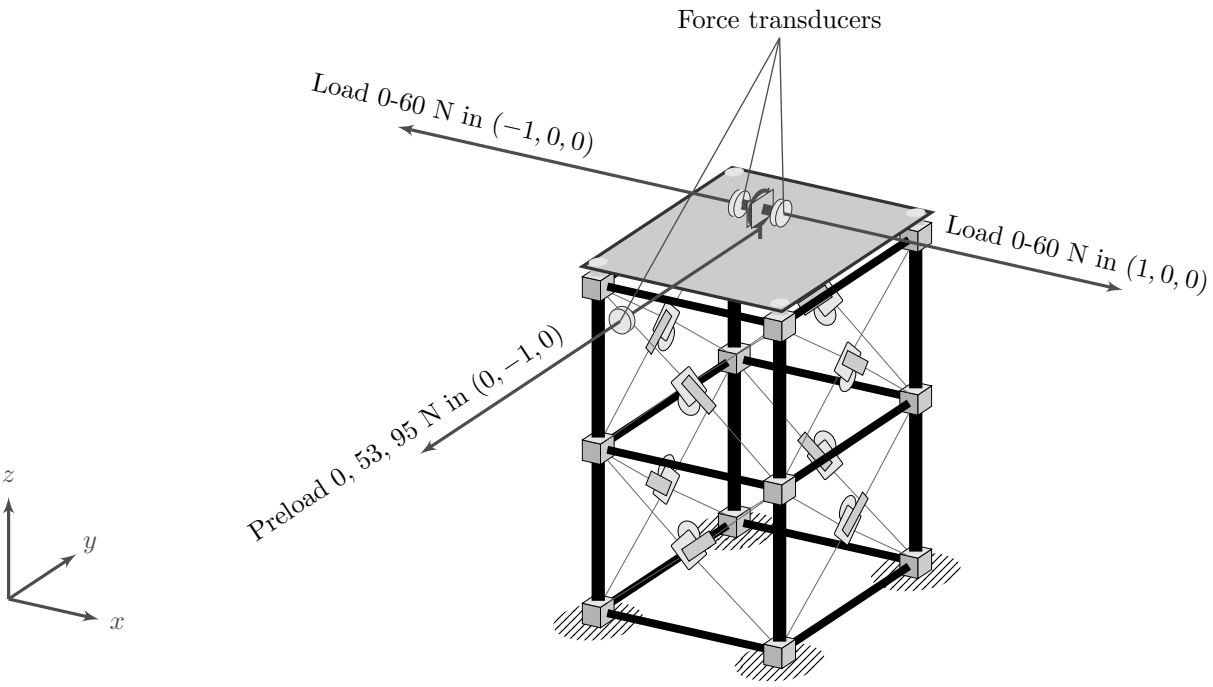

Figure 4.11: Schematic of biaxial shear loading experiment. The x-loading cables lie in a plane 57.5 mm above the center of the top batten square; the y-loading cable is 35.5 mm above the center of the top batten square.

4.3.2 Results

Figure 4.13 shows the key results of the biaxial shear experiment. In order to distinguish the effects of the different levels of load in the $-y$ direction, the first data set is shown for comparison with the three later data sets. Both the force-displacement curves and the path of the node at the center of the top batten square in the x-y plane are shown. The closeness of the applied transient load to the critical collapse load is demonstrated by the widening of the force-displacement curve at high loads, which is characteristic of the change in stiffness as the beads move out of the latch. Only at the highest load of 95 N in the y direction does the response in the x direction appear to change, although at this load an effect is clearly present. This indicates that a gravity offload system need only maintain a modest degree of balance against the load of gravity on the structure to maintain the same stiffnesses and hysteresis effects in this sort of loading.

The x-y displacement plots of Figure 4.13 show two interesting effects: a slight and repeatable waviness in the y displacement, and a sawing pattern that appears as the mast settles into a new y-position. Both are seen to some degree in the simulations of Section 7.3, but are not reproduced exactly. This results raises the same questions about the possibility of a systematic error in the

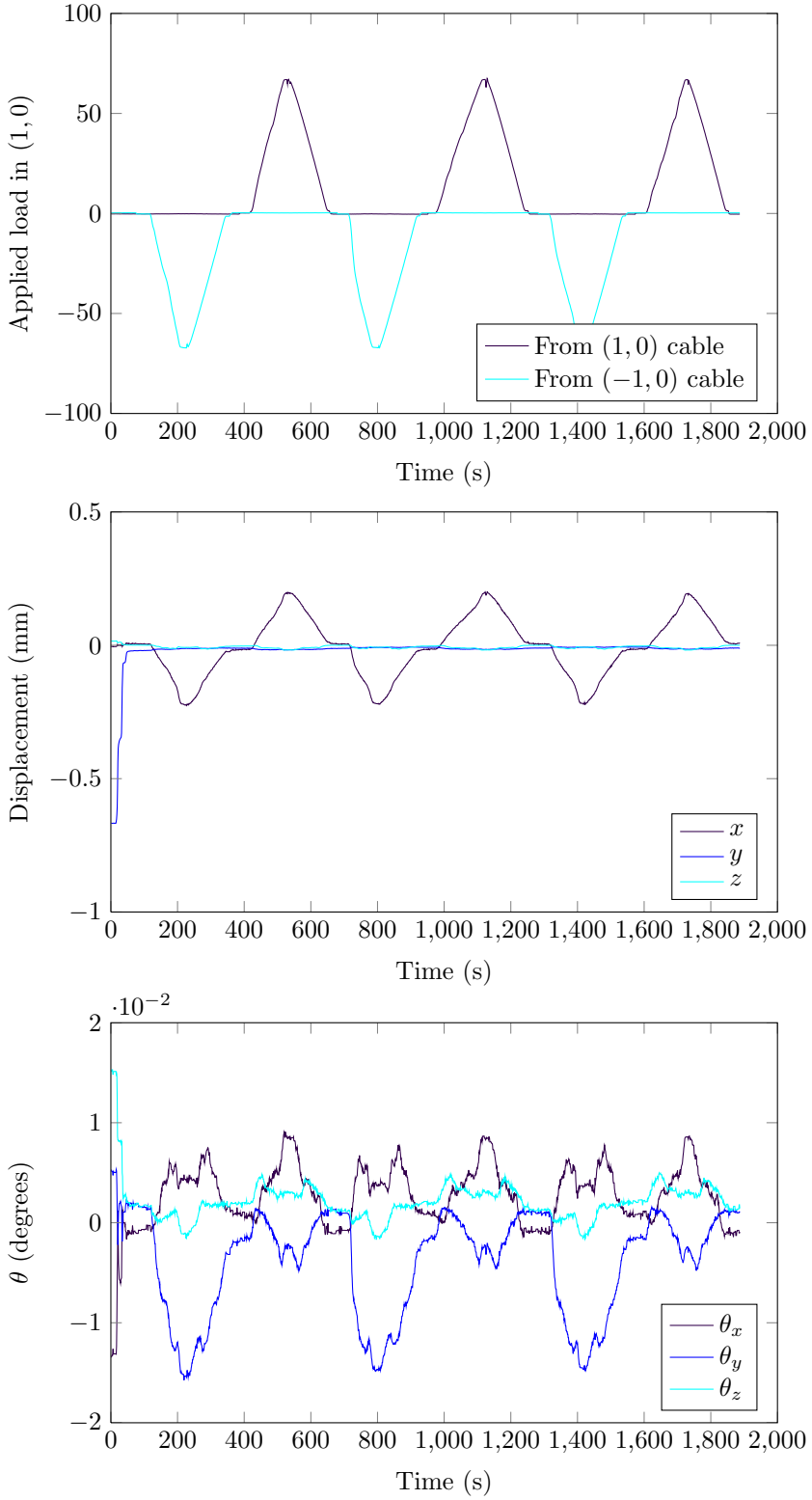

Figure 4.12: Loading and displacement patterns for the final data set of the biaxial shear experiment.

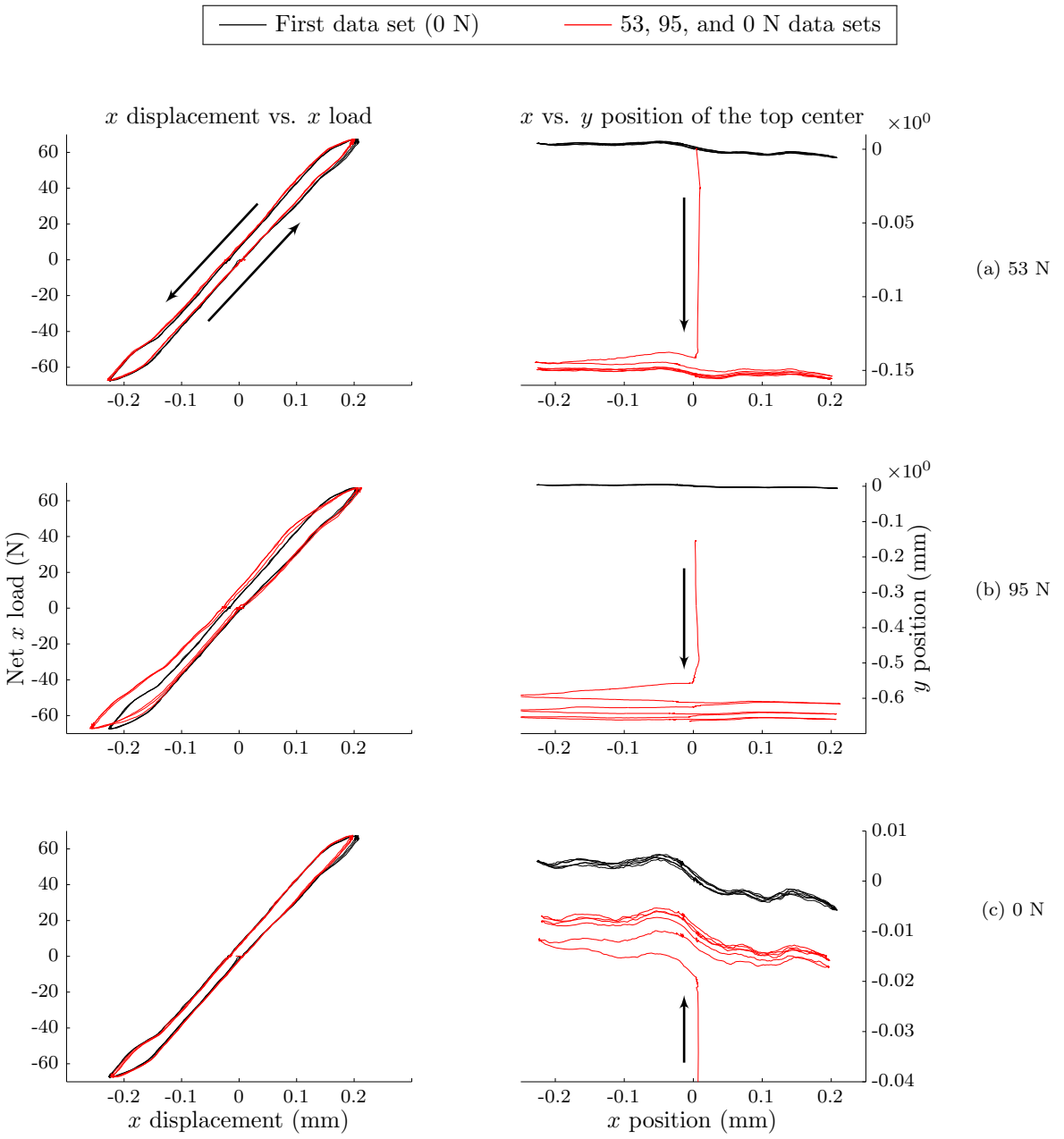

Figure 4.13: Load-displacement and displacement-displacement relationships. The first data set, at 0 N static load, is shown in black (——) on each plot.

measuring system as the simple shear experiments.

Chapter 5

Finite element model

This section describes the computational model that was built using the experimental data of Chapter 3 and a number of calibrated or assumed properties. Standard finite elements were used for much of the structure, and are addressed here, and the most substantial part of the finite element model is a user element that describes the latch, presented in detail in Section 5.2.

The mast generation and initialization are performed using Matlab code, while the user element was written in Fortran for use by Abaqus/Standard. The finite element solution method is driven by Abaqus/Standard. The Matlab code, which is fundamentally for management of the database of part properties and load cases, will be discussed in Section 5.3. First, we will examine the model itself: the elements that form the structure in this finite element model, and the laws governing their connections.

5.1 Basic elements

The primary structure of the finite element model is treated with linearly elastic beam elements. The longerons are modeled as three-dimensional beams (Abaqus element type `B33`) with joints at either end and Coulomb friction in the joints (Abaqus connector element type `CONN3D2`, with `join, rotation`). The batten elements are connected to one another in their squares with perfectly rigid joints. The cables are modeled as linearly elastic truss elements and are only able to carry tension loads, described later in this section.

Table 5.1 summarizes the properties of the longerons and battens, as modeled.

Table 5.1: Properties of modeled battens and longerons.

Longerons		Battens	
Radius	9.6 mm	Radius	6.1 mm
Young's modulus	70 GPa	Young's modulus	220 GPa
Shear modulus	80 GPa	Shear modulus	80 GPa

5.1.1 Corner joints and pulleys

The corner joints of the structure are modeled as rigid bodies. The positions and angles of the batten ends, cable terminations, and longeron sockets are fixed relative to one another using the `*RIGID BODY, TIE NSET` command. The relative positions of these connections were measured on the sample bay as input to the model, so the modeled joints have finite size. The bodies of the pulleys are similarly represented as rigid bodies, connecting the terminations of cables C and D to the intersection point of cables A and B.

5.1.2 Battens and longerons

Because the battens and longerons are required to transmit moments, they cannot be modeled using simple truss elements [42, p. 23.2.1-1]. `B33` beam elements are three-dimensional two-node elements, and activate all the displacement and rotation degrees of each of the end nodes. Euler-Bernoulli beam theory governs the behavior of these elements, which means they are most appropriate for slender beams.[1] The battens can be elastically deformed through bending, as the corners are fully connected, and therefore cannot be modeled with truss elements; the longerons are similarly required to model the rotational friction that is transmitted through their ball joints. The longerons were meshed as six elements and the battens as ten elements.

5.1.3 Ball-end joints

Unlike the battens, which are firmly glued to the corner joints, the longerons are connected to the corner joints by ball-end joints with significant friction. These are treated with `CONN3D2` elements. The `join` [42, p. 25.1.5-29] option of the `*CONNECTOR SECTION` command is used to fix the end of the longeron coincident with the node that represents the socket of the joint. The `rotation` option is used to declare a relationship between the orientation of the socket node and the longeron end

[1] Simulia [42, p. 23.3.3-2] recommends that "For beams made of uniform material, typical dimensions in the cross-section should be less than 1/15th of typical axial distances for transverse shear flexibility to be negligible." The longerons, which are the least slender elements of the sample mast, have an aspect ratio of 15.5.

node, which is specified according to standard Abaqus methods [42, 25.2.5-15].

The friction relationship is simple Coulomb friction, with a single value for both static and kinetic friction. Based on the experiments of Section 3.1, randomly assigned values for μ were used in the longeron joints. The μ values were generated using a normal distribution of standard deviation of 50%, rejecting values below zero. The relationship between the normal load F and the moment opposing relative rotation of the nodes, M, is

$$M \leq \mu r F \tag{5.1}$$

in static friction and

$$M = \mu r F \tag{5.2}$$

when there is relative rotation of the nodes, with r the radius of the longeron ball-end. As modeled, the magnitude of the moment from friction is not dependent on the axis or angle of rotation of the ball end.

5.1.4 Cables C and D

This user element functions identically to an Abaqus truss element (`T3D2`) with the `*NO COMPRESSION` option activated. These cables are idealized as linearly elastic and are able to carry only tension and not bending or compression. As all other elements in this model, they can accept large displacements of their end nodes.

The difference between this user element and the element type provided by Abaqus lies in the length control. The cable user elements consists of two end nodes and one control node, which was used to define the initial length of the element such that if the initial distance between the ends nodes was L_i, and the control node is displaced by u_1 in the x direction, the unstretched length of the cable is taken to be $L_i - u_1$. This makes it possible to gradually adjust the preload in the cable. Abaqus does offer some built-in methods of applying similar effects, but the level of control offered by a user element was preferred.

5.2 Latch user element

The latch user elements connects three nodes: the end of cable A, the intersection point of A and B in the latch assembly, and the end of cable B. It is responsible for the model interactions of cable A-B, the pulley, and the latch. These parts are illustrated in Figure 2.3.

5.2.1 Cable systems

This section describes a general framework for modeling a cable that passes through a set of anchor points where pulleys and latches may be located.. The simplest such system is a series of ideal pulleys. Here an "ideal" pulley is massless, frictionless, and of zero radius.

A cable that passes over any number of pulleys, or latches can be described by breaking the cable into straight segments. The distribution of the cable's length between n sections of cable and the cable tension in each section can then be found by solving a system of nonlinear algebraic equations.

Consider a cable broken into n sections by $n+1$ anchor points at known locations $\mathbf{x_1}...\mathbf{x_{n+1}}$. There is a known constitutive relationship for each section of cable $T_i = T_i(L_i, L_1^0, ..., L_n^0)$, where T_i is the tension in cable section i, L_i is the current (stretched) length of the cable in section i (i.e. $L_i = |\mathbf{x}_{i+1} - \mathbf{x}_i|$), and $L_1^0, ..., L_n^0$ are the unstretched lengths of all the sections of cable. As the cable is redistributed over the pulleys, the values of $L_1^0, ..., L_{0n}$ reflect that redistribution. The total sum of the cable initial length will be constant, and equal to L^0. Finally, each of the $n-1$ pulley or latch elements will have some equation that relates the tension on one side to the tension on the other as a function of the lengths of cable segments (i.e., an equation of the form $\Delta T_i = T_{i+1} - T_i = \Delta T_i(L_1^0, ..., L_n^0)$).[2]

In summary, for n cable sections there are $2n$ unknowns: n tensions and n un-streched length values. There are also $2n$ equations: n constitutive relationships, one length constraint, and $n-1$ ΔT_i relationships across the pulley or latch elements.

[2]This can be extended to functions that are arbitrarily complicated. For example, it might be necessary to include a pulleys with a frictional response that is proportionate to the tension and the rate of motion.

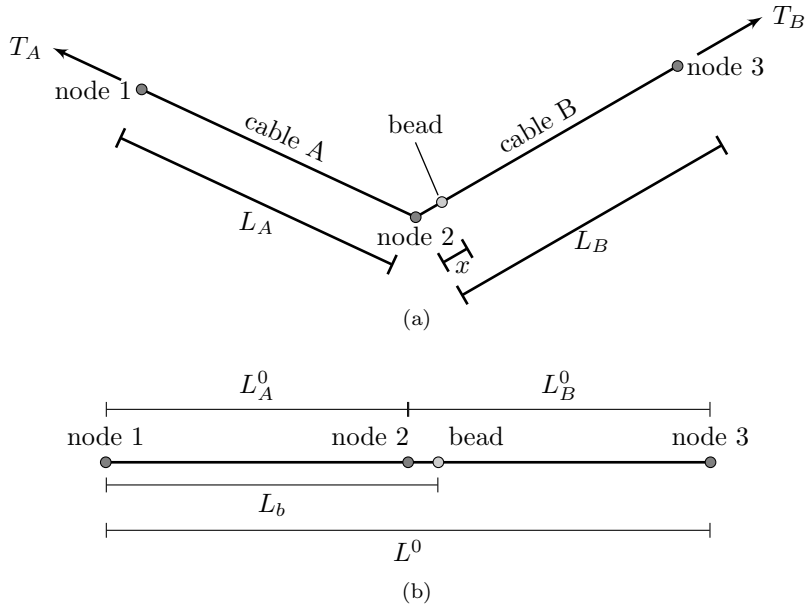

Figure 5.1: Variables for two-section cable. The variables describing the unstretched state are given in (b).

The particular design of the ADAM mast requires a cable going over a single pulley-and-latch unit. The following set of equations were used in the user element:

$$T_A = \begin{cases} 0 & L_A \leq L_A^0 \\ EA\frac{L_A - L_A^0}{L_A^0} & L_A > L_A^0 \end{cases} \tag{5.3}$$

$$T_B = \begin{cases} 0 & L_B \leq L_B^0 \\ EA\frac{L_B - L_B^0}{L_B^0} & L_B > L_B^0 \end{cases} \tag{5.4}$$

$$L_A^0 + L_B^0 = L^0 \tag{5.5}$$

$$T_B - T_A = \Delta T(x), \quad x = L_b - L_A^0 \tag{5.6}$$

Here the cable stiffness EA, total unstretched length L_0, and bead attachment position on the cable L_b are part of the element properties. The details of the function $\Delta T(x)$ are discussed in Section 5.2.2, but when the bead is entirely out of the latch, $\Delta T = 0$, and if the bead were rigidly fixed in the latch such, the equation of ΔT would be replaced by $L_A^0 = L_b$.

This model does not account for the size of the pulley, nonlinear stiffness of the cables, or bending stiffness in the cable. The interaction of the latch and the bead is based on the unstretched length

of cable x, rather than the very slightly different stretched length, and no adjustment is made to the constitutive equation of cable B to account for the difference in tension in the sections on either side of the bead. The solution of these four equations produces the cable tensions and therefore the reaction forces at the three element nodes.

5.2.2 Latch constitutive relationship

The face latching mechanism is modeled on two scales: the mechanism scale, which describes the full range of latch motion, and the backstop scale, which governs the behavior of the ball-and-cone backstop when the latch is fully engaged.

5.2.2.1 Mechanism scale latch motion: analytical model

The latch mechanism can be described as two rollers mounted on elastic cantilever beams. The rollers may rotate with friction about their pins. This mechanism grips a bead that is fixed to the cable that runs through the latch.

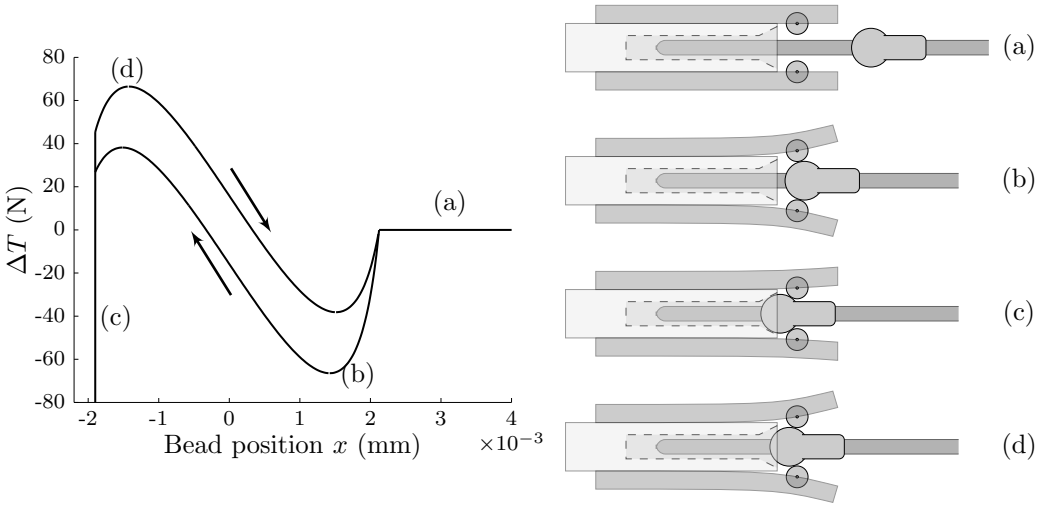

Figure 5.2: Bead positions in the latch.

The assumed geometry of the latch is shown in Figure 5.3. It consists of a bead, two rollers, and a backstop. The bead is attached to a cable, which runs through the backstop of the latch. The system is assumed to remain symmetric about the horizontal centerline.

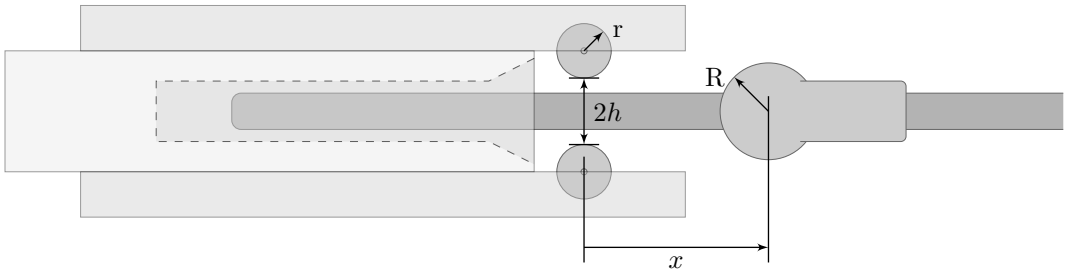

(a)

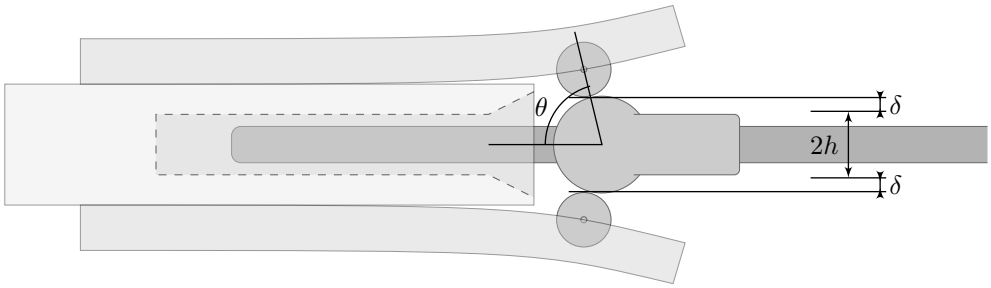

(b)

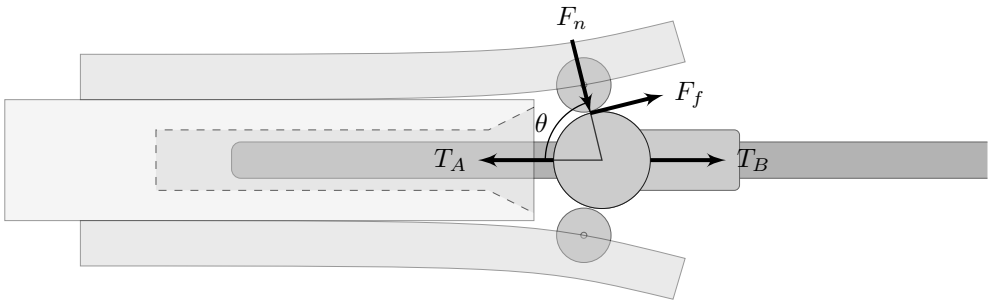

(c)

Figure 5.3: Geometry of the analytical latch model. The geometry of the unstressed latch, without bead contact, is shown in (a). When the bead contacts the latch jaws, it forces them further apart by 2δ, as shown in (b), and the forces of (c) are applied to the bead.

Therefore, while the bead is in contact with the rollers, the following relationship holds:

$$x^2 + (h + \delta + r)^2 = (r + R)^2 \tag{5.7}$$

It is also convenient to introduce the angle between the centerline and the line through the center of the bead and the center of a roller, θ (Figure 5.3b), and note that

$$\cos\theta = \frac{x}{r + R} \tag{5.8}$$

$$\sin\theta = \frac{h + \delta + r}{r + R} \tag{5.9}$$

The rollers are assumed to have a linear stiffness, i.e., it is assumed that the vertical force on each roller required to open the latch by an amount 2δ is $F_{\text{pinch}} = k\delta$, where F_{pinch} is the sum of the vertical components of the forces on the bead.

Now consider the two force components transmitted between the roller and the bead: the normal component F_n and the tangential component $|F_f| \leq |\mu F_n|$ (Figure 5.3c). The kinetic and static coefficients of friction are assumed to be equal, so we need only consider the following equations for the two directions of motion:

$$\Delta T = \begin{cases} -2F_n \cos\theta - 2\mu F_n \sin\theta & \text{if } dx < 0 \\ -2F_n \cos\theta + 2\mu F_n \sin\theta & \text{if } dx > 0 \end{cases} \tag{5.10}$$

where dx denotes an infinitesimal change in bead position and $dx > 0$ corresponds to the bead moving out of the latch. In the third case, $dx = 0$, the bead is subject to static friction, and hence the cable force ΔT must fall between the two extreme values provided by Eq. 5.10.

We can relate δ with F_{pinch}, and thus F_n:

$$F_{\text{pinch}} = k\delta \tag{5.11}$$

$$F_{\text{pinch}} = \begin{cases} F_n \sin\theta - \mu F_n \cos\theta & \text{if } dx < 0 \\ F_n \sin\theta + \mu F_n \cos\theta & \text{if } dx > 0 \end{cases} \tag{5.12}$$

Finally, we can calculate the force balance on the bead with respect to x:

$$\delta = \sqrt{(r+R)^2 - x^2} - h - r \tag{5.13}$$

$$\Delta T = \begin{cases} -2k\delta \frac{\cos\theta + \mu \sin\theta}{\sin\theta - \mu\cos\theta} & \text{if } dx < 0 \\ -2k\delta \frac{\cos\theta - \mu \sin\theta}{\sin\theta + \mu\cos\theta} & \text{if } dx > 0 \end{cases} \tag{5.14}$$

$$= \begin{cases} -2k\delta \left(\frac{x + \mu(h+\delta+r)}{h+\delta+r-\mu x} \right) & \text{if } dx < 0 \\ -2k\delta \left(\frac{x - \mu(h+\delta+r)}{h+\delta+r+\mu x} \right) & \text{if } dx > 0 \end{cases} \tag{5.15}$$

We can see that there are three geometric parameters in this latch model: the roller radius r, the bead radius R, and the initial roller separation h. There are also two constitutive parameters:

the friction coefficient μ and the spring stiffness k. To model a nonspherical bead, we would need only to change the formula for δ.

There is an additional parameter, x_{backstop}, which defines the position at which the bead will come to rest, preventing further motion in the $-x$ direction. This variable is defined in Figure 5.4.

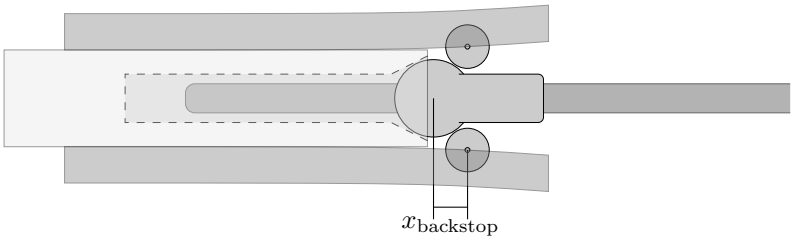

Figure 5.4: Location of the backstop. The value of x_{backstop} is negative, in accordance with the sign convention of the bead position x.

5.2.2.2 Lookup table and blended profile

While the analytical model provides a good fit to most of the experimental latch data, it falls short near the backstop. This is an especially important area because the bead is expected to remain against the backstop during normal use. It is therefore important to include the true experimentally determined profile in the modeled constitutive relationship. The complete latch profile model combines the experimental data and the best fit curve. The lookup table is composed of the experimental data, processed to be monotonically increasing in x and ΔT, with a section that is linearly blended into the fit curve.

Figures 5.5 and 5.6 show typical relationships between the latch profile as modeled and the original experimental data. Twenty-two such profiles were used in the database of latch profiles. Deviations exist to the degree that the experimental data was not monotonic and where the fit curve does not blend perfectly with the experimental data.

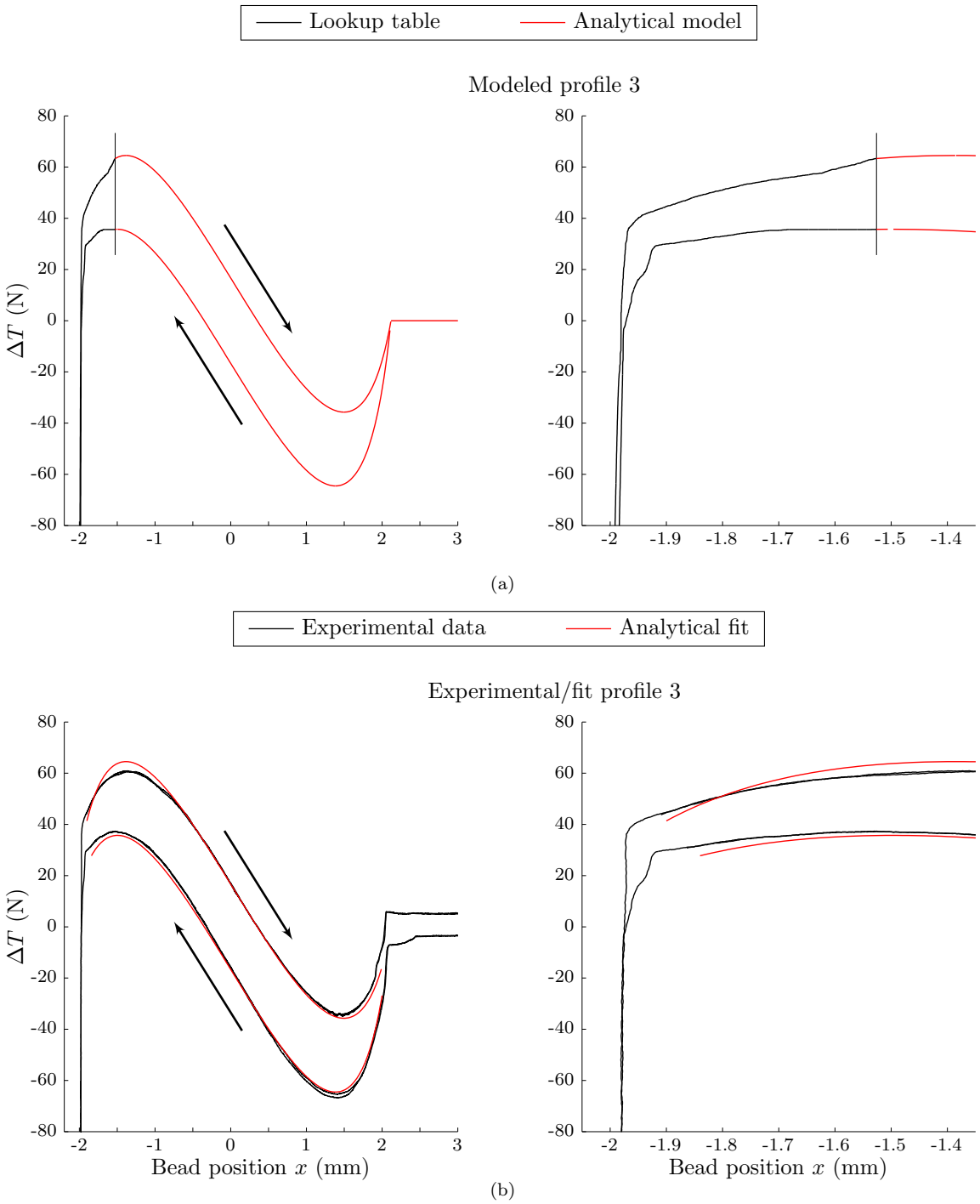

Figure 5.5: A representative latch profile (Latch profile #3). The right-hand graph shows the data near the backstop. In (a) is the profile as modeled, with the lookup table section and the analytically defined section. In (b) is the original experimental data and the fit to that data. Slight differences between the experimental and lookup table data are visible where the lookup table data has been processed to obtain a monotonic relationship.

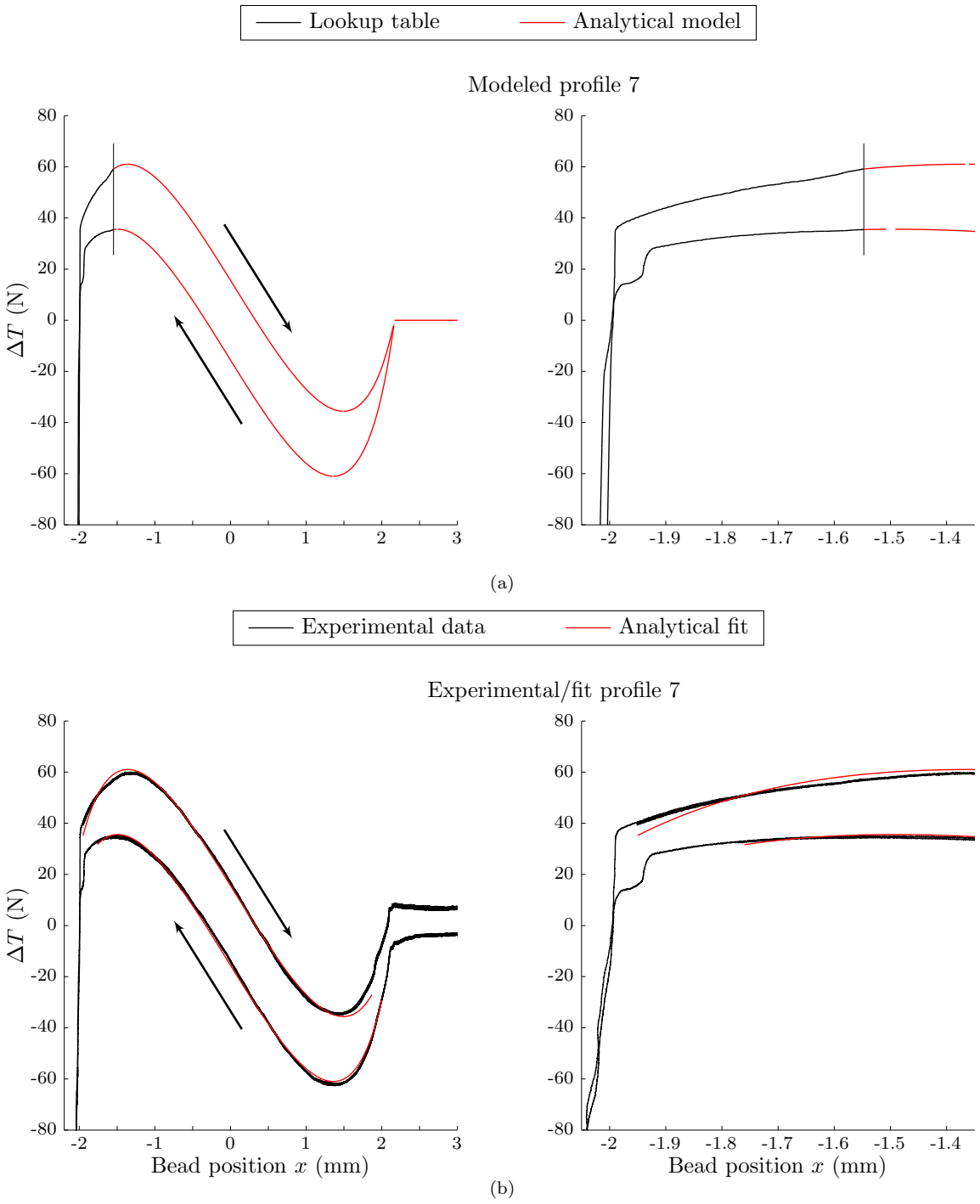

Figure 5.6: Another representative latch profile (Latch profile #7). The right-hand graph shows the data near the backstop. In (a) is the profile as modeled. In (b) is the original experimental data and the fit to that data. Slight differences between the experimental and lookup table data are visible where the lookup table data has been processed to obtain a monotonic relationship.

5.2.3 Formulation of user element

The user element is an application of the Abaqus subroutine capability. Abaqus can call a Fortran subroutine to provide the reactions of an element. In the quasi-static case, this means that the element must provide nodal forces and a stiffness matrix, given information about the state of the element. Figure 5.7 is a flowchart showing the internal structure of the user element.

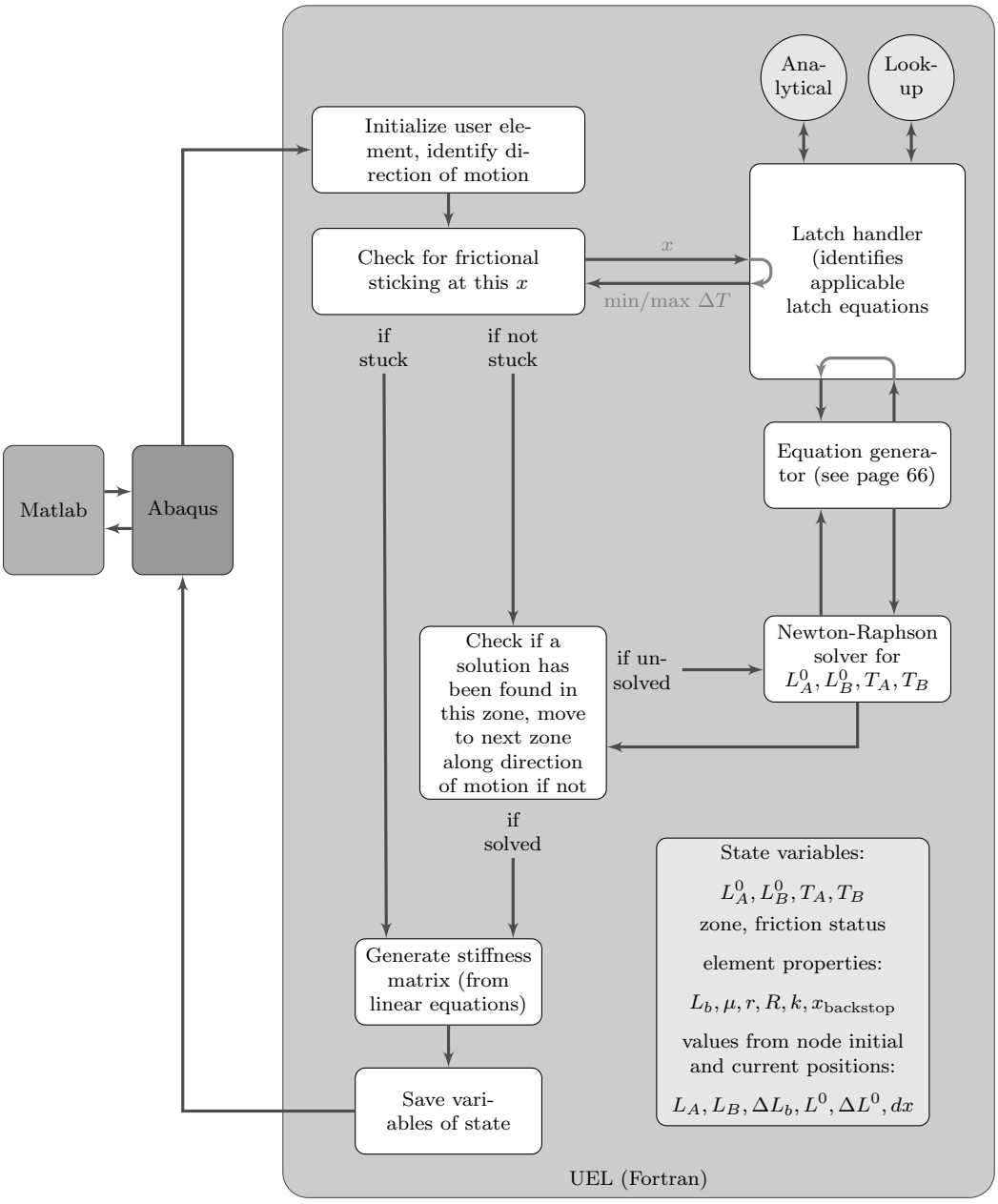

Figure 5.7: User element flowchart

The latch element uses the following inputs from Abaqus:

- `SVARS` contains the "state variables" from the end of the previous step: the results T_A, T_B, L_A^0, L_B^0, direction of motion, and bead zone.
- `JPROPS` contains the integer that indicates which set of properties to use for this element.
- `COORDS` contains the initial position of each node. This is used for L^0_{initial}.
- `U` contains the displacement relative to the initial position of each node. This is combined with `COORDS` to produce the values L_A and L_B. The displacement of the control node is used to establish ΔL^0 and ΔL_b.
- `DU` contains the change in displacement and is used to establish the direction of motion dx.

Seven nodes are used in the latch element. Three nodes are the actual element nodes: the two cable ends and a node representing the latch. Three additional nodes are "dummy" nodes, whose coordinates must be fixed and whose reaction forces are used to report internal variables in a form that can be accessed by the user (Abaqus does not record the values of state variables at each step in the output data). The final node is a control node, which is used to change certain internal properties of the element, namely L_b and L^0, through its nodal displacements.

5.2.3.1 Zones of bead behavior

Because the bead equation $\Delta T = \Delta T(x)$ is not monotonic, it is important to always identify the *correct* solution of the latch equations. It will often be the case that two solutions are possible for given cable endpoints and a given direction of motion: generally one solution has the bead remaining inside the latch and one has the bead outside, while intermediate positions are not possible. It is assumed that the correct solution is the first solution encountered in the direction of bead motion.

To ensure that the correct solution is found, each direction of motion is separated into zones in which the bead equation is monotonic. The equation is extended beyond its zone as a straight line. First, a solution is sought in the zone of the bead's last known position. If the solution places x beyond the limit of the zone, a solution is sought in the next zone along the direction of bead motion. This guarantees that if the bead was last found outside the latch, a solution outside of the latch will be selected before a solution inside of the latch. It also simplifies the work of the Newton-Raphson solver for the equation to be monotonic.

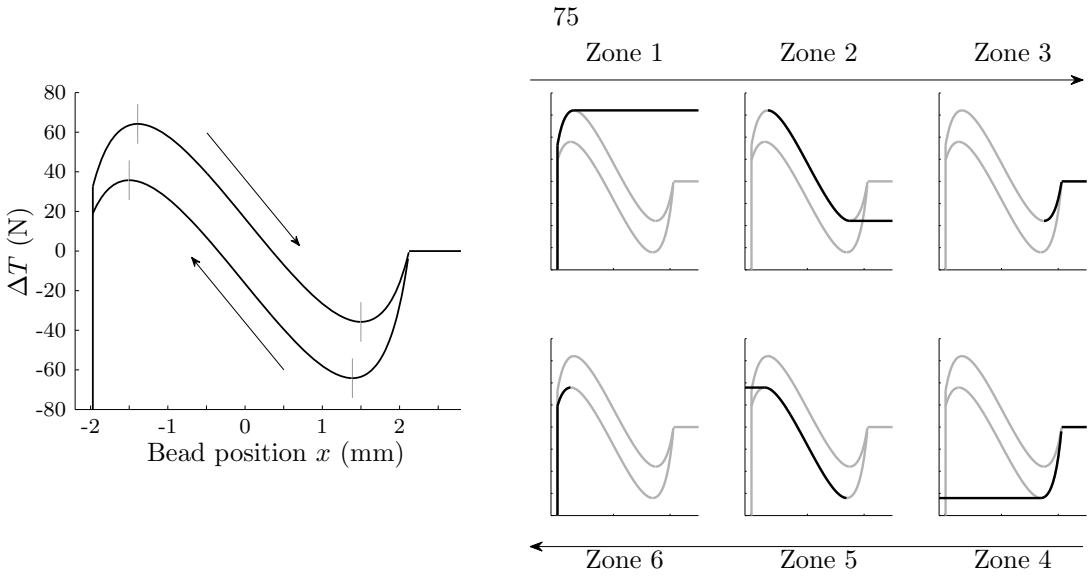

Figure 5.8: An example of the bead zones.

5.2.3.2 Newton-Raphson method and lookup table interpolation

The Newton-Raphson method of solving a nonlinear system of equations was implemented as a subroutine titled `MNEWT`. The code was adapted with slight changes from the example in Numerical Recipes in Fortran [40, p. 272]. Because the equations governing the latch are not convex, a simple relaxed Newton's method [4] was implemented. This substantially improved convergence in `MNEWT`.

To maintain a continuous first derivative within the lookup table, third-order polynomial interpolation was used. The boundary conditions for the function between point $(x_i, \Delta T_i)$ and $(x_{i+1}, \Delta T_{i+1})$ were defined as

$$\begin{aligned} \Delta T(x_i) &= \Delta T_i \\ \Delta T(x_{i+1}) &= \Delta T_{i+1} \end{aligned} \tag{5.16}$$

$$\begin{aligned} \left.\frac{d\Delta T}{dx}\right|_{x_i} &= \min\left(\frac{\Delta T_i - \Delta T_{i-1}}{x_i - x_{i-1}}, \frac{\Delta T_{i+1} - \Delta T_i}{x_{i+1} - x_i}\right) \\ \left.\frac{d\Delta T}{dx}\right|_{x_{i+1}} &= \min\left(\frac{\Delta T_{i+1} - \Delta T_i}{x_{i+1} - x_i}, \frac{\Delta T_{i+2} - \Delta T_{i+1}}{x_{i+2} - x_{i+1}}\right) \end{aligned} \tag{5.17}$$

as a simple way to guarantee slope continuity and maintain the monotonic relationship between x and ΔT.

With the particular equations of this problem, it would have been possible to implement a bisection algorithm for at least some of the range of bead motion. The algorithm would select a

value of x and solve for the difference between the ΔT defined at that bead position by the latch and the ΔT defined at that position by the cable lengths. This strategy was not pursued because the Newton-Raphson solver is more flexible in its applications, but would improve convergence in certain situations.

5.2.3.3 Stiffness matrix

The stiffness matrix **A** is a required output of Abaqus user elements, and is used by the Abaqus solver to estimate the next step solution. **A** is defined by

$$A_{ij} = \frac{\partial F_i}{\partial u_j} \tag{5.18}$$

where **F** are the nodal forces and **u** are the nodal displacements. Therefore, the size of the functional part of **A** (disregarding rows and columns that pertain to dummy nodes and control nodes), is nine by nine. With the solutions of the nonlinear Equations 5.3-5.6, the stiffness matrix can be found from the solution of a set of linear equations as follows.

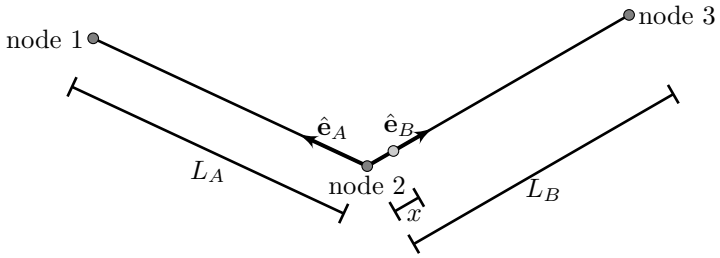

Figure 5.9: Geometric variables of the user element.

First, consider the relationship between **F** and **u**. The reactions and stiffness at node 1 will provide an illustrative example. The other 80 elements of the matrix can be derived analogously. The nodal force at this point is

$$\mathbf{F} = T_A \hat{\mathbf{e}}_A \tag{5.19}$$

where $\hat{\mathbf{e}}_A$ is the unit vector from node 2 to node 1, $\hat{\mathbf{e}}_A = (e_{A1}, e_{A2}, e_{A3})$. This example will continue for the matrix element A_{11}, which relates the reaction force in the first direction at node 1 to displacements in the same direction of node 1.

$$A_{11} = \frac{\partial(T_A e_{A1})}{\partial u_{A1}} \tag{5.20}$$

The unit vector $\hat{\mathbf{e}}_A$ will not be changed by any $\mathbf{u}$ parallel to it. Conversely, T_A is only changed by the motion of $\mathbf{u}$ parallel to $\hat{\mathbf{e}}_1$. Therefore, consider this reformulation:

$$A_{11} = T_A \frac{\partial e_{A1}}{\partial u_{A1}} + e_{A1} \frac{\partial T_A}{\partial u_{A1}} \tag{5.21}$$

$$A_{11} = T_A \frac{\partial e_{A1}}{\partial u_{A1}} + e_{A1} \left(\frac{\partial L_A}{\partial u_{A1}} \frac{\partial T_A}{\partial L_A}\bigg|_{L_B} + \frac{\partial L_B}{\partial u_{A1}} \frac{\partial T_A}{\partial L_B}\bigg|_{L_A} \right) \tag{5.22}$$

$$A_{11} = T_A \frac{\partial e_{A1}}{\partial u_{A1}} + e_{A1}^2 \frac{\partial T_A}{\partial L_A} \tag{5.23}$$

The value L_A is the length of the vector whose unit direction is $\hat{\mathbf{e}}_A$, so $\partial L_A / \partial u_{A1} = e_{A1}$. L_B is not dependent on $\mathbf{u}_A$ at all, so the third term of Equation 5.22 is equal to zero. The value of $\partial e_{A1} / \partial u_{A1}$ is

$$L_A e_{A1} = l_A^0 + u_{A1} \tag{5.24}$$

$$e_{A1} = \frac{l_A^0 + u_{A1}}{L_A} \tag{5.25}$$

$$\frac{\partial e_{A1}}{\partial u_{A1}} = \frac{1}{L_A} + \frac{l_A^0 + u_{A1}}{L_A^2} \frac{\partial L_A}{\partial u_{A1}} \tag{5.26}$$

$$\frac{\partial e_{A1}}{\partial u_{A1}} = \frac{1 + e_{A1}^2}{L_A} \tag{5.27}$$

and so the only remaining term to calculate is $\partial T_A / \partial L_A$. To calculate this, we return to the fundamental equations of the latch, Equations 5.3-5.6. Denoting the partial derivative of the general parameter K with respect to L_A at constant L_B as K', we may differentiate the equations of the

user element:

$$T'_A = \begin{cases} 0 & L_A \leq L^0_A \\ EA\left(\frac{1}{L^0_A} - \frac{L_A}{(L^0_A)^2} {L^0_A}'\right) & L_A > L^0_A \end{cases} \tag{5.28}$$

$$T'_B = \begin{cases} 0 & L_B \leq L^0_B \\ -EA\frac{L_B}{(L^0_B)^2} {L^0_0}' & L_B > L^0_B \end{cases} \tag{5.29}$$

$${L^0_A}' + {L^0_B}' = 0 \tag{5.30}$$

$$T'_B - T'_A = -{L^0_A}' \frac{d\Delta T(x)}{dx} \tag{5.31}$$

which are linear in all the partial derivatives, and are solved by LU decomposition [40, p. 35-37] in the UEL subroutine. Various convolutions of the above derivation apply to other elements of the stiffness matrix.

5.3 Model generation

The strategy for model generation in Matlab is predicated on the repeating and rotationally symmetric nature of the mast. The Matlab code first generates all the elements and nodes, starting with the first side of the first bay, and completing four sides of a bay before starting to generate the next bay. This process is described in Appendix B. Matlab is also responsible for the stochastic part properties and model initialization.

5.3.1 Modeling stochastic variability

Certain mast properties are assigned stochastically. The pretension in the cables, through the cable unstretched lengths L^0, is randomized to match an experimentally identified normal distribution. The friction coefficient in the longeron balls ends is similarly treated. The random number stream, common to all these distributions, is seeded with a new value from the clock with every call to the bay property generator (that is, once per generated mast).

Experimentally, the average tension of the four cables on each bay face has been measured but the individual cable tensions have not. For each bay face i and each of the four cable sections on that face j, the unstretched cable length L^0_{ij} is defined as

$$r_i = \texttt{normrand(0,}\sigma_{\text{face}}\texttt{)} \tag{5.32}$$

$$s_{ij} = \texttt{normrand(0,}\sigma_{\text{cable}}\texttt{)} \tag{5.33}$$

$$L^0_{ij} = L^{\text{initial}}_{ij} + \Delta L^0_{ij \text{ for } T = T_{\text{mean}}} + r_i + s_{ij} \tag{5.34}$$

by calling Matlab's normally distributed random number function, `normrnd(mean, stdev)`. In this equation, L^{initial}_{ij} is the distance between the two end nodes in the locations at which the model is first generated. The distribution variable σ_{face} is the standard deviation of cable length between bay faces, while σ_{cable} is the standard deviation between individual cables.

Values of r_i and s_{ij} that would leave slack cables were discarded. In practice, the values $\sigma_{\text{face}} = 100$ μm and $\sigma_{\text{cable}} = 0$ μm were used. 100 μm is the face-to-face variability that produces an approximately 50 N standard deviation in cable tensions. No cable-to-cable variability was applied because the severely unbalanced cables that arise from large values of s_{ij} were very computationally expensive in the initial steps of the simulations and the experimental data offered no specific guidance on this point.

The friction in the longeron ball-end joints was also generated with a normal distribution, rejecting negative values. A standard deviation of 50% about a mean of $\mu = 0.0375$ was used in this distribution.

Latch data was also assigned with an element of randomness. Blended latch profiles were generated for all the experimental latch data. Of these profiles, twenty-two were selected for use in the database. Rejected profiles were generally removed because the blended profile had an unacceptable shape. Each latch in a model was assigned to a random latch profile. Assignments were independently generated, so duplicates were allowed.

5.3.2 Initializing the mast model

Because the cables are initialized in a pre-tensioned state, some of the initial steps may involve large displacements and not converge successfully. Therefore, an adaptive stabilization scheme was adopted, using the Abaqus `STABILIZE` option. Figure 5.10 shows how this stabilization scheme fits into the overall modeling strategy. The procedure is detailed as follows.

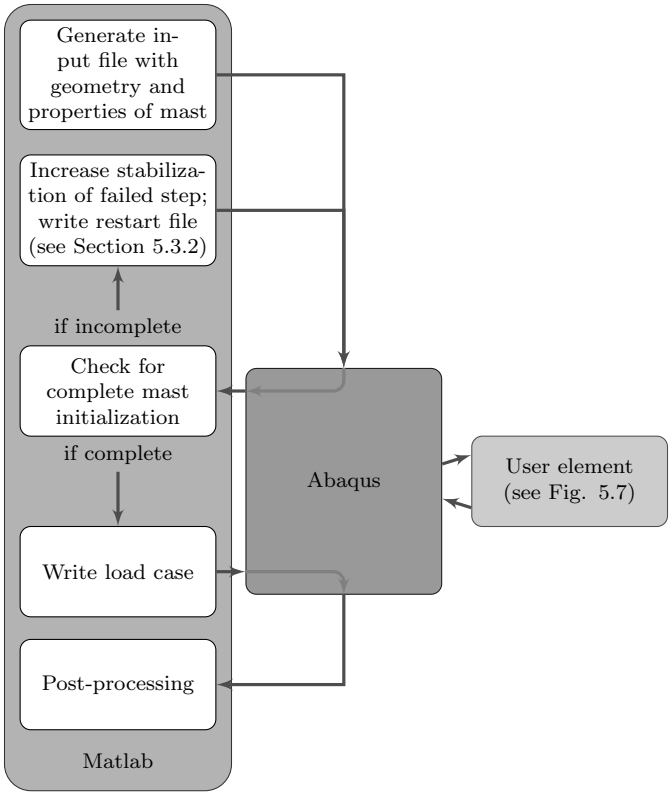

Figure 5.10: Mast initialization and high-level modeling workflow.

1. Write the initial steps:
   (a) Initialize the mast with the positions of all the batten corners and latches fixed and all the cables at the same $L_i^{\text{initial}} - L_i^0 = \Delta L_{\text{avg}}$. Starting with the top bay,
   (b) One at a time, release the four pulleys of this bay
   (c) Release all the corners of the batten square above this bay
   (d) Repeat from (1b) until all pulleys and batten corners are free (except for the four bottom corners)
   (e) Over n steps, "unbalance" the cables such that at step $m = [0, 1, ..., n]$, for each cable i,

$$L_i^{\text{initial}} - L_i^0 = \Delta L_{\text{avg}} + \frac{m}{n}\left(L_{i\ \text{(intended)}} - L_{i\ \text{(intended)}}^0 - \Delta L_{\text{avg}}\right) \tag{5.35}$$

2. Run Abaqus until failure to converge (or internal error of UEL) or completion
3. If file has not completed, determine failure step from `.sta` file
4. Increase stabilization and adjust $L_i^{\text{initial}} - L_i^0$
   (a) If the failure step is unstabilized, insert before it an identical step j with `STABILIZE, FACTOR=10`
   If the failure step is stabilized, insert before it an identical step j with a new stabilization factor of 10 times the current factor
   - If step j is identical to step $j-1$ (the last completed step), but has a stabilization factor below 99% of step $j-1$, apply the average stabilization factor of steps $j-1$ and $j+1$

(b) Set $L_i^{\text{initial}} - L_i^0$ for the new step to the average of the previous step and the current step

5. Rewrite file from step j, headed with `*RESTART, READ, STEP=`$(j-1)$, return to (2)

The initialization stage of a twelve-bay mat is shown in Figure 5.12

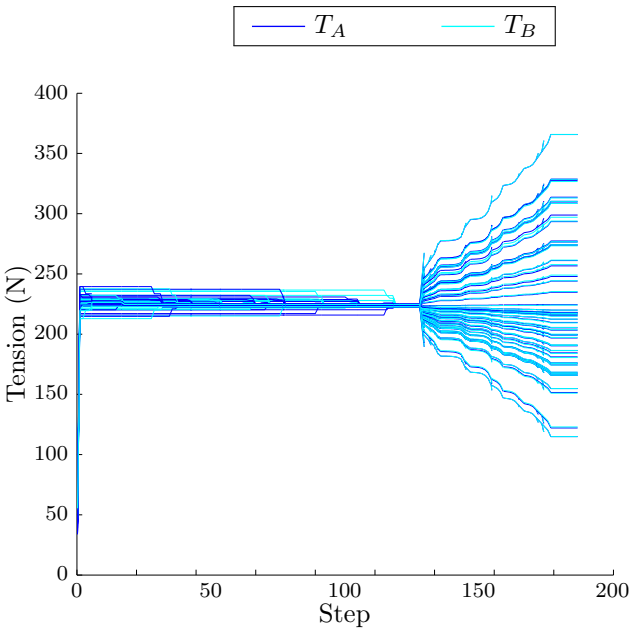

Figure 5.11: Tensions T_A and T_B during mast intialization. Cable unbalancing begins at step 115.

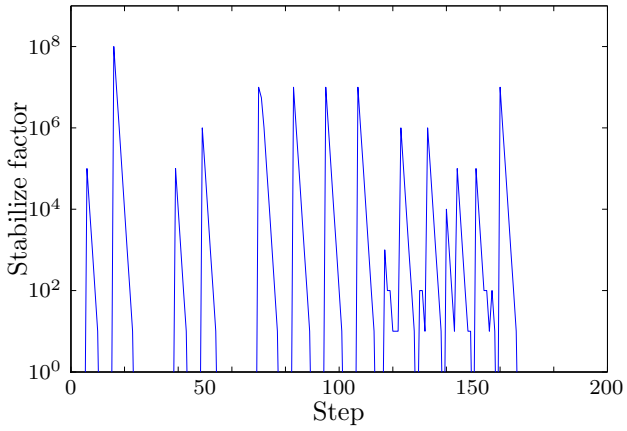

Figure 5.12: Stabilization factors during mast intialization.

Chapter 6

Parametric studies

By varying model parameters, the simulations of this section are intended to illuminate which design elements have the greatest impact on mast behavior and which modeling details are most worthy of computational and experimental time to capture. The following cases were all run for short two-bay masts. There were two reasons for this: it reduced computational time and it allowed for direct comparison with the experimental shear cases.

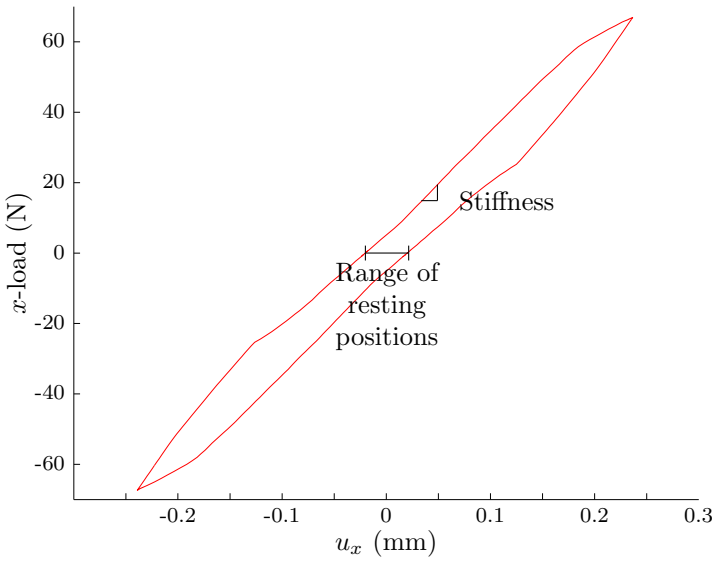

Figure 6.1: Two quantitative measures of mast performance.

The mast tip position is represented by a control node at the center of the top batten square. Most of the simulation cases apply to the mast tip a shear load analogous to the experiment of Section 4.2.2. In these cases, x displacement u_x refers to the displacement of the control node in the x direction, and x load refers to the load in the x direction applied at the control node. Because in

the experiment the load was applied a few centimeters above the location of the theoretical control node, a small moment about the y-axis is also applied.

6.1 Calibration cases

Two parameters were calibrated to measurements made on a two-bay mast: the stiffnesses of the battens was unknown and the friction in the longeron ball ends could be measured only very approximately. One disadvantage of calibrating parameters to full-bay data is that the cases used for calibration are no longer appropriate for validation of the model. Another disadvantage is that this indirect measurement may obscure important variations in the behavior of the parts.

6.1.1 Batten stiffness

Batten stiffness had been indirectly measured by a preliminary shear loading experiment in Section 4.2.2. Therefore, the goal of this parametric study was to identify a batten stiffness that matched the experimental observations. In this experimental setup, the mast had been loaded at its corner joints without a stiffening top plate. Experimentally, displacements were measured at the corner joints, so these are the important displacements for this special load case.

In order to isolate the effect of the deformation of the batten square from the motion of the whole two-bay mast along the direction $(1, 1)$, the displacement of the $(-1, 1)$ corner in the $(1, -1)$ direction is considered. This is labeled d_b in Figure 6.2, and is equal to $d_b = (u_x - u_y)/\sqrt{2}$ from the displacement $\mathbf{u} = (u_x, u_y, u_z)$ of this corner.

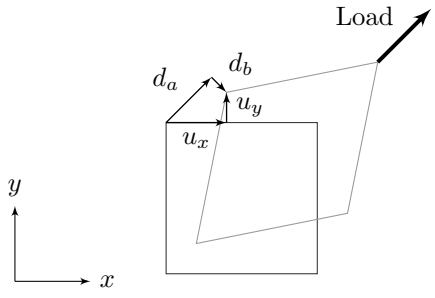

Figure 6.2: Top view of deformation and displacement at the measured batten square corner. The direction of d_a is parallel to the load vector.

This calculation makes some naïve assumptions about the displacement and deformation of the top batten square. In reality, the top batten square does not only displace along the direction $(1, 1)$;

it also rotates and moves out of plane. Both the model and the experiment report the displacements u_x and u_y of the corner joint. The experiment was originally intended to measure the shear motion of the whole mast, rather than to direction measure batten stiffness, and was only later appropriated for calibration of the modeled batten stiffness. This is reason for the indirect nature of the measurement and the low precision of the results.

Figure 6.3 shows results of four levels of batten stiffness overlaid with the experimental measurements. Agreement is excellent in the case $E = 200$ GPa and good for the higher stiffness of 300 GPa. The input load levels to the simulation were transposed, resulting in a slightly high load in $(1, 1)$ and a slightly low load in $(-1, -1)$, which do not affect the conclusions. A value of 220 GPa was selected as the default for other simulations.

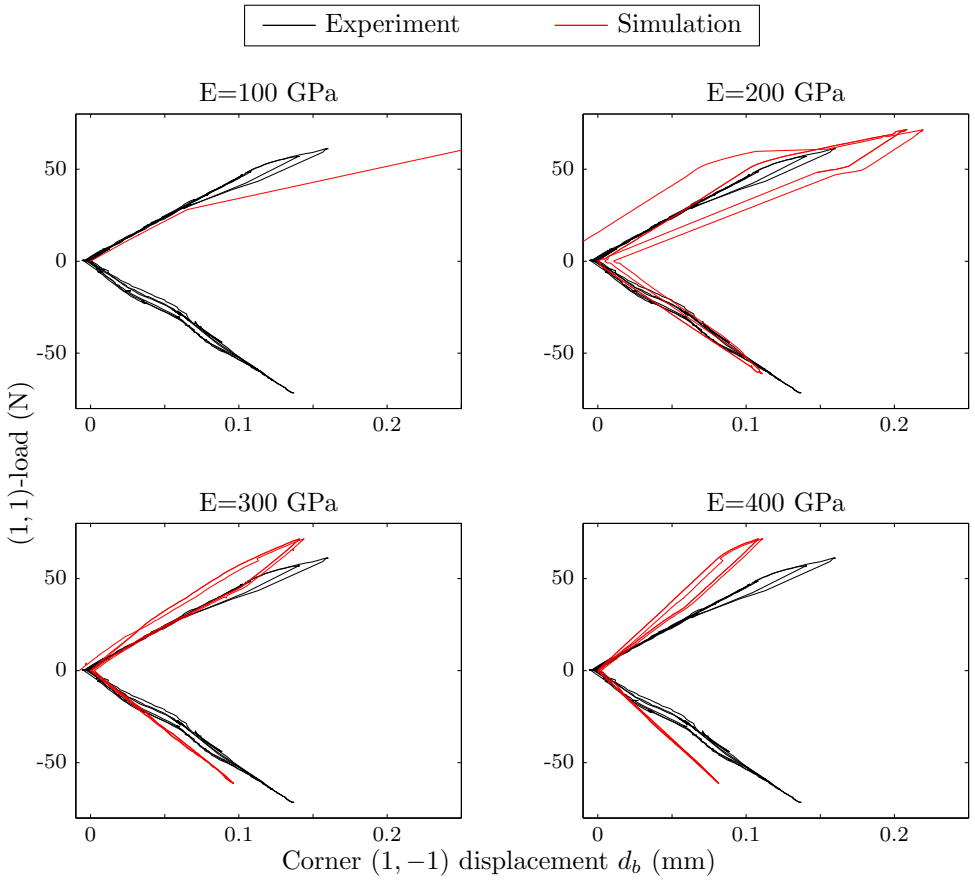

Figure 6.3: Simulation vs. experiment for four values of the batten Young's modulus.

The case of $E = 100$ GPa was not able to solve for the full load, because the simulation found that the mast would delatch and collapse.

Also of note is the asymmetric feature in the top half of the plots. The hysteretic feature that

appears at approximately 30 N in the $(1, 1)$ direction is seen in all the completed model cases and in the experiment. A more basic approach, with a perfectly locked latch, would assume that the bay had twofold mirror symmetry about $(1, 1)$ and $(1, -1)$ and that the two loading directions would therefore be interchangeable. This is not the case, because of the unidirectional latching mechanism. Assuming identical but complex latches, the mast is identical under 90° rotations, but not under reflection. Therefore, it is not safe to assume that the two loading directions will produce the same response at this point on the structure.

6.1.2 Ball-end friction

The frictional behavior of the longeron joints was not clearly determined in the experiments of Section 3.1. This motivated a calibration of the longeron joint friction from experimental measurements of an assembled two-bay mast, and results are calculated using either an experimental value or this calibrated value, as noted. The value of μ for the longeron ball-end joints has a number of subtle effects on the shape of the force-displacement curve. To best illustrate them, values will be compared to the first set of data from Section 4.3, which is a case of shear loading in the x direction. The results are presented as force-displacement curves, with the displacement measured at the center of the top batten square. In the model, a rigid body constrains all four corner joints of the top batten square to move together. Results of this simulation for a number of values of μ are shown in Figure 6.4.

Figure 6.5 shows a number of trials with values of the average longeron joint friction ranging from far below to far above the expected coefficient. The joints have a dramatic influence when they all slip, but above $\mu_{\text{avg}} \approx 0.2$, some combination of joints may lock, producing a structure with very little residual displacement at the level of load considered here. There is a modest jump in mast stiffness of approximately 30% when the longeron joints remain locked, as the mast can maintain a higher load without slipping. Lower friction longeron joints produce a mast whose hysteretic behavior is sensitive to changes in joint friction.

There are at least three features of the force-displacement relationship that can be connected to the value of the joint friction. First is the stiffness of the mast in shear, illustrated in Figure 6.5b: as long as the joints are able to slip under a given load, increasing friction will produce increasing stiffness. Secondly, the residual displacement at zero load, while also dependent on the randomized latch profiles, generally increases with increasing joint friction, as shown in Figure 6.5a. Thirdly, and more subtly, the appearance of latch disengagement in these plots is substantially more prominent

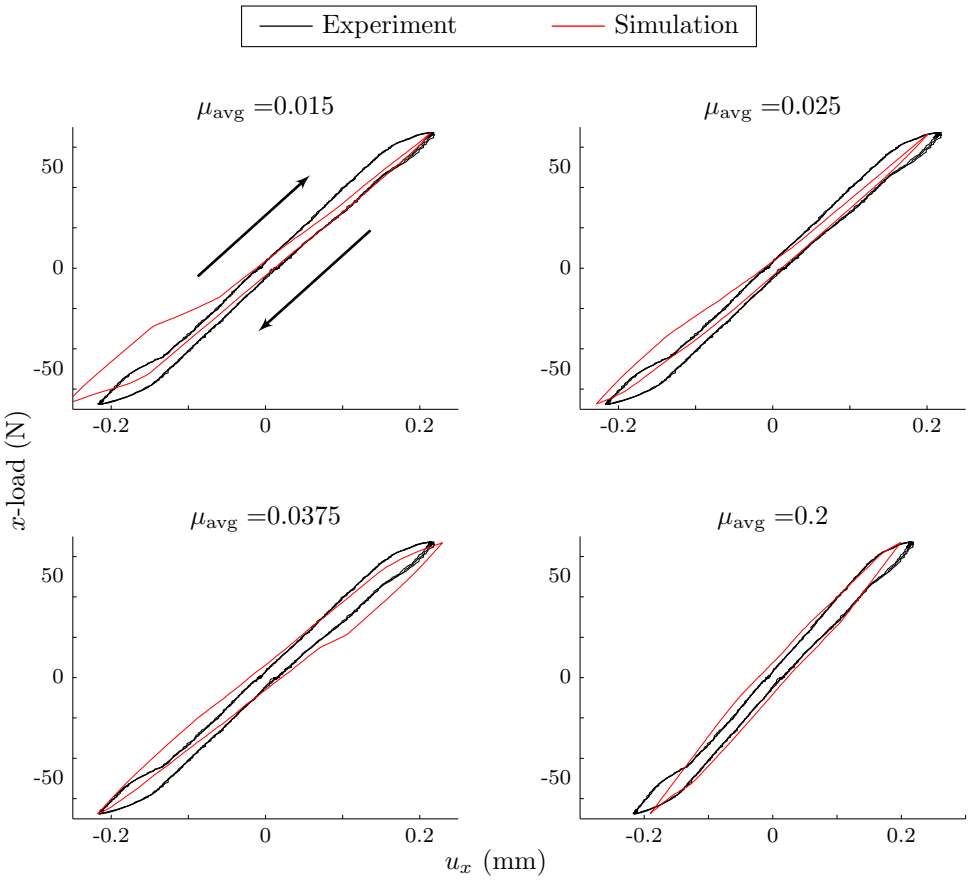

Figure 6.4: Simulation vs. experiment for four values of μ in the longeron ball-end joints.

at lower joint frictions, perhaps simply because the lower stiffness allows more deformation of the mast. This effect is seen in Figure 6.4.

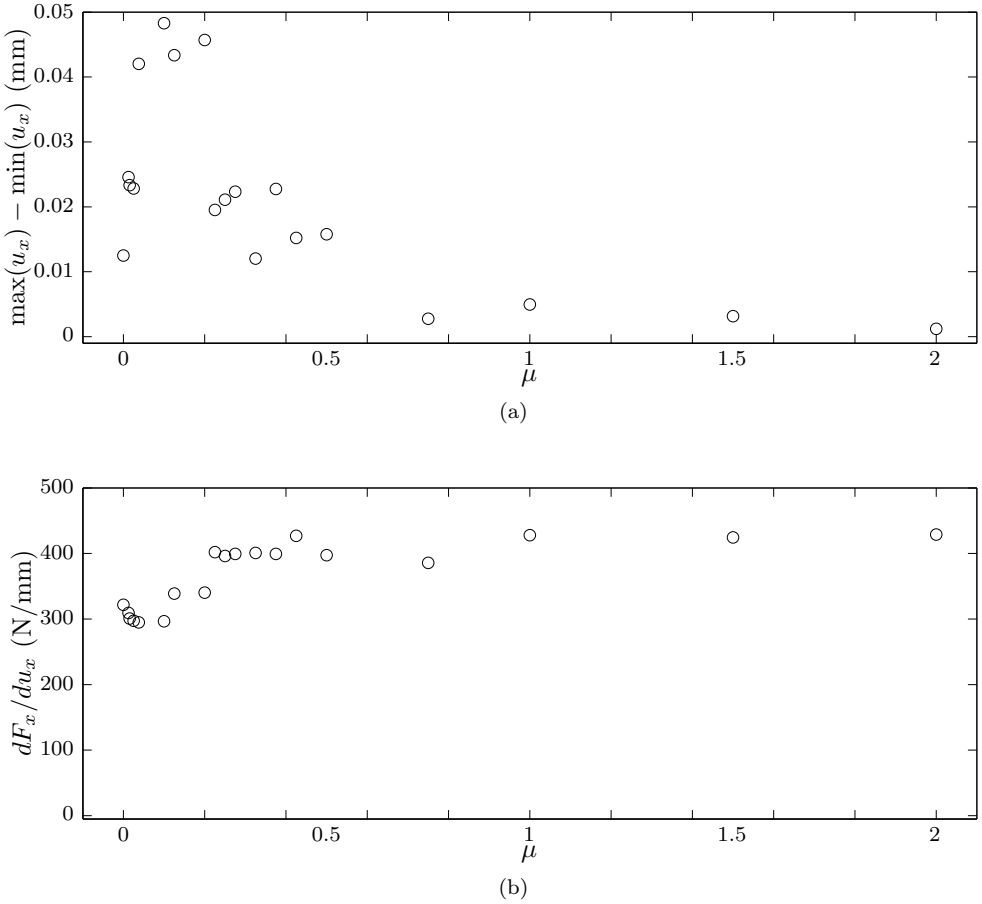

Figure 6.5: Relationships between mean ball-end joint friction coefficient μ and the range of resting positions (a) and mast stiffness (b). The range of resting positions in the experimental measurements of a two-bay mast was 21 μm.

No single value of μ can match all of these variables at once; high values like $\mu = 0.2$ don't begin to disengage the latches at all, which is a clear failure to capture this important behavior. Very low values mildly underestimate the residual displacement and overstate the disengagement of the latches. Moderate values, which are nonetheless quite a bit lower than experiments had indicated, produce a plot with too high a residual displacement and a stiffness lower than indicated by experiments. A value of $\mu = 0.0375$ is used as the default in the remaining parametric studies, and validation cases are presented for both this value and the experimental average of $\mu = 0.14$. It is possible that the discrepancy between the range of resting positions of 21 μm found experimentally and the 36 μm range found at this friction value actually stems from an incorrect value of the friction

in the latches, as encoded in the lookup tables, but the latch data are considered more reliable than the friction data.

6.2 Impact of modeling practices

Computational modeling offers users the opportunity to include an arbitrary level of detail in their analyses, and with that ability comes the question of which details are, in fact, useful. One of the broader goals of this thesis is to identify whether it is important to model the variability in part properties. This section addresses three stochastically modeled properties, ball-end friction, cable preload, and latch behavior. Following these studies, simulations with fully idealized latch behavior are compared with simulations that include the near-backstop lookup tables described in Section 5.2.2.2.

As an additional study, the impact of geometric imperfections in the joint positions, which would be introduced through variability in the longeron and batten lengths, is presented in Section 6.2.5.

6.2.1 Variability in ball-end friction

In the default case, the ball-end friction is assigned, individually, to each longeron joint as $\mu = 0.0375 \pm 0.01875$ with a normal distribution, discarding values below zero. This section compares a set of six x-shear experiments with the default distribution to a set where all joints have the single value $\mu = 0.0375$. The isolated effect of this variability is seen in Figure 6.6.

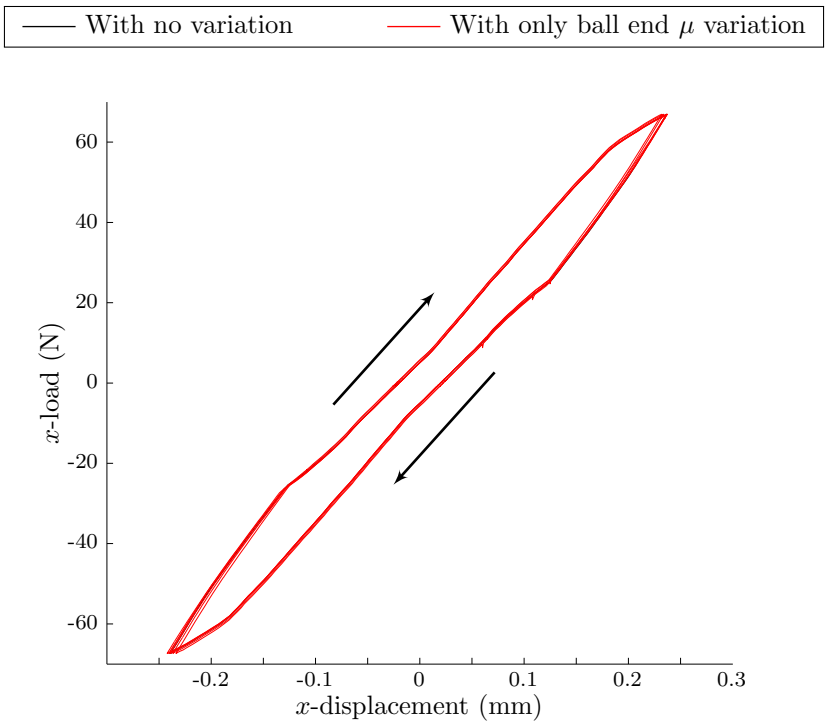

Figure 6.6: Spread in experimental data with and without variation in the ball-end friction. No other properties are randomized.

Variability in μ does produce a measurable effect, but it is very small. As will be seen, the latch variability has a substantially greater impact.

6.2.2 Cable preload - variability

Quite similarly to the ball-end friction variability, the measured preload spread has an identifiable but small effect, seen in Figure 6.7. Selectively removing this variability, as in Figure 6.8, shows that this factor doesn't appear to be the cause of any special features in the force-displacement curve. By elimination, it appears that variability in the latches is the primary source of variability in shear response between two-bay masts.

When ball-end joint friction and latch behavior are both varied, there is no observable impact of including the variability of the cable preloads. Figure 6.8 shows the similarity between these two cases.

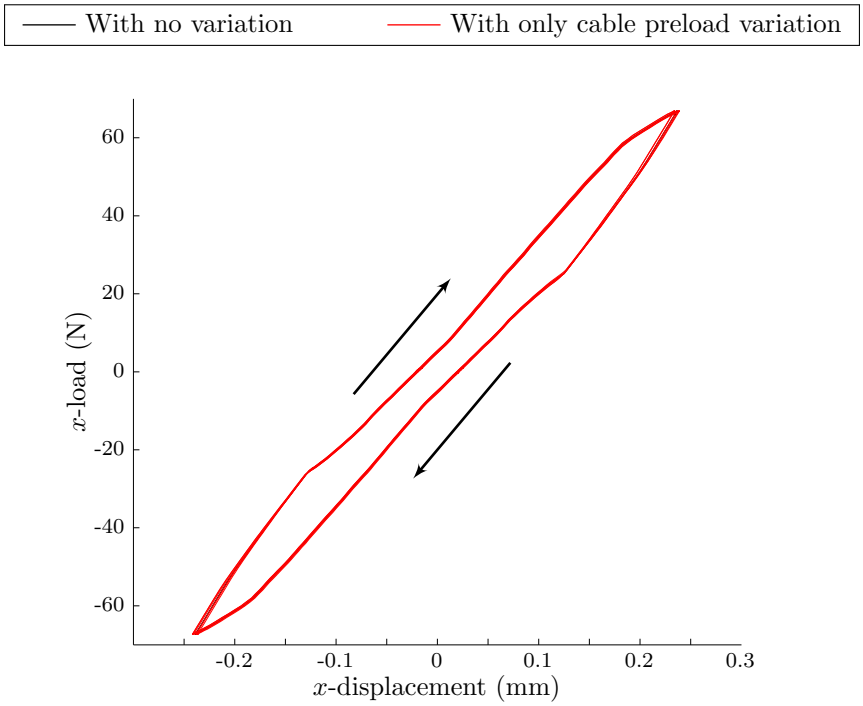

Figure 6.7: Spread in experimental data with and without variation in the cable preload. No other properties are randomized; a single latch model (#3) is used for all faces.

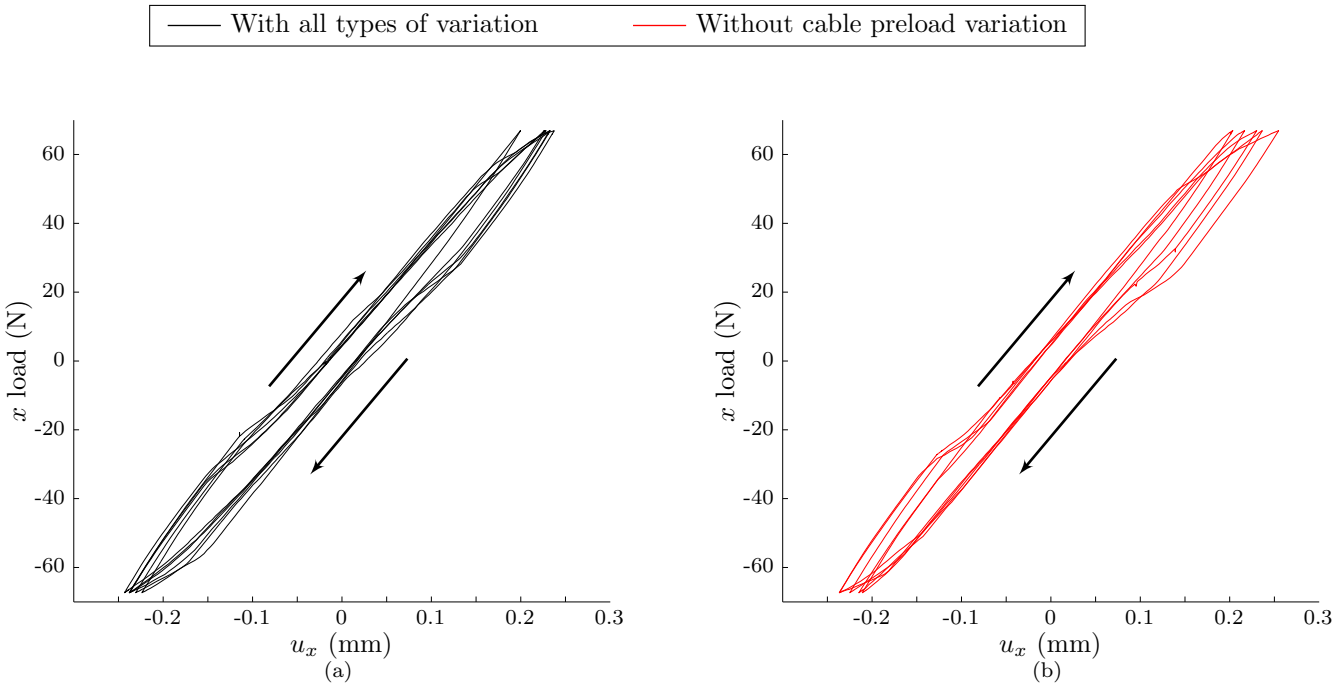

Figure 6.8: Spread in experimental data with (a) and without (b) variation in the cable preload. Ball-end joint friction variation and latch behavior variation are present in all cases.

6.2.3 Latch model - variability

Finally, the impact of the latch variability alone is seen to be substantial. Figure 6.9 shows force-displacement curves for fully randomized latches over a completely unrandomized mast. The unrandomized mast uses latch model #3 on all faces. This result implies that it may be important to maintain the same distribution of latch behaviors between testing and use if this degree of repeatability is required, i.e., to avoid switching latches to different faces between uses.

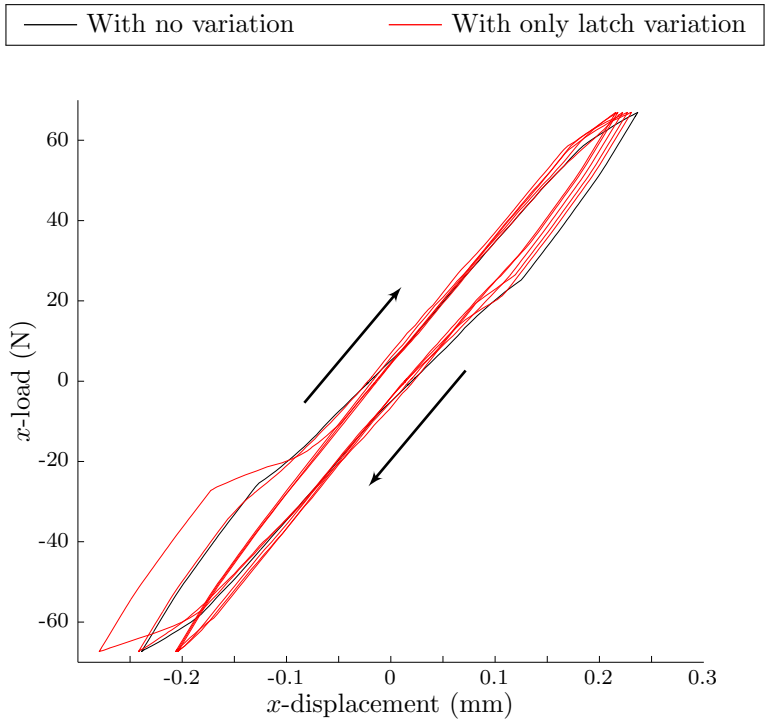

Figure 6.9: Spread in experimental data with and without variation in the latch model. No other properties are randomized.

How can we evaluate these results? One measure of comparison is the width of the curve at zero load. Table 6.1 summarizes this values for the preceding sections. From this, we can see that the variation in the latches is responsible for the majority of the variation in this measure of behavior, for these levels of variability in each property. It may be noted that the variability of 50% in the value of μ for the longeron joints is not well-established from the experiments, and so it remains possible that this is an under- or overestimate.

Table 6.1: Summary of variation in range of resting positions at zero load. Six trials of each type were performed.

Latch model variation	Ball-end μ variation	Cable length variation	Curve width (μm)	Figure(s)
Yes	50%	100 μm	36 ± 9	6.8
Yes	50%	0 μm	35 ± 5	6.8
Yes	0%	0 μm	30 ± 9	6.9
No	50%	0 μm	41 ± 3	6.6
No	0%	100 μm	40 ± 2	6.7
No	0%	0 μm	40 ± 0	6.6, 6.7, 6.9

6.2.4 Measured vs. idealized latch behavior

The baseline case is the use of a randomly assigned selection of the latches with lookup tables described in Section 5.2.2.2. The simulations in Figure 6.10 show the importance of including the lookup tables; the fit lines are not a good match for the near-backstop latch behavior that most strongly influences the mast response at high load. The range of resting positions for a modeled mast with idealized latches was 16 ± 4 μm, attributed to the influence of the longeron ball-end joint friction.

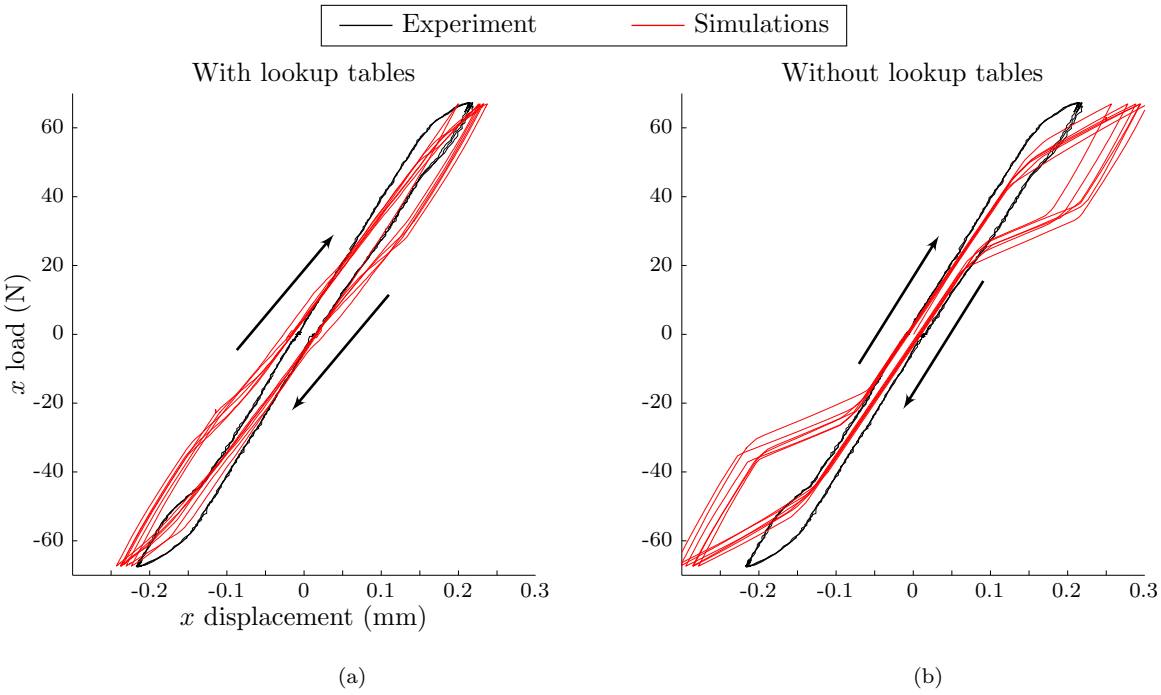

Figure 6.10: Contrast between the use of fit curves and lookup tables near the backstop.

Figure 6.10 also shows that the estimated frictional hysteresis is higher with the lookup tables

than with the perfect backstop. A bead that seats perfectly against an ideally rigid backstop leaves only friction in the ball-end joints as a source of hysteresis.

6.2.5 Geometric imperfections

The baseline case assumes that all battens and longerons are identical in length. We can, however, consider the behavior of a mast in which the battens and longerons are imperfectly aligned. This was accomplished by assigning a small randomly generated offset for each of the joints in the mast in its initial state. Vertical offsets were treated as cumulative along each longitudinal edge and offsets in the x-y plane were treated as independent. To examine the effect of this type of error in corner position, normally distributed random offsets were generated with a standard deviation of 100 μm.

These cases were run to identify whether this might be the cause of the observed off-axis motion in the x-y plots from the simple shear experiment of Section 4.2. Figure 6.11 confirms that this is not the case; including this type of geometric imperfection has no substantial impact on the path. This reinforces the suspicion that there may have been some systematic error in the measurement or loading systems that produced the observed waviness, rather than it being a fundamental property of the mast.

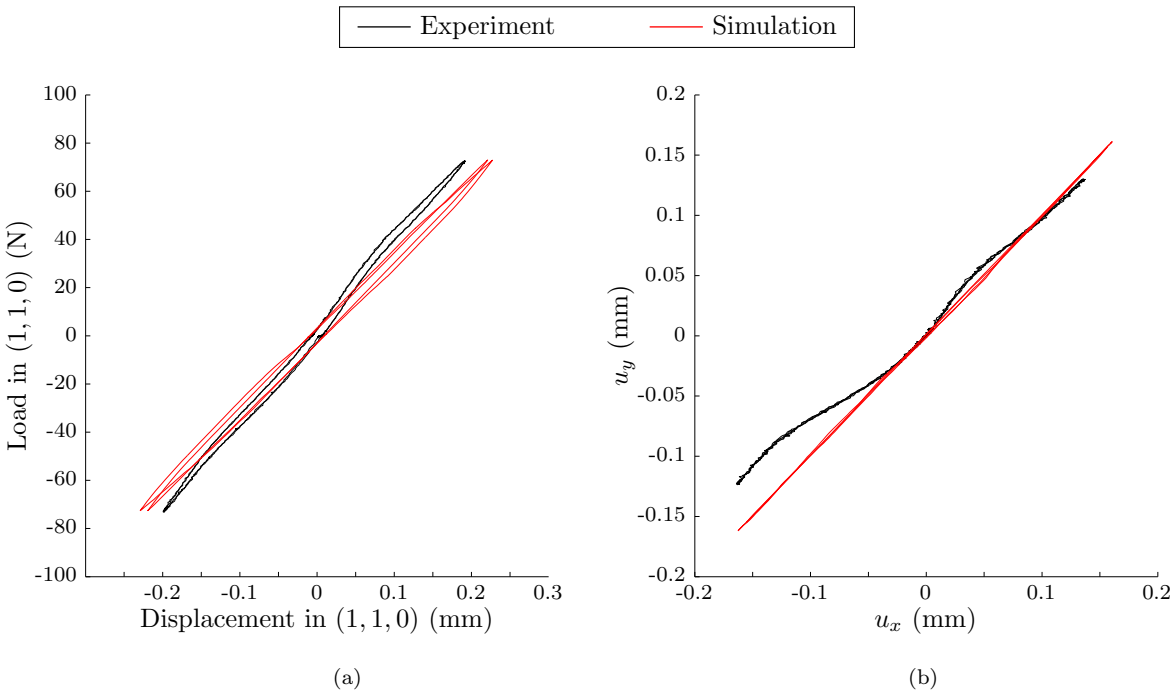

Figure 6.11: Effects of geometric imperfections on the shear response in the $(1, 1)$ direction of a two-bay mast (two trials).

6.3 Component properties

The stiffness and preload of various components may be a practical property to adjust. As might be expected, the cable stiffness has a very direct influence on the mast response to shear. While the primary reason for the focus on shear in this study was simply that shear engages the mast joints more than bending, it is also a relevant case to mast use. A spacecraft pointing maneuver can create a shear load at the mast tip, for example, depending on how the maneuver is powered.

6.3.1 Longeron stiffness

The longeron stiffness has no significant impact on the behavior in shear case, as seen in Figure 6.12. This is unsurprising, as on this short mast, the motion is dominated by the cable-supported shear mode, rather than bending.

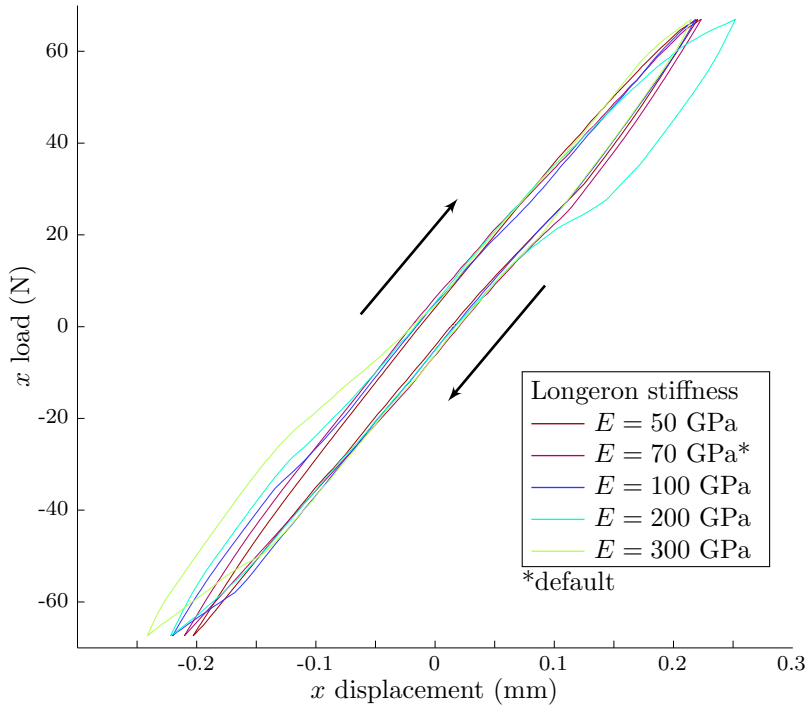

Figure 6.12: Shear response of the two-bay mast at various longeron Young's moduli.

6.3.2 Cable stiffness

The baseline cable stiffness value was taken to be $EA = 73$ N, based on the experimental data of Figure 3.15 in Section 3.3.1. Because the cross-sectional area is only involved in the stiffness calculation in this simulation (the cable is assumed to support only axial tension), stiffness values are considered rather than Young's moduli. This range of simulations is shown in Figure 6.13

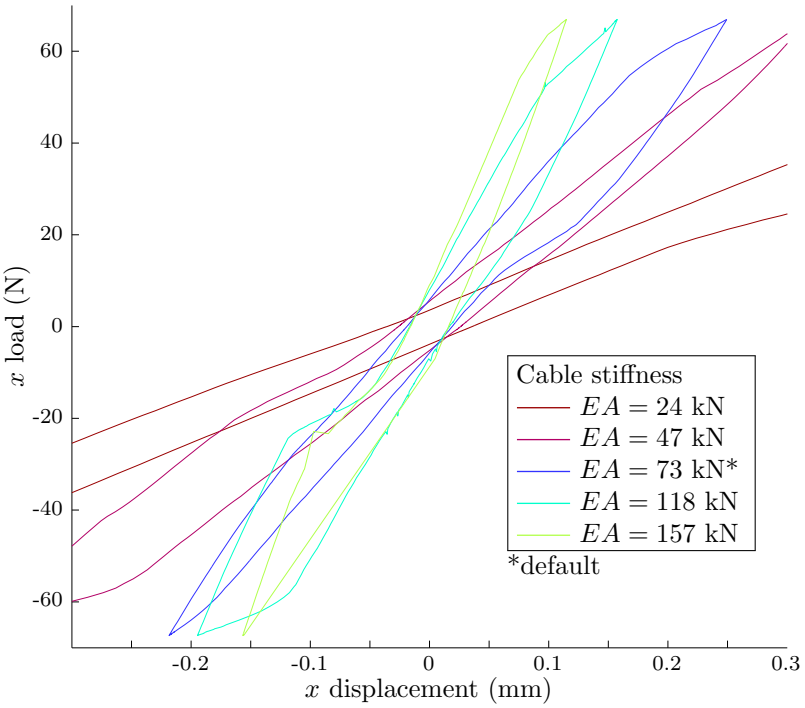

Figure 6.13: Shear response of the two-bay mast at various cable stiffnesses.

The cable stiffness is closely connected to the preload and the preload variability. In these simulations, the same average cable preload was used for all simulations, but the variability in the preload (which is based on a variability in the cable length) was proportionately higher in trials with higher cable stiffness. It should be noted that the range of resting positions is also affected by this variable: as the preload was not changed, the absolute load on the joints remained approximately the same. At the same time, the restoring force from the cables increases with increasing cable stiffness. This effect is summarized in Table 6.2.

Table 6.2: Summary of variation in range of resting positions and stiffness at zero load. The stiffness is considered to be the average of the loading and unloading slopes Δx load $/\Delta u_x$.

Cable stiffness	Curve width at zero load (μm)	Slope at zero load (N/mm)
24	71	100
47	52	210
73	38	310
118	33	450
157	32	560

It is quite clear, comparing Figures 6.12 and 6.13, that the shear response is dominated by the cable stiffness, rather than the longeron stiffness. Unless the ball-end joints are locked in static friction, there is no way for the longerons and battens to resist shear, so the only possible contribution of the longeron stiffness is to resisting the moment response due to the shear force at the tip. Any slight bending in the structure is completely overwhelmed by the shearing motion.

6.3.3 Mean cable preload

The cable preload show a modest impact on the range of resting positions, similar to the results of a proportionate change in the longeron ball-end joint friction. The graphs of Figure 6.14 show this effect, superimposed on the shear experiment.

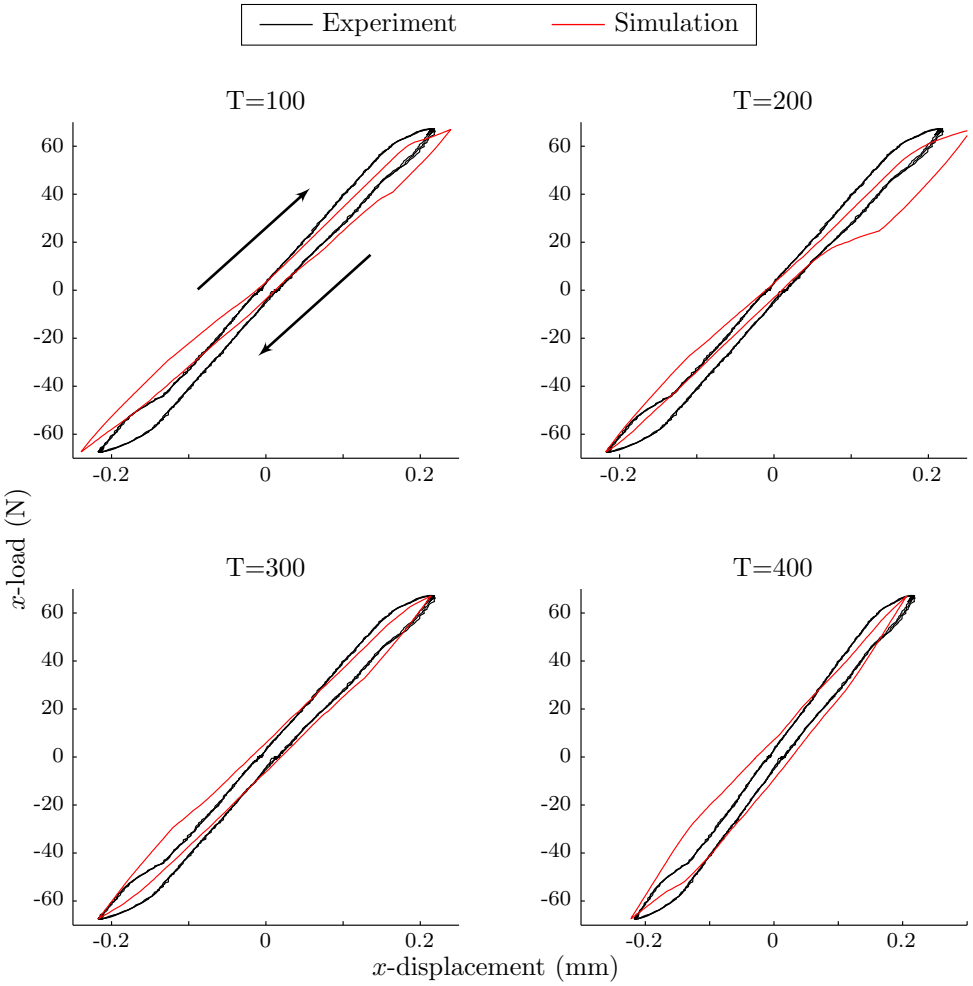

Figure 6.14: Simulation vs. experiment for four values of preload tension in the cables.

The residual displacement at zero load is summarized in Figure 6.15. With this latch model, which introduces frictional effects of approximately the same magnitude as the longeron joints, and with this level of randomness in the longeron joints, the effect of cable preload is not pronounced. A slight correlation with the range of resting positions can be seen in Figure 6.15a.

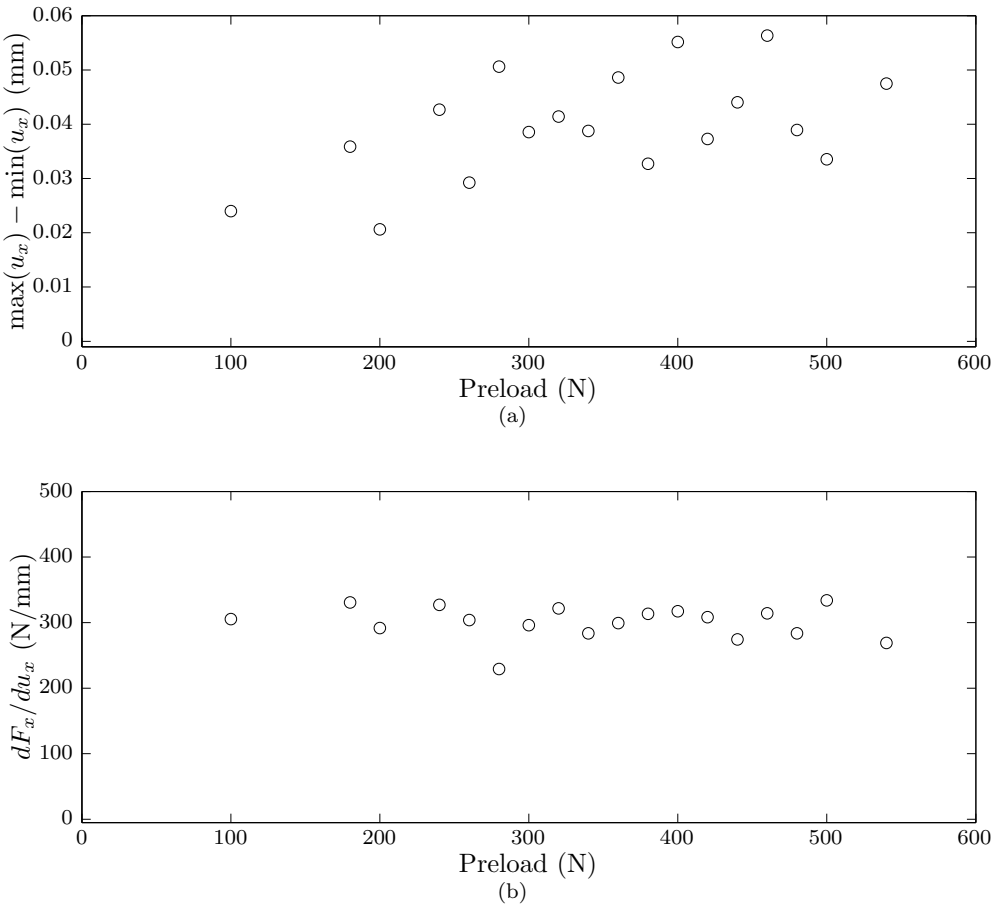

Figure 6.15: Relationships between mean preload and the range of resting positions (a) and mast stiffness (b).

Chapter 7

Validation

Two boundary conditions are common to all validation cases. The four corner joints of the base were completely constrained in all size degrees of freedom using the command `*BOUNDARY`. The four corner joints of the top batten square were joined by an Abaqus `*RIGID BODY`, which is a kinematic constraint locking them to move rigidly with the control node of the rigid body. In all cases, the loading or displacement condition of the simulation was applied to the control node.

The component properties of Table 7.1 were used in all validation cases. Two values of longeron joint friction were considered: a calibrated value of $\mu = 0.0375$ based on full-bay measurements and a value based directly on experiments. The experimental value of $\mu = 0.14$ is viewed with uncertainty because the simulations do not, in general, load the bay joints in the same way as the ball-end friction experiments.

Table 7.1: Component properties for validation cases.

Part	Property	Value
Bay	Height	171 mm
	Width	233 mm
Longerons	Radius	9.6 mm
	Young's modulus	70 GPa
	Shear modulus	80 GPa
	Joint friction	0.0375 ± 0.01875 0.14 ± 0.07
Battens	Radius	6.1 mm
	Young's modulus	220 GPa
	Shear modulus	80 GPa
Cables	Stiffness EA	73 kN
	Preload	220 ± 50 N
Latches	Lookup tables	

7.1 Torsional motion

A one-bay mast was used in this simulation. Displacement boundary conditions in x, y, and θ_z were applied to the control node. These three constraints were taken from the experiment described in 4.1. Because the displacement conditions were partially prescribed by the experimental output, the reaction forces and the unprescribed displacements can be considered outputs of the simulation.

These models show good agreement for the very complex behaviors that take place during this stowage and deployment cycle. The overall curve shape, including the initial unlatching peak and subsequent peaks at the end of unlatching and at the end of the cable relaxation are all captured. The localized friction behavior is also qualitatively captured; small vertical dips in both the experiment and simulation are seen where there was a slight reversal in the direction of motion.

In Figure 7.2b, a closer view of the behavior of the bay under a twisting deformation but without full unlatching demonstrates that the hysteretic response to a change in the direction of motion is captured correctly at any point in the bay motion. This is very important for more realistic load cases, where unlatching is not anticipated.

As was observed during the experiment, only three of the four latches unlock during the modeled torsion case. Figure 7.3 shows the motion of the four beads in their latches for one of the simulations of Figure 7.2a. Latches 1 and 4 delatch first, before 0.5° of motion, and Latch 2 follows, but due to the asymmetry of the motion, Latch 3 is never released. Latches can be considered "released" at $x > 0$ mm, where $x = 0$ mm corresponds to the latch jaws in their widest position and the bead perfectly aligned between the rollers.

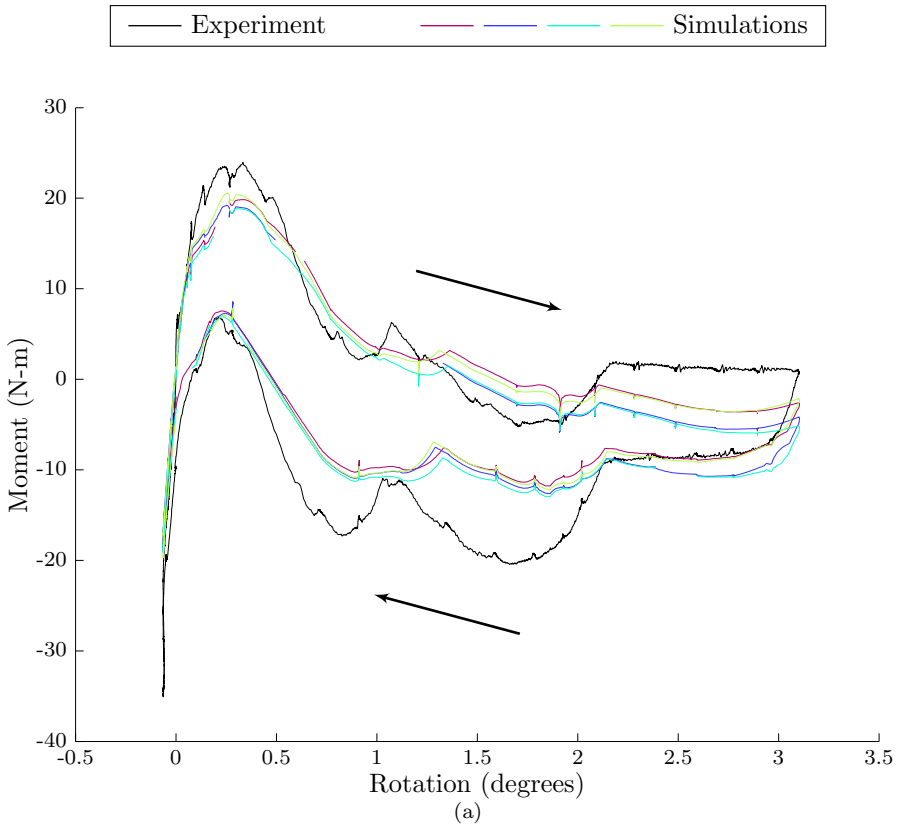

Figure 7.1: Twist vs. moment for the experiment and simulation with the calibrated ball-end friction value. Gaps occur where the simulation failed to converge within the allotted number of iterations. Because the load steps were split into several files, the simulation picks up after skipping the remainder of the previous file. Three models generated with independent stochastic component properties are included in (a), while a single model is run through multiple loops of torsion in (b).

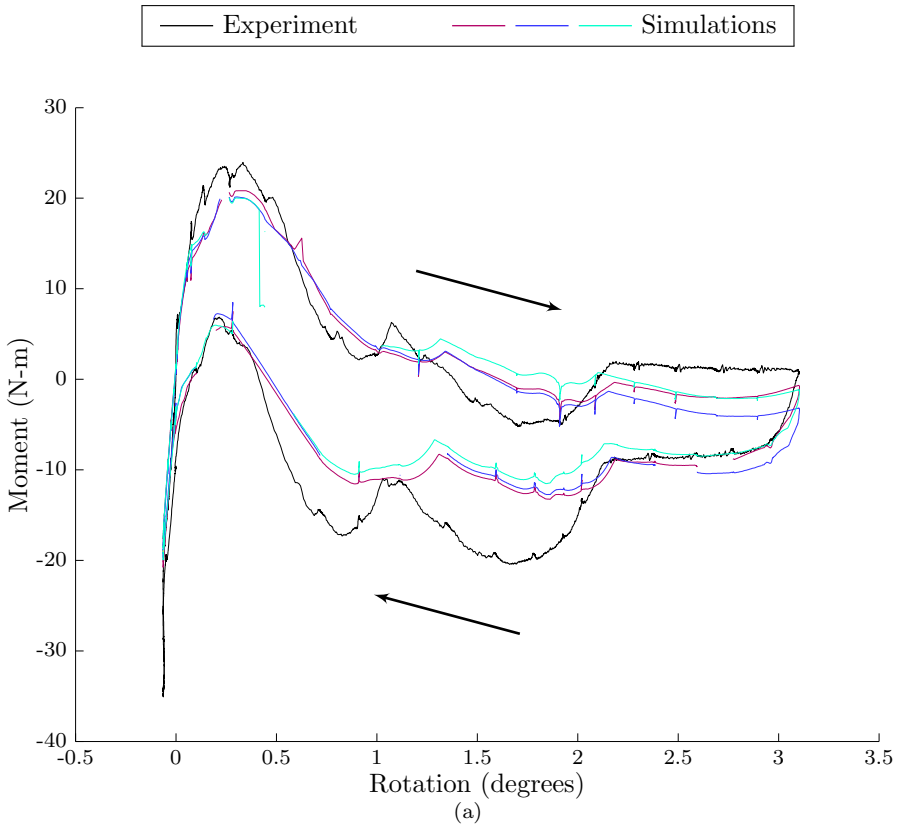

(a)

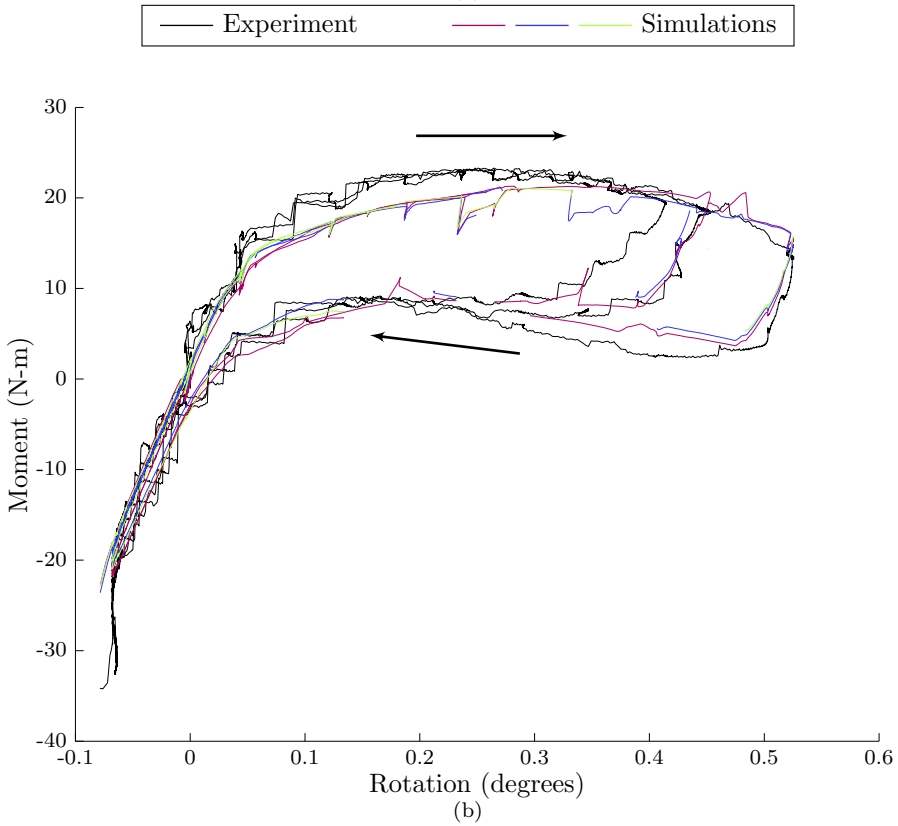

(b)

Figure 7.2: Twist vs. moment for the experiment and simulation with the experimental ball-end friction value.. Gaps occur where the simulation failed to converge within the allotted number of iterations. Because the load steps were split into several files, the simulation picks up after skipping the remainder of the previous file. Four models generated with independent stochastic component properties are included in (a), while a single model is run through multiple loops of torsion in (b).

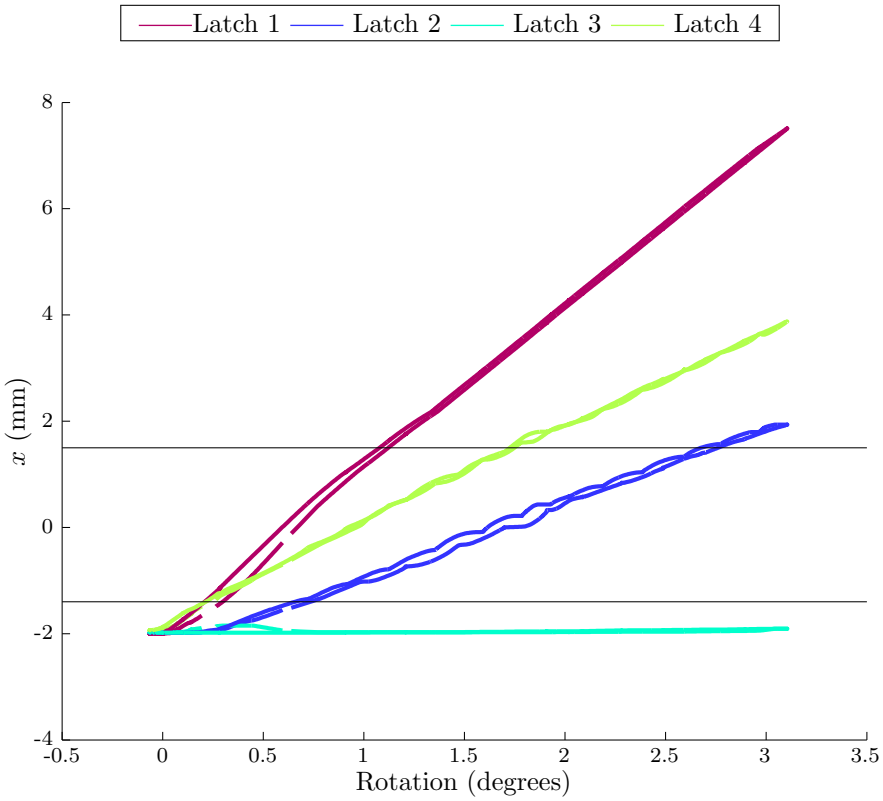

Figure 7.3: The motion of the four beads in their latches for a torsion simulation. The lines $x = -1.4$ mm and $x = 1.5$ mm, where the beads transition from zones 1 to 2 and 2 to 3, respectively, are marked with horizontal lines (——).

7.2 Shear loading

This section validates the model against the experiment of Section 4.2. The boundary conditions of the experiment were imposed upon the simulated model as follows: the four corners of the base were fixed in all six degrees of freedom, and the top four corners were connected to one another by a rigid body.

Loading was applied to the control node at the center of the top batten square. The load was a combination of shear and moment, calculated in Matlab to be equivalent to a shear load applied at the eyebolt in the actual experiment. The magnitude of the loads were based on the maximum experimental loads, but intermediate loads were applied linearly. The result of this simulation is shown with the experiment in Figure 7.5 for six simulations with independently generated stochastic properties.

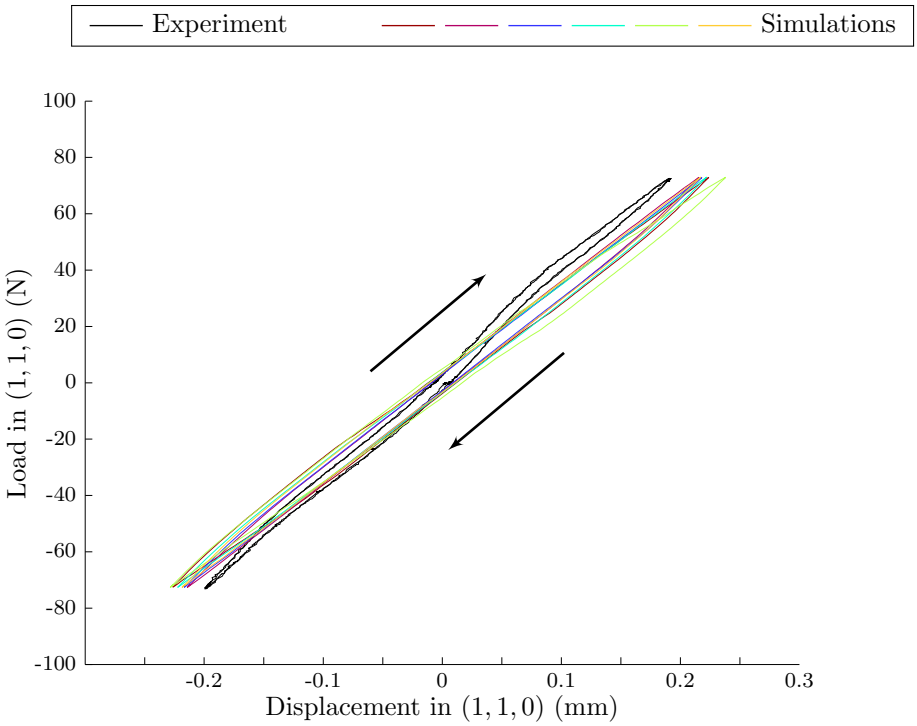

Figure 7.4: Force-displacement curve for shear in the $(1, 1)$ direction for six two-bay mast models with stochastic component behaviors and the calibrated ball-end friction value $\mu = 0.0375$.

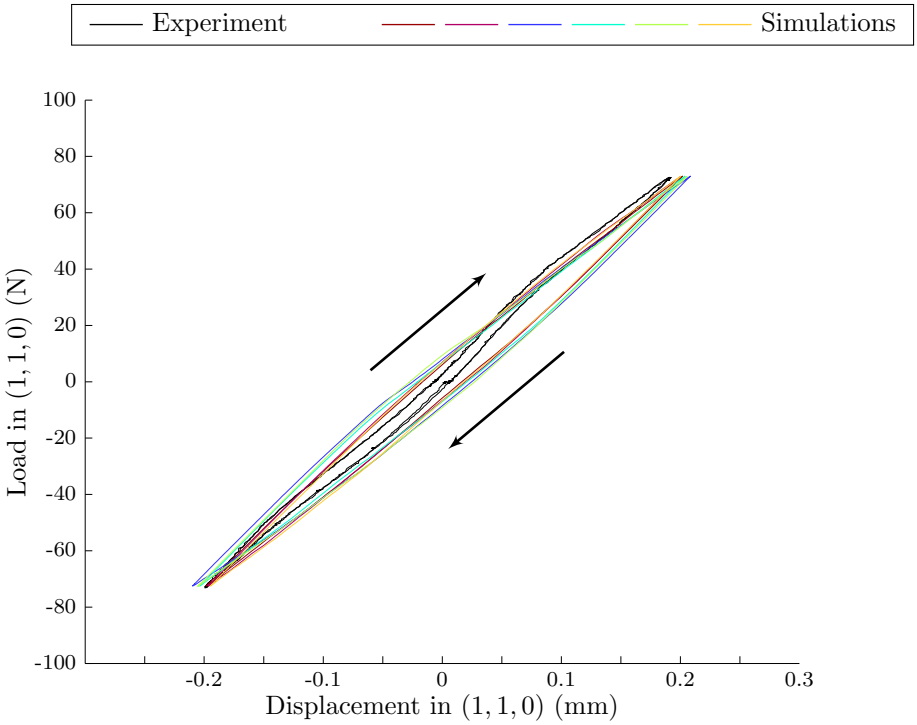

Figure 7.5: Force-displacement curve for shear in the $(1, 1)$ direction for six two-bay mast models with stochastic component behaviors and the experimental ball-end friction value $\mu = 0.14$.

As was noted in Section 6.2.5, this model does not capture the wavy displacement pattern, which is believed to be an error of the experimental measurement system. The most significant point of agreement between the experiment and the model is that the displacement curve does not show any of the distortions associated with delatching. In this load case, the model correctly predicts that the beads remain against the backstops and do not produce the characteristic widening of the force-displacement curve that is seen when the latches begin to disengage. This is interesting because similar loads in the $(1, 0)$ direction do engage complex latch behaviors.

7.3 Biaxial shear loading

A two-bay mast was modeled in this validation case, which is a slight modification of the previous case. As in the experiments of Section 4.3, the loading case was shear in the x direction. In these simulations, there was a simultaneous shear load in the $-y$ direction, and the goal was to evaluate whether these responses are highly coupled. Figures 7.6 and 7.7 show the simplest case of zero load in the y direction.

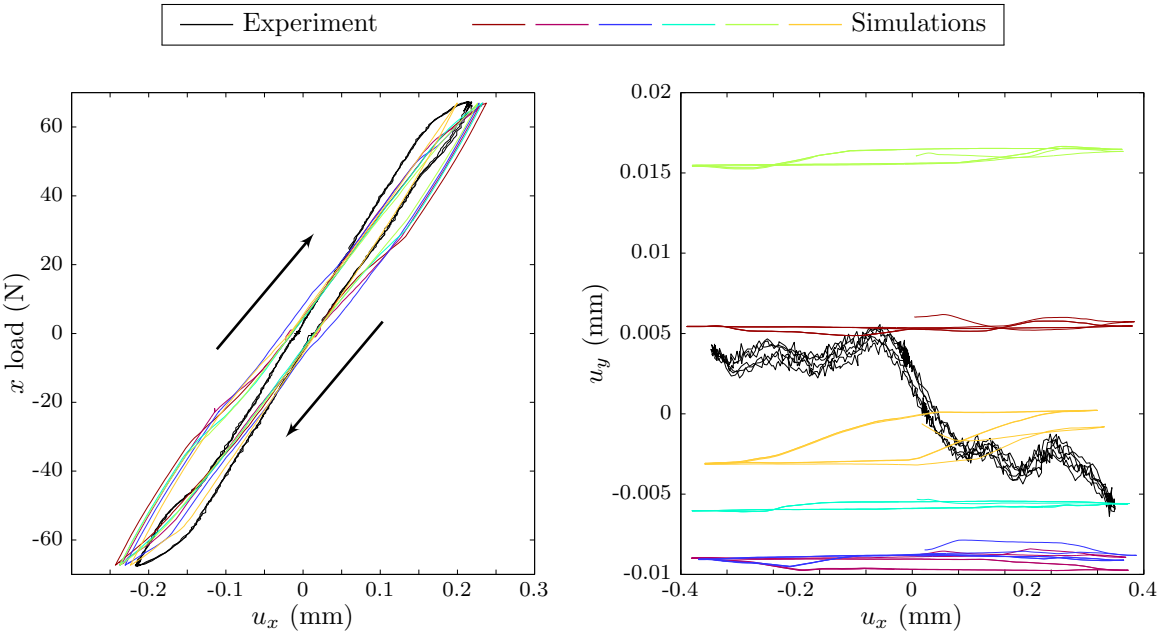

(a) (b)

Figure 7.6: Shear in the x direction with zero y load for six two-bay mast models with stochastic component behaviors. (Calibrated ball-end friction value.)

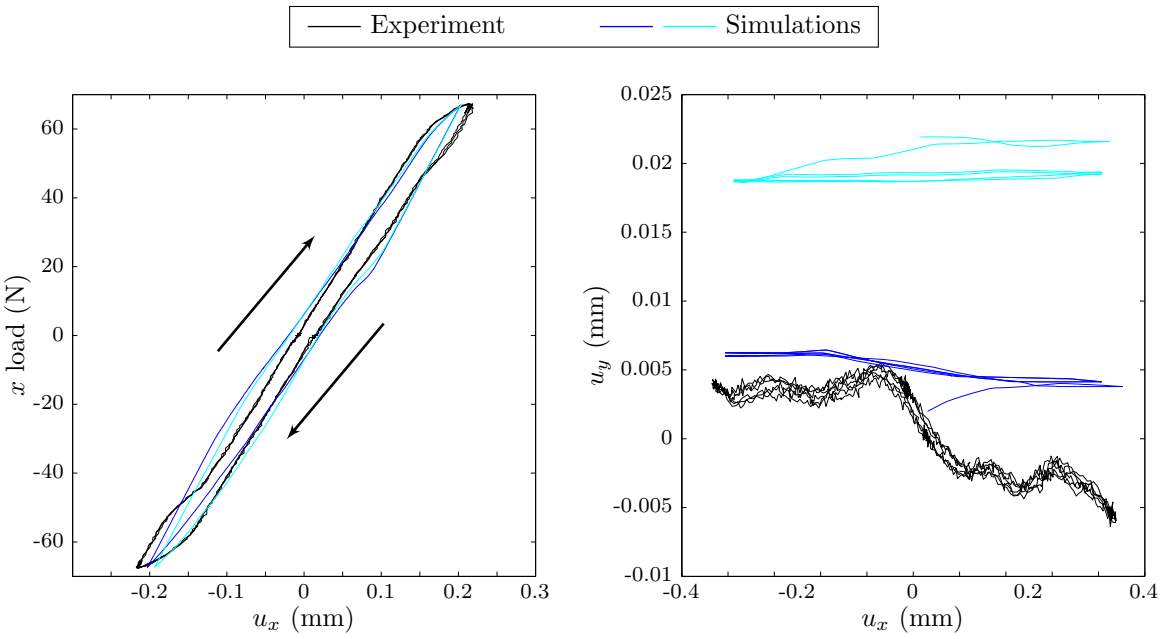

(a) (b)

Figure 7.7: Shear in the x direction with zero y load for six two-bay mast models with stochastic component behaviors. (Experimental ball-end friction value.)

The agreement between the simulations and experiment in Figures 7.6 and 7.7 is not exact, but the most important features, including the change in shape of the force-displacement curve due to latch effects, are captured. The path of the control node in the x-y plane, shown in Figure 7.7b, is not captured. It is possible that the very repeatable waviness seen in the experiment is an artifact of the surface finish of the joint faces measured by the lasers, or of some other systematic effect in the measurements.

When the modeling results for cases with simultaneous shear load are considered, the agreement with the complex behaviors seen experimentally is excellent. First, the comparison between Figures 7.8a and 7.8c shows an important effect. In the experiments, it was observed that while the response to loading in the x direction did not change between 0 and 53 N of load in the $-y$ direction, the force-displacement curve was clearly distorted at the 95 N load level. This is also seen in the simulation cases: the force-displacement curves at 95 N static load are wider and appear to include more latch disengagement than the curves from simulations with lower y loads. In the x-y paths, there is also a common behavior as the mast gradually settles into a new position over several cycles.

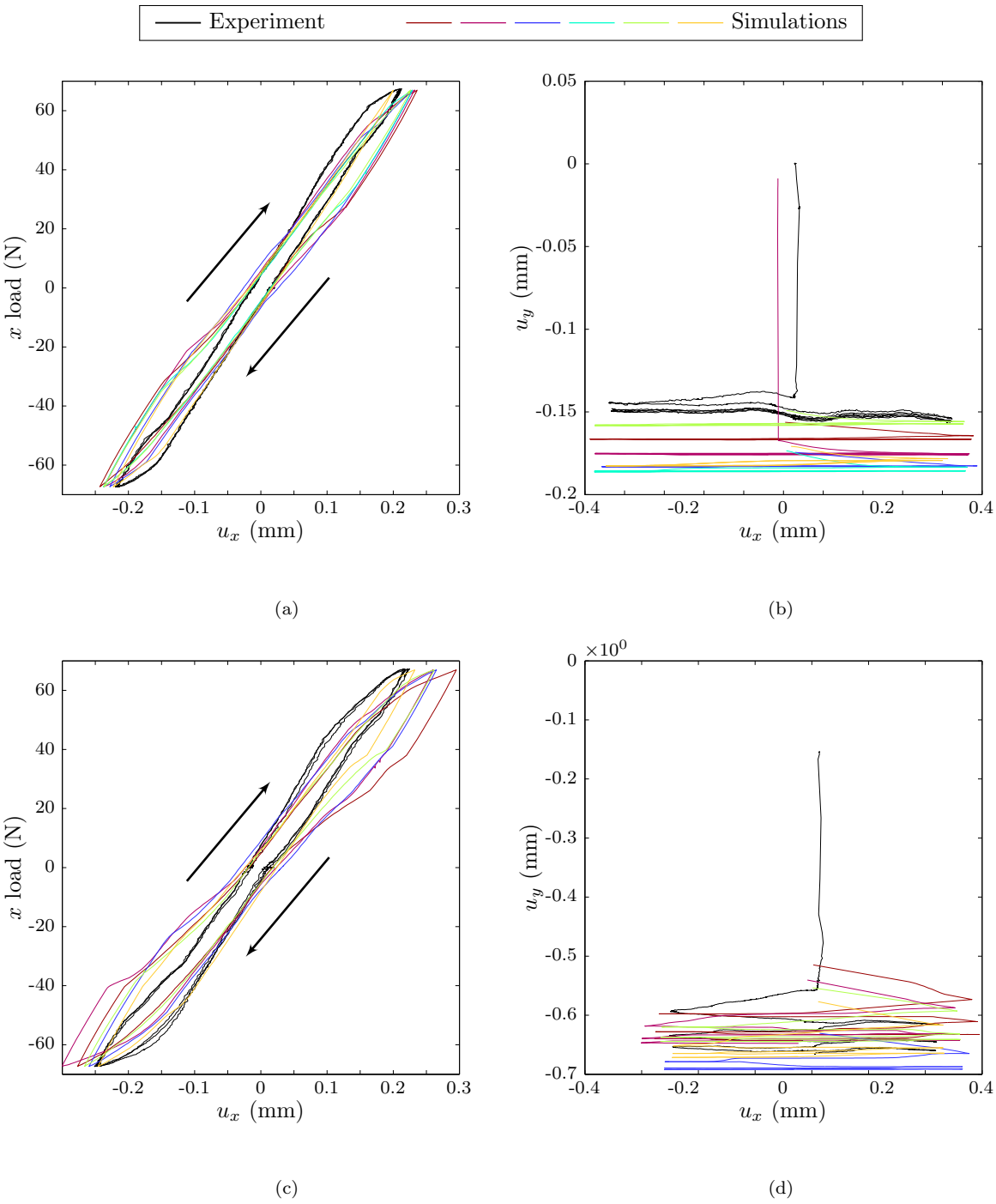

Figure 7.8: Shear in the x direction with simultaneous constant shear in the y direction for six two-bay mast models with stochastic component behaviors (calibrated ball-end friction). Figures 7.8a and 7.8b are for the case of $F_{-y} = 53$ N, and Figures 7.8c and 7.8d are for the case of $F_{-y} = 95$ N

.

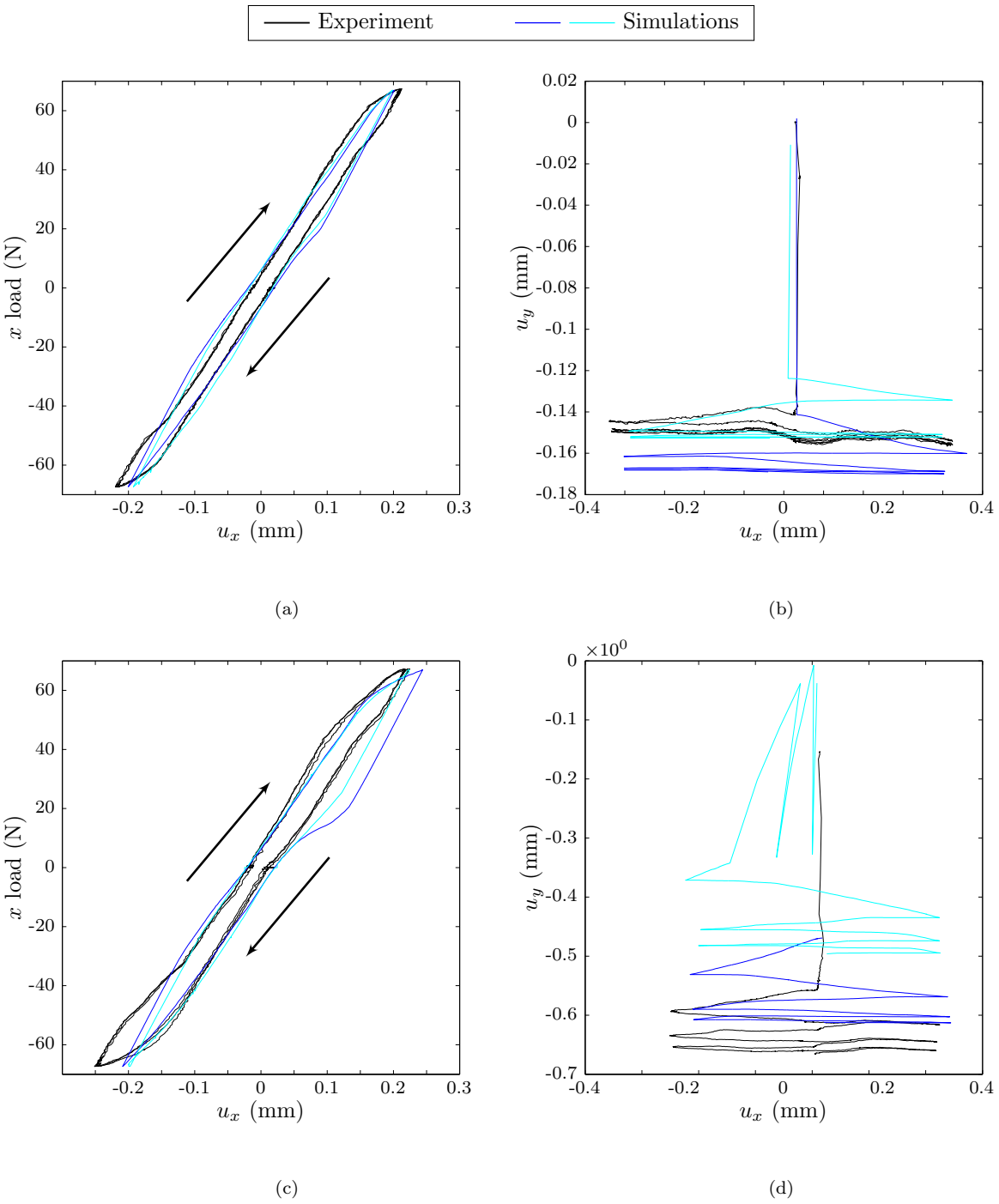

Figure 7.9: Shear in the x direction with simultaneous constant shear in the y direction for six two-bay mast models with stochastic component behaviors (experimental ball-end friction). Figures 7.9a and 7.9b are for the case of $F_{-y} = 53$ N, and Figures 7.9c and 7.9d are for the case of $F_{-y} = 95$ N

.

Chapter 8

Discussion

This thesis has presented a study of a jointed deployable mast of the ADAM design through experimentation and modeling. Results of the component and mast experiments are important and related measures of performance, and their relationships are made clearer through modeling. The mast behavior was primarily characterized by the range of resting positions of the unloaded mast after a transient quasi-static shear load. This measure describes the difference between the minimum and maximum x displacements of the mast tip when it is subjected to a shear load at x and released quasi-statically. A single measurement of this value of 21 μm on a two-bay mast was made experimentally, and simulations predicted a value of 36 ± 9 microns across a group of two-bay masts.

Component behavior experiments characterized the structural properties of several mast components. One key result is the wide spread in cable preloads seen on the test mast. Preload values ranged from 130 to 330 N over sixteen mast bays, with a mean tension of 220 N. This distribution was shown in Section 6.2.2 to produce little change in behavior from mast to mast; alone, the cable preload variability produced a standard deviation in range of resting positions of 2 μm from mast to mast in the case of shear loading of a two-bay mast. The mean value of the preload was also shown to have little impact on mast performance, barring slackened cables.

In contrast with the low impact of the mean value of cable preload on mast performance, the average value of the friction in the longeron ball-end joints showed a significant impact on the range of resting positions of a mast. Section 6.1.2 explored the impact of a simple joint friction metric, and Figure 8.1 shows the relationship between this metric μ and the range of resting positions in x for a two-bay mast undergoing 60 N of shear load.

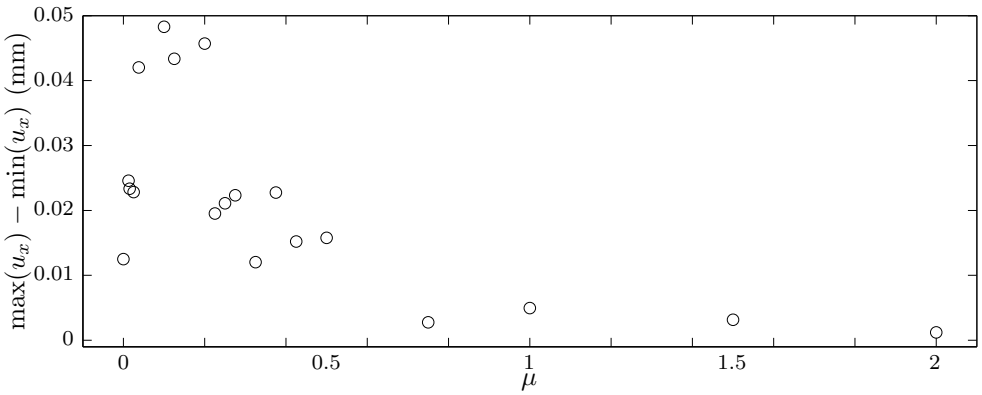

Figure 8.1: Relationship between mean ball-end joint friction coefficient μ and the range of resting positions.

The measurements and modeling of the latches revealed that they are the primary contributor to nonlinearity on this particular mast. Experimental characterization of the latches revealed that their behavior is hysteretic, and also that they demonstrate complex non-ideal behavior while latched. This deviation from idealized latch behavior was attributed to the imperfect seating of the latch bead against its backstop. The differences between a model with idealized latches and a model with experimentally based lookup tables were discussed in Section 6.2.4. One result was that hysteresis in the latches appeared to be responsible for about half of the range of resting positions, with the other half contributed by longeron joint friction. It is concluded that, if the budget for repeatability errors due to friction is of the order of tens of microns per bay, the longeron ball-end joints and the latching mechanisms both make important contributions to the range of positions that can be held by friction in mast interfaces. Modeling also revealed that, when the variability between latches was considered as the only source of variability between masts, it produced a standard deviation of 9 μm in the range of resting positions over a set of masts.

The latches also complicate the stiffness profile of the mast, especially at high loads, in a way that depends on the distribution of particular latches on the mast. A qualitative change in the force-displacement curve is observed where the latches begin to disengage, and its appearance is sensitive to the angle of a shear load relative to the mast sides, as discussed in Section 7.2. If high loads are to be applied during use of the mast, testing of these load cases should include a survey of multiple load orientations perpendicular to the axis of the mast.

In light of the sensitivity of the results, it may be advisable for high-precision missions to investigate the changes in behavior of frictional elements in the space environment. The longeron ball joints

of this study could be sensitive to vacuum or temperature, and their impact on the range of resting positions of the mast means that repeatability of the mast could be impacted by the environmental conditions of orbit.

Despite testing, friction in the longeron ball ends remained poorly characterized, and the value eventually calibrated to full-bay experiments was not in good agreement with the independently measured friction. In a setting where good predictive a priori data about the ball-end friction is very important, an applicable test would require the joint to be exercised in ways that resemble the actual joint motion (i.e., in bending rather than torsion). It would also be important to run the test under flight conditions, perhaps including low pressure, and again under ground testing conditions, so that the discrepancies between ground testing and flight performance might be anticipated.

There are additional experiments and modeling considerations that could contribute to the accuracy of this model. Beyond improvements to the treatment of longeron joint friction, material hysteresis and more directly measured materials properties are worth consideration. The cables did demonstrate hysteresis, as seen in Section 3.3.1. Standardized conditions of temperature, humidity, and joint cleanliness would also produce more reliable results, and would be necessary for a prediction of the change in behavior between ground testing and orbit. The relevance of part variability could be assessed in further detail in a much large study, with statistically significant data collection from tens of nominally identical parts. The most definitively variable property of the sample mast was cable preload, whose distribution was shown to have at most a modest impact on the mast behavior.

It is possible to improve the latch characterization further through improvements to the experimental design, but relating latch behavior to temperature might be a more significant experimental contribution. Unanticipated interference of tightly toleranced parts appears to have caused the damping subsystem failure in SRTM [49], and the latches could react differently at different temperatures for a variety of reasons. Because of the demonstrated significance of the latch behavior in overall mast hysteresis, any mast that requires extreme repeatability in the space environment should have its latching system performance evaluate for temperature dependent behavior.

The same modeling system used to produce results for a two-bay mast can model masts of arbitrary length. Figure 8.2 shows a comparison between a number of simulations of two-masts masts under 60 N shear and a simulation of a twelve-bay mast with the same part properties and distributions under the same tip load. The twelve-bay mast shows a similar residual displacement per bay, and a reduced impact from the variability of latch behaviors, as the effects of more individual

components are combined in the response of a longer mast.

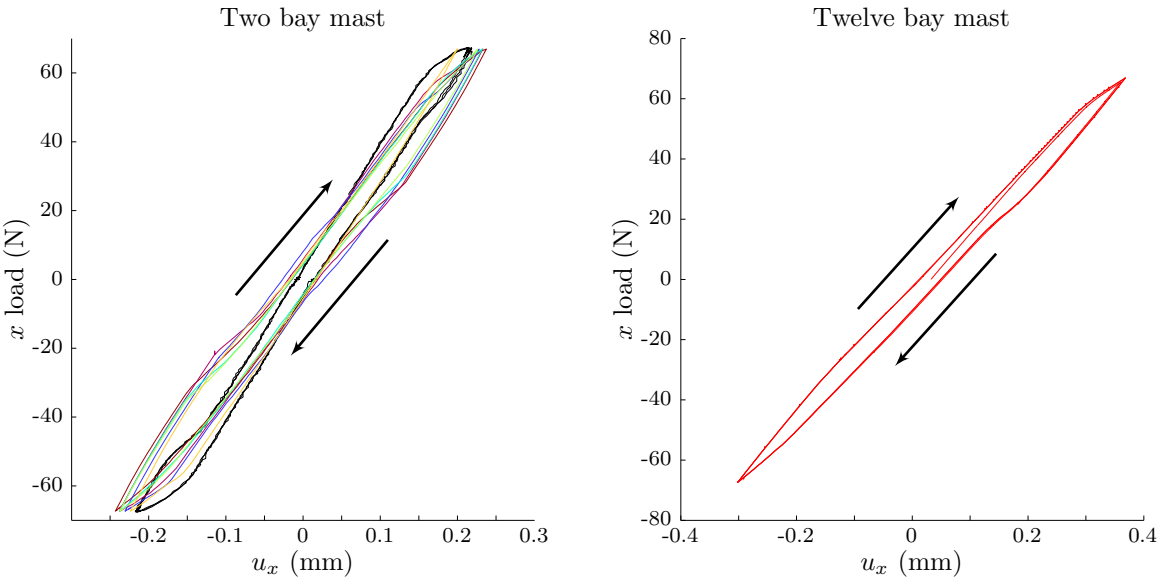

(a) (b)

Figure 8.2: The response curves of two- and twelve-bay masts under the same tip shear load.

The computational expense of initializing a mast with part variability and preload is worth balancing with the impact of these effects. It took approximately two minutes to run the initialization and stabilization steps of Section 5.3.2 for a two-bay mast with no randomized properties; it took an average of twenty minutes to initialize the same mast with all the randomized properties, and each individual randomized property had a substantial effect on this time. After the initialization steps, simulation times are not strongly impacted by the variability in properties. This sort of time scale is often not a problem for short masts, but increases exponentially with the number of bays: a four-bay mast took two hours to initialize and a twelve-bay mast, twenty hours.

A few different approaches are possible to improve this behavior. Of course, a different solution engine could be used. Abaqus/Standard may not be the ideal finite element method solver for a structure with so many frictional elements. Within the bounds of conventional finite element software, though, the user element for the latch could be greatly improved. Within the scope of the project, streamlining the latch subroutine was not a priority, and it is consequently dense with conditional statements and unnecessary memory allocation. A more general treatment of the lookup tables should be possible, with improved tolerance for nonmonotonic lookup tables. The treatment of the zones of bead behavior in particular would benefit from a more general approach, rather than hard-coding the particular zones of the ADAM mast latches. A standard approach to this system

of cable system problem would be a valuable addition to the Abaqus element ad example libraries, or to any other finite element system.

In conclusion, this thesis has characterized and modeled a typical joint-dominated deployable mast design, and found that the locking mechanism and the joints that permit the mast to be folded contribute to the behavior of the deployed mast. The friction in these two parts allows each bay to maintain a misalignment between its top and bottom faces of approximately 10 μm in lateral displacement. This is an acceptable repeatability for current mast projects, and will hopefully improve alongside the other elements of space observatory design.

Appendix A

Calculating the position of a rigid body from rangefinding lasers

This describes the implementation of a simple algorithm that calculates the six degrees of freedom of the motion of a rigid body. The input data comes from rangefinding lasers.

We shall make a number of simplifying assumptions to develop the equations of this method:

- The laser is aimed at a planar face
- There is some known initial position of the face that corresponds to the zero reading of the laser

Consider a face in its initial position. The face is defined by a point $\mathbf{p}_0$ and a normal direction $\hat{\mathbf{n}}_0$. The point that is measured by the laser in this initial position is located at $\mathbf{l}$, and the direction of the laser beam measurement is $\hat{\mathbf{x}}$.

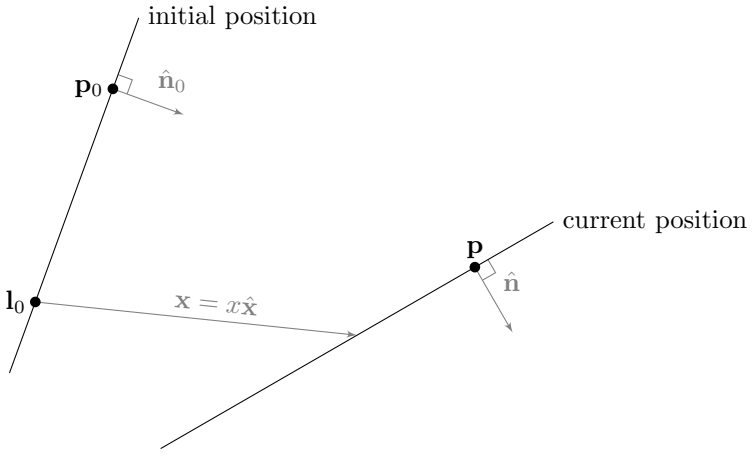

Figure A.1: The variables of the problem.

The face then moves by a rotation of magnitude θ about a direction $\hat{\mathbf{r}}$ and a displacement $\mathbf{d}$. The

rotational transformation can be expressed with the rotation matrix $\mathbf{R}$. After this motion, the laser reads a value x, which is the position of the laser dot along the vector $\hat{\mathbf{x}}$. We will define the laser vector $\mathbf{x} = x\hat{\mathbf{x}}$, where $\hat{\mathbf{x}}$ is a known parameter of the experimental setup and x is data gathered from the laser during the experiment (possibly rezeroed so that there is an appropriate initial position).

The equation that expressed the relationship between this displacement and the laser readout is:

$$\mathbf{p} = \mathbf{R}\mathbf{p}_0 + \mathbf{d} \tag{A.1}$$

$$\hat{\mathbf{n}} = \mathbf{R}\hat{\mathbf{n}}_0 \tag{A.2}$$

$$\mathbf{x} \cdot \hat{\mathbf{n}} = (\mathbf{p} - \mathbf{l}_0) \cdot \hat{\mathbf{n}} \tag{A.3}$$

$$\therefore x - \frac{(\mathbf{p} - \mathbf{l}_0) \cdot \hat{\mathbf{n}}}{\hat{\mathbf{x}} \cdot \hat{\mathbf{n}}} = 0 \tag{A.4}$$

in these equations, x is the output of the laser, $\hat{\mathbf{n}}_0, \hat{\mathbf{p}}_0$, and $\hat{\mathbf{l}}_0$ are parameters of the experimental setup, and $\mathbf{d}$ and $\mathbf{R}$ are the desired displacement and rotation, each of which have three independent elements.

Further, there are a number of assumptions and requirements for this particular Matlab code:

- The lasers are all measuring a single rigid body, so that all faces move simultaneously
- There are exactly six lasers
- The lasers are arranged such that all six degrees of freedom can be detected (they are not, for example, all aimed at the same face)

The following code may be applied to a vector of the six laser readouts `x`, with the laser setup defined in a Matlab `struct` called `lasersetup` via the command `solutionn = fsolve(@sixDOF, [0,0,0,0,0,0], lasersetup, x)`. The initial guess in this command was defined as $\mathbf{R} = \mathbf{I}, \mathbf{d} = [0, 0, 0]$.

```
function sixDOF = sixDOF(posrot, lasersetup, x)

d = posrot(1:3);
% theta will be defined as always positive
theta = sqrt(sum(posrot(4:6).^2));
if theta < 1e-16
    rot_dir = [0,0,1];
else
    rot_dir = posrot(4:6) / theta;
end

R = rotmat(rot_dir, theta);

for i = 1:6
```

```
    p = d + (R*lasersetup.p0(i,:)')';
    x_unit = lasersetup.x_unit(i,:);
    x_unit = x_unit/sqrt(sum(x_unit.^2));
    n_unit = (R*lasersetup.n0(i,:)')';
    n_unit = n_unit/sqrt(sum(n_unit.^2));
    l = lasersetup.l_pos(i,:);

    sixDOF(i) = x(i) - sum((p-l).*n_unit)/sum(x_unit.*n_unit);

end
```

This code calls a subroutine `rotmat`, which transforms an axis and angle into a rotation matrix.

Appendix B

Mast generation code (Matlab)

B.1 Mast generation pseudocode

1. Call `bay_properties(num_bays, randomness)` to generate bay properties.
2. Initialize first corner at $(0, 0, 0)$. Initialize counters to zero.
3. For bay $b = 1, 2, ..., B$, where B is the total number of bays,
   (a) For side $s = 1, 2, 3, 4$,
      i. Place the nodes that are attached to the bottom-left joint:
         - The left node of the lower batten
         - The bottom-left cable attachment
         - The lower node of the left longeron
      ii. Place the nodes that are attached to the bottom-right joint:
         - The bottom-right cable attachment
         - The right node of the lower batten
      iii. Place the nodes that are attached to the top-right joint:
         - The top-right cable attachment
      iv. Place the nodes that are attached to the top-left joint:
         - The upper node of the left longeron
         - The top-left cable attachment
      v. Place the nodes that are attached to the latch/pulley assembly:
         - The ends of the two simples cables (C and D)
         - The intersection point of the two sections of cable A-B
4. Write nodes for the top batten square and dummy nodes for the user elements.
5. If subdividing each longeron and batten into multiple elements, create these nodes
6. Open Abaqus `.inp` file for writing.
7. `*NODE` Write all node positions
8. Write the rigid bodies that represent the batten corner joints and the latch/pulley assemblies.
9. Write batten elements.
10. Write longeron elements.
11. Write the elements for cables C and D.

12. Write the elements for cable A-B and the latch.
13. Close `.inp` file.

Appendix C

Fortran UEL code

This is the complete user subroutine Fortran code. The later sections of code are generated by Matlab, as marked on page 137.

The code begins with the UEL subroutine header, as described in [43, p.].

```
      SUBROUTINE UEL(RHS,AMATRX,SVARS,ENERGY,NDOFEL,NRHS,NSVARS,
     1     PROPS,NPROPS,COORDS,MCRD,NNODE,U,DU,V,A,JTYPE,TIME,DTIME,
     2     KSTEP,KINC,JELEM,PARAMS,NDLOAD,JDLTYP,ADLMAG,PREDEF,
     3     NPREDF,LFLAGS,MLVARX,DDLMAG,MDLOAD,PNEWDT,JPROPS,NJPROP,
     4     PERIOD)
C
      implicit NONE
      INTEGER NDOFEL, NRHS, NSVARS, NPROPS, MCRD, NNODE, JTYPE
      INTEGER KSTEP, KINC, JELEM, NDLOAD, JDLTYP, NPREDF, LFLAGS
      INTEGER MLVARX, MDLOAD, JPROPS, NJPROP
      INTEGER NPRECD
      INTEGER INDX
      INTEGER K1, KRHS, K2
      INTEGER PROPNUM, NPROPNUM
      REAL*8 SVARS, PROPS, TIME, DTIME, ADLMAG
      REAL*8 PREDEF, DDLMAG, PNEWDT, PERIOD
      REAL*8 AREA, E, RADIUS, FMAX, LB, EA
      REAL*8 PARAMS
      REAL*8 ZERO, HALF, ONE, TWO, TEN, THREE, FOUR, FIVE, SIX
      REAL*8 P1, P2, P3, V1 , V2, X0, PASSPARAMS
      REAL*8 L0, L1, L2, LW
      REAL*8 COORDS, U, DU, V, A
      REAL*8 AMATRX, SRESID, ENERGY, RHS
      REAL*8 T1, T2, L10, Lw0, L20
      REAL*8 V1LENGTH, V2LENGTH
      REAL*8 LATCHED
      REAL*8 N(3)
      REAL*8 L, T
      REAL*8 DL1, DL2, LATCHING, BEADZONE
      REAL*8 CYLRADIUS, LATCHK, LATCHH, LATCHMU, LATXVERT, DELTA
      REAL*8 LATCHXHORIZ, STUCKT1, STUCKT2, STUCKDT
      REAL*8 LATCHXVERT, XLOOKUP
      REAL*8 STUCK, EX, NEWRUN, XOLD
      REAL*8 DELTRH, STUCKDTMAX, STUCKDTMIN
      REAL*8 TINY, FEWNEWTONS
```

```
      REAL*8 F, MINDT, MAXDT, DFDT1, DFDT2, DFDL10, DFDL20
      REAL*8 X12, X23, X45, X56, LATCHLB, CABLEEA, LZERO
      REAL SR1, SR2
      DOUBLE PRECISION SDP1, SDP2

      PARAMETER (NPRECD=2)
      PARAMETER ( ZERO = 0.D0, HALF = 0.5D0, ONE = 1.D0)
      PARAMETER ( TWO=2.0D0, TEN=10.0D0, THREE=3.0D0 )
      PARAMETER ( FOUR=4.0D0, FIVE=5.0D0, SIX=6.0D0 )
      PARAMETER ( TINY=1.0D-10, FEWNEWTONS=1.0D-8 )

      DIMENSION RHS(MLVARX,*),AMATRX(NDOFEL,NDOFEL),
     1     SVARS(NSVARS),ENERGY(8),PROPS(NPROPS),COORDS(MCRD,NNODE),
     2     U(NDOFEL),DU(MLVARX,*),V(NDOFEL),A(NDOFEL),TIME(2),
     3     PARAMS(3),JDLTYP(MDLOAD,*),ADLMAG(MDLOAD,*),
     4     DDLMAG(MDLOAD,*),PREDEF(2,NPREDF,NNODE),LFLAGS(*),
     5     JPROPS(*)
      DIMENSION SRESID(NDOFEL)
      DIMENSION P1(3), P2(3), P3(3)
      DIMENSION V1(3), V2(3)
      DIMENSION INDX(3)
      DIMENSION X0(4),  PASSPARAMS(7)
```

Element type three is the three-node UEL for the latch and cable A-B.

The variable `SVARS` contains the state variables. These will be updated and stored after the solution is found for the new values, but right now it is necessary to establish the last calculated values of `T1`=T_A, `T2`=T_B, `L10`=L_A^0, and `L20`=L_B^0.

```
      IF (JTYPE.EQ.3) THEN
         T1=SVARS(1)
         T2=SVARS(2)
         L10=SVARS(3)
         L20=SVARS(4)
         LATCHING=SVARS(5)
         BEADZONE=SVARS(6)
```

The variable `PROPNUM` defines which set of properties to use for this latch. In previous version, the properties were specified in the `.inp` file and passed to the subroutine in the standard way, as parameters like the Poisson's ratio as normally passed to elements. This became impractical as the number of properties describing the behavior became large and lookup tables were added.

```
         PROPNUM=JPROPS(1)
```

The following code identifies whether this is the first run of the subroutine, which would mean that the state variables `SVARS` did not contain a solution of the system.

```
         NEWRUN=-ONE
         IF ((LATCHING.NE.ONE).AND.(LATCHING.NE.(-ONE))) THEN
            LATCHING=-ONE
            NEWRUN=ONE
         END IF
         IF (BEADZONE.EQ.ZERO) THEN
            BEADZONE=ONE
         END IF
```

Next, the absolute end positions of the nodes are found through their initial positions in COORDS and their displacements in U. Depending on the absolute displacement does sacrifice some decimals of precision that might be available if all calculations were made based on the displacements.

```
EA=CABLEEA(PROPNUM)
P1(1) = COORDS(1,1) +U(1)
P1(2) = COORDS(2,1) +U(2)
P1(3) = COORDS(3,1) +U(3)
P2(1) = COORDS(1,2) +U(4)
P2(2) = COORDS(2,2) +U(5)
P2(3) = COORDS(3,2) +U(6)
P3(1) = COORDS(1,3) +U(7)
P3(2) = COORDS(2,3) +U(8)
P3(3) = COORDS(3,3) +U(9)
```

The total un-stretched cable length L0=L^0 is controlled by a combination of the initial length and an adjustment provided by the control node in the degree of freedom NDOFEL.

```
      L0=SQRT((COORDS(1,3)-COORDS(1,2))**2
     *       +(COORDS(2,3)-COORDS(2,2))**2
     *       +(COORDS(3,3)-COORDS(3,2))**2)
     *       +SQRT((COORDS(1,1)-COORDS(1,2))**2
     *       +(COORDS(2,1)-COORDS(2,2))**2
     *       +(COORDS(3,1)-COORDS(3,2))**2)
      L0=L0-U(NDOFEL)
```

The bead attachment position LB=L_b is similarly defined by the propertyLATCHLB(PROPNUM) and the degree of freedom NDOFEL-1.

```
LB=LATCHLB(PROPNUM)-U(NDOFEL-1)
```

The following code makes it possible for bead "sticking" to be evaluated properly when the cable lengths have been adjusted in the most recent step. "Sticking" occurs when the bead does not change position in this step, and is assumed to occur if the current distribution of cable on the two sides of the latch will produce a tension differential between the minimum and maximum possible at this bead location x.

```
IF ((DU(NDOFEL,1).NE.ZERO).OR.(DU(NDOFEL-1,1).NE.ZERO)) THEN
   L20 = L20 - (DU(NDOFEL, 1)-DU(NDOFEL-1, 1))
END IF
IF (DU(NDOFEL-1, 1).NE.ZERO) THEN
   L10 = L10 - DU(NDOFEL-1, 1)
END IF
IF (XLOOKUP(PROPNUM).LT.LATCHXVERT(PROPNUM)) THEN
 IF ((LB-L10).LT.LATCHXVERT(PROPNUM)) THEN
    PRINT *, "Unacceptable X; resetting to LVERT="
    PRINT *, LB-L10,LATCHXVERT(PROPNUM)
  SVARS(3)=LB-LATCHXVERT(PROPNUM)
  L10 = LB-LATCHXVERT(PROPNUM)
  L20 = L0 - L10
 END IF
END IF
```

The stretched lengths L1= L_A and L2= L_B are found from the current node positions.

```
      V1(1) = P1(1) - P2(1)
      V1(2) = P1(2) - P2(2)
      V1(3) = P1(3) - P2(3)
      V2(1) = P3(1) - P2(1)
      V2(2) = P3(2) - P2(2)
      V2(3) = P3(3) - P2(3)
      L1=SQRT((V1(1))**TWO+(V1(2))**TWO+(V1(3))**TWO)
      L2=SQRT((V2(1))**TWO+(V2(2))**TWO+(V2(3))**TWO)
      V1 = V1/L1
      V2 = V2/L2
```

The incremental changes of node positions `DU` are used to identify the direction of motion of the bead, which will be stored in `LATCHING`.

```
      DL1 = V1(1)*(DU(1,1)-DU(4,1)) + V1(2)*(DU(2,1)-DU(5,1))
     *        + V1(3)*(DU(3,1)-DU(6,1))
      DL2 = V2(1)*(DU(7,1)-DU(4,1)) + V2(2)*(DU(8,1)-DU(5,1))
     *        + V2(3)*(DU(9,1)-DU(6,1))
      IF (NEWRUN.NE.ONE) THEN
         IF (DL1.GT.DL2) THEN
            LATCHING=ONE
         ELSE IF (DL1.LT.DL2) THEN
            LATCHING=-ONE
         END IF
      END IF
```

`PASSPARAMS` holds the variables of the problem that will be used to solve for the tensions and other relevant values. Once we have those, we can query the subroutine `LATCHHANDLER` to find the minimum and maximum possible tension differentials at this location.

```
      PASSPARAMS(1)=LATCHING
      PASSPARAMS(2)=BEADZONE
      PASSPARAMS(4)=L1
      PASSPARAMS(5)=L2
      PASSPARAMS(6)=L0
      PASSPARAMS(7)=LB
      CALL LATCHHANDLER(T1, T2, L10, L20, PASSPARAMS,
     *        F, MINDT, MAXDT, DFDT1, DFDT2, DFDL10, DFDL20,
     *        PROPNUM, NPROPNUM)
      STUCK=-ONE
      IF (NEWRUN.LT.ZERO) THEN
         STUCKT1 = EA*(L1-L10)/L10
         STUCKT2 = EA*(L2-L20)/L20
         IF (STUCKT1.LT.ZERO) STUCKT1=ZERO
         IF (STUCKT2.LT.ZERO) STUCKT2=ZERO
         STUCKDT=STUCKT2-STUCKT1
   EX=LB-L10
   IF (EX.GT.LATCHXHORIZ(PROPNUM)) THEN
C     Then do nothing- it can't be stuck on the pulley
C     (pending further code development)
   ELSE
             IF (STUCKDT.GT.(MINDT-FEWNEWTONS)) THEN
                IF (STUCKDT.LT.(MAXDT+FEWNEWTONS)) THEN
```

```
                  STUCK=ONE
                  IF (DL1.NE.ZERO) STUCK=TWO
               END IF
            END IF
   END IF
         END IF
         PASSPARAMS(3)=STUCK
```

The variable `X0` will hold the four unknowns of the problem: T_A, T_B, L_A^0 and L_B^0. If this is a new run, guesses are used to initialize the variables.

```
         X0(1)=ZERO
         X0(2)=ZERO
         IF (XLOOKUP(PROPNUM).LT.LATCHXVERT(PROPNUM)) THEN
            X0(3)=LB-LATCHXVERT(PROPNUM)
         ELSE
            X0(3)=LB-(X56(PROPNUM)-0.00001)
         END IF
         X0(4)=L0-X0(3)
         X0(3)=L0*L1/(L1+L2)
         X0(4)=L0*L2/(L1+L2)
C     If this is a continuation from a previous solution, start from
C     those state variables.
         IF (NEWRUN.LT.ZERO) THEN
            X0=SVARS(1:4)
            IF (STUCK.GT.ZERO) THEN
               X0(1) = STUCKT1
               X0(2) = STUCKT2
               X0(3) = L10
               X0(4) = L20
            END IF
         ELSE
            PRINT *, "FIRST RUN"
         END IF
```

The bead zones are defined in Section 5.2.2.1 and divide the latch into it locally monotonic behaviors. If the bead is already known to be stuck, this is a simple definition.

```
         IF (STUCK.GT.ZERO) THEN
            X0(1) = STUCKT1
            X0(2) = STUCKT2
            IF (LATCHING.GT.ZERO) THEN
               IF ((LB-X0(3)).GT.X45(PROPNUM)) THEN
                  BEADZONE=FOUR
               ELSE IF ((LB-X0(3)).GT.X56(PROPNUM)) THEN
                  BEADZONE=FIVE
               ELSE
                  BEADZONE=SIX
               END IF
            ELSE
               IF ((LB-X0(3)).GT.X23(PROPNUM)) THEN
                  BEADZONE=THREE
               ELSE IF ((LB-X0(3)).GT.X12(PROPNUM)) THEN
                  BEADZONE=TWO
               ELSE
```

```
            BEADZONE=ONE
         END IF
      END IF
```

If the bead is not stuck at its position, and moving in the latch, we start at the current bead zone and move to the next one in this direction of motion if a valid solution is not found.

```
      ELSE

         IF ((XLOOKUP(PROPNUM).LT.LATCHXVERT(PROPNUM)).
     *        AND.((LB-X0(3)).LT.LATCHXVERT(PROPNUM))) THEN
            X0(3) = LB-LATCHXVERT(PROPNUM)
            X0(4) = L0-X0(3)
         END IF
         IF (LATCHING.GT.ZERO) THEN
            IF ((LB-X0(3)).GT.X45(PROPNUM)) THEN
               BEADZONE=FOUR
            ELSE IF ((LB-X0(3)).GT.X56(PROPNUM)) THEN
               BEADZONE=FIVE
            ELSE
               BEADZONE=SIX
            END IF
            PASSPARAMS(1)=LATCHING
            PASSPARAMS(2)=BEADZONE
            PASSPARAMS(3)=STUCK

            IF (BEADZONE.EQ.SIX) THEN
               CALL MNEWT(X0, PASSPARAMS, PROPNUM)
            ELSE IF (BEADZONE.EQ.FIVE) THEN
               CALL MNEWT(X0, PASSPARAMS, PROPNUM)
               IF ((LB-X0(3)).LT.X56(PROPNUM)) THEN
                  BEADZONE=SIX
                  PRINT *, "BEADZONE SWITCHED FROM 5 TO ", BEADZONE
                  PASSPARAMS(2)=BEADZONE
                  CALL MNEWT(X0, PASSPARAMS, PROPNUM)
               END IF
            ELSE
               CALL MNEWT(X0, PASSPARAMS, PROPNUM)
               IF ((LB-X0(3)).LT.X45(PROPNUM)) THEN
                  BEADZONE=FIVE
                  PRINT *, "BEADZONE SWITCHED FROM 4 TO ", BEADZONE
                  PASSPARAMS(2)=BEADZONE
                  CALL MNEWT(X0, PASSPARAMS, PROPNUM)
                  IF ((LB-X0(3)).LT.X56(PROPNUM)) THEN
                     BEADZONE=SIX
                     PRINT *, "BEADZONE SWITCHED FROM 4 TO 5 TO "
     *                    , BEADZONE
                     PASSPARAMS(2)=BEADZONE
                     CALL MNEWT(X0, PASSPARAMS, PROPNUM)
                  END IF
               END IF
            END IF

         END IF
```

```
      IF (LATCHING.LE.ZERO) THEN
         IF ((LB-X0(3)).GT.X23(PROPNUM)) THEN
            BEADZONE=THREE
         ELSE IF ((LB-X0(3)).GT.X12(PROPNUM)) THEN
            BEADZONE=TWO
         ELSE
            BEADZONE=ONE
         END IF
         PASSPARAMS(2)=BEADZONE

         IF (BEADZONE.EQ.THREE) THEN
            CALL MNEWT(X0, PASSPARAMS, PROPNUM)
         ELSE IF (BEADZONE.EQ.TWO) THEN
            CALL MNEWT(X0, PASSPARAMS, PROPNUM)
            IF ((LB-X0(3)).GT.X23(PROPNUM)) THEN
               BEADZONE=THREE
               PRINT *, "BEADZONE SWITCHED FROM 2 TO ", BEADZONE
               PASSPARAMS(2)=BEADZONE
               CALL MNEWT(X0, PASSPARAMS, PROPNUM)
            END IF
         ELSE
            CALL MNEWT(X0, PASSPARAMS, PROPNUM)
            IF ((LB-X0(3)).GT.X12(PROPNUM)) THEN
               BEADZONE=TWO
               PRINT *, "BEADZONE SWITCHED FROM 1 TO ", BEADZONE
               PASSPARAMS(2)=BEADZONE
               CALL MNEWT(X0, PASSPARAMS, PROPNUM)
               IF ((LB-X0(3)).GT.X23(PROPNUM)) THEN
                  BEADZONE=THREE
                  PRINT *, "BEADZONE SWITCHED FROM 1 TO 2 TO "
     *                 , BEADZONE
                  PASSPARAMS(2)=BEADZONE
                  CALL MNEWT(X0, PASSPARAMS, PROPNUM)
               END IF
            END IF
         END IF
      END IF
```

At this point, there is a complete solution for the current state of the latch and cable. The state variables can be updated and the subroutine calculates the reaction forces for return to Abaqus.

```
      T1=X0(1)
      T2=X0(2)
      L10=X0(3)
      L20=X0(4)
      SVARS(1)=T1
      SVARS(2)=T2
      SVARS(3)=L10
      SVARS(4)=L20
      SVARS(5)=LATCHING
      SVARS(6)=BEADZONE
```

```
C     Clear RHS, AMATRX, and SRESID so that unspecified columns will
C     definitely be zero.
         DO K1 = 1, NDOFEL
            SRESID(K1) = ZERO
            DO KRHS = 1, NRHS
               RHS(K1,KRHS) = ZERO
            END DO
            DO K2 = 1, NDOFEL
               AMATRX(K2,K1) = ZERO
            END DO
         END DO
         DO K1 = 1, MLVARX
            DO KRHS = 1, NRHS
               RHS(K1,KRHS) = ZERO
            END DO
         END DO
```

The state variables are recorded as reaction forces on the dummy nodes so they can be usefully retrieved.

```
         DO K1 = 1, 8
            RHS(9+K1,1)=-SVARS(K1)
         END DO
         RHS(9+7,1)=-(L2)
         RHS(9+8,1)=-(LB-SVARS(3))
         RHS(9+9,1)=-STUCK
```

The next step is to confirm that the values in `LFLAGS` are requesting a solution for the only type of problem this user element is valid for: static or quasi-static simulations. The subroutine `STIFFNESS` (page 133) is called to produce the stiffness matrix.

```
         IF (LFLAGS(3).EQ.1) THEN
            IF (LFLAGS(1).EQ.1 .OR. LFLAGS(1).EQ.2) THEN
               CALL STIFFNESS(AMATRX, NDOFEL, V1, L1, V2,
     *              L2,  X0, PASSPARAMS, PROPNUM)
               IF (LFLAGS(4).EQ.0) THEN
C     The reaction force is the magnitude of the tension in the
C     direction of the cable.
                  SRESID(1) = T1*V1(1)
                  SRESID(2) = T1*V1(2)
                  SRESID(3) = T1*V1(3)
                  SRESID(7) = T2*V2(1)
                  SRESID(8) = T2*V2(2)
                  SRESID(9) = T2*V2(3)
                  SRESID(4) = -(SRESID(1)+SRESID(7))
                  SRESID(5) = -(SRESID(2)+SRESID(8))
                  SRESID(6) = -(SRESID(3)+SRESID(9))
C     There is no special reason to subtract SRESID from zero rather
C     than simply assigning it; this only follows the convention of
C     the Abaqus manual example.
                  RHS(1,1) = RHS(1,1)-SRESID(1)
                  RHS(2,1) = RHS(2,1)-SRESID(2)
                  RHS(3,1) = RHS(3,1)-SRESID(3)
                  RHS(4,1) = RHS(4,1)-SRESID(4)
                  RHS(5,1) = RHS(5,1)-SRESID(5)
```

```
            RHS(6,1) = RHS(6,1)-SRESID(6)
            RHS(7,1) = RHS(7,1)-SRESID(7)
            RHS(8,1) = RHS(8,1)-SRESID(8)
            RHS(9,1) = RHS(9,1)-SRESID(9)
         ELSE
            PRINT *,"ERROR: DID NOT ENTER 3RD IF"
         END IF
      ELSE
         PRINT *,"ERROR: DID NOT ENTER 2ND IF"
      END IF
   ELSE
      PRINT *,"ERROR: DID NOT ENTER 1ST IF"
   END IF
END IF
```

If JTYPE is two, the subroutine for cable C or D is being called. This is a much simpler element.

```
IF (JTYPE.EQ.2) THEN
   E=PROPS(1)
   AREA=PROPS(2)
   IF (NNODE.EQ.2) THEN
      L0=PROPS(3)
   ELSE
      L0=SQRT((COORDS(1,1)-COORDS(1,2))**2
*           + (COORDS(2,1)-COORDS(2,2))**2
*           + (COORDS(3,1)-COORDS(3,2))**2)
      L0=L0-U(7)
   END IF
   P1(1) = COORDS(1,1)+U(1)
   P1(2) = COORDS(2,1)+U(2)
   P1(3) = COORDS(3,1)+U(3)
   P2(1) = COORDS(1,2)+U(4)
   P2(2) = COORDS(2,2)+U(5)
   P2(3) = COORDS(3,2)+U(6)
   L=SQRT((P1(1)-P2(1))**2+(P1(2)-P2(2))**2+(P1(3)-P2(3))**2)
   N(1)=(P1(1)-P2(1))/L
   N(2)=(P1(2)-P2(2))/L
   N(3)=(P1(3)-P2(3))/L
   IF (L.GE.L0) THEN
      T=E*AREA*(L-L0)/L0
   ELSE
      T=ZERO
   END IF
   RHS(1,1) = -T*N(1)
   RHS(2,1) = -T*N(2)
   RHS(3,1) = -T*N(3)
   RHS(4,1) = -RHS(1,1)
   RHS(5,1) = -RHS(2,1)
   RHS(6,1) = -RHS(3,1)
   IF (L.GE.L0) THEN
      DO K1 = 1, 3
         DO K2 = 1, 3
            IF (K1.EQ.K2) THEN
               AMATRX(K1,K2)
```

```
*                    = ((T*(ONE-N(K1)**2)/L+N(K1)*E*AREA*N(K2)/LO))
              ELSE
                 AMATRX(K1,K2)
*                    = ((T*(-N(K1)*N(K2))/L+N(K1)*E*AREA*N(K2)/LO))
              END IF
              AMATRX(K1+3,K2) = -AMATRX(K1, K2)
              AMATRX(K1, K2+3) = -AMATRX(K1, K2)
              AMATRX(K1+3, K2+3) = AMATRX(K1, K2)
           END DO
        END DO
     ELSE
        AMATRX = ZERO*AMATRX
     END IF
  END IF
  RETURN
  END
```

The subroutines for LU decomposition, `LUDCMP` and `LUBKSB`, are taken verbatim from Press et al. [40] and omitted here.

```
SUBROUTINE LUDCMP(A, N, NP, INDX, D)
.
.
.
END

SUBROUTINE LUBKSB(A, N, NP, INDX, B)
.
.
.
END
```

The subroutine `MNEWT` is substantially modified from Press et al. [40].

```
SUBROUTINE MNEWT(X,PARAMS, PROPNUM)
IMPLICIT NONE
INTEGER I, J, K, N, NP, NTRIAL, NTRIALP
INTEGER D, INDX, PROPNUM
REAL*8 PARAMS, TOLX, TOLF
REAL*8 ZERO, HALF, ONE, TWO, TEN
REAL*8 ERRX, ERRF
REAL*8 X, ALPHA, BETA, INIX
REAL*8 LASTX, LASTLASTX, LASTLASTLASTX
REAL*8 FACTOR, WEIGHT
PARAMETER (NTRIAL=10000, N=4, TOLX=0.00000001, TOLF=0.00000001)
PARAMETER (NP=4)
DIMENSION X(NP),ALPHA(NP,NP),BETA(NP),INDX(NP), PARAMS(7)
DIMENSION LASTX(NP), LASTLASTX(NP), LASTLASTLASTX(NP)
DIMENSION INIX(NP), WEIGHT(NP)
PARAMETER ( ZERO = 0.D0, HALF = 0.5D0, ONE = 1.D0)
PARAMETER ( TWO=2.D0, TEN=1.D1 )
INIX=X
FACTOR=ONE+0.1
NTRIALP=NTRIAL
DO I=1,N
```

```
   WEIGHT(I)=ONE
END DO

DO J=1,10
   FACTOR= FACTOR-0.1
   X=INIX
DO K=1,NTRIALP
   LASTLASTLASTX=LASTLASTX
   LASTLASTX=LASTX
   LASTX=X
   CALL PULLEYANDLATCH(X, N, ALPHA, BETA, PARAMS, PROPNUM)
   ERRF=ZERO
   DO I=1,N
      ERRF=ERRF+ABS(BETA(I))
   END DO

   IF(ERRF.LE.TOLF)RETURN

   CALL LUDCMP(ALPHA,N,NP,INDX,D)
   CALL LUBKSB(ALPHA,N,NP,INDX,BETA)

   ERRX=ZERO
   IF (X(1).GT.(1.D8)) THEN
      WEIGHT(1) = (X(1)/(1.D7))
   ELSE
      WEIGHT(1) = ONE
   END IF
   IF (X(2).GT.(1.D8)) THEN
      WEIGHT(2) = (X(2)/(1.D7))
   ELSE
      WEIGHT(2) = ONE
   END IF
   DO I=1,N
      ERRX=ERRX+ABS(BETA(I))/WEIGHT(I)
      X(I)=X(I)+FACTOR*BETA(I)
   END DO

   IF(ERRX.LE.TOLX) RETURN

END DO
NTRIALP = NTRIALP*1.5
END DO
```

If no solution is found with this relaxed Newton-Raphson method, a fatal error is thrown and the last few solution attempts are reported, in an attempt to identify whether the failure to converge is due to insufficient step or a non-convex problem statement.

```
PRINT *, "Failure in MNEWT, triggering error..."
PRINT *, "PROPNUM=", PROPNUM
PRINT *, "PARAMS=",PARAMS
PRINT *, "X=            ", X
PRINT *, "LASTX=        ", LASTX
PRINT *, "LASTLASTX=    ", LASTLASTX
PRINT *, "LASTLASTLASTX=", LASTLASTLASTX
```

```
      PRINT *, "BETA=", BETA
      PRINT *, "ERRF=", ERRF
      PRINT *, "ERRX=", ERRX
       X(1) = ONE/ZERO
      RETURN
      END
```

The subroutine PULLEYANDLATCH returns the system of equations that can be used by the Newton-Raphson method in MNEWT to solve for the tensions and cable distribution int he system.

```
      SUBROUTINE PULLEYANDLATCH(X, NP, ALPHA, BETA,
     *     PARAMS, PROPNUM)
      IMPLICIT NONE
      INTEGER NP, PROPNUM
      REAL*8 ZERO, HALF, ONE, TWO, THREE, FOUR, FIVE, SIX, TEN
      REAL*8 EA, LB, RADIUS, Fmax, L1, L2, L0
      REAL*8 T1, T2, L10, L20
      REAL*8 ALPHA, X, BETA, PARAMS
      REAL*8 LATCHED
      REAL*8 LATCHING, BEADZONE
      REAL*8 CYLR, K, H, MU, LATXVERT
      REAL*8 CABLEEA, LATCHLB, LATCHBEADR, LATCHH, LATCHXHORIZ, LZERO
      REAL*8 EX, DELTA, DELTRH, TVERT, LATXHOR
      REAL*8 TVERTLAT, TVERTUN
      REAL*8 DELTRHXVERT, DELTAXVERT
      REAL*8 F, MINDT, MAXDT, DFDT1, DFDT2, DFDL10, DFDL20
C     This subroutine returns the linearized equations of the pulley-latch system.
C     The variables passed in as X are T1, T2, L10, L20, EA
      DIMENSION X(NP), ALPHA(NP,NP),BETA(NP), PARAMS(7)
      PARAMETER ( ZERO = 0.D0, HALF = 0.5D0, ONE = 1.D0)
      PARAMETER ( TWO=2.D0, THREE=3.D0, FOUR=4.D0, TEN=1.D1 )
      PARAMETER ( FIVE=5.D0, SIX=6.D0 )
      T1=X(1)
      T2=X(2)
      L10=X(3)
      L20=X(4)
      LATCHING=PARAMS(1)
      BEADZONE=PARAMS(2)
      L1=PARAMS(4)
      L2=PARAMS(5)
      L0 = PARAMS(6)
      LB = PARAMS(7)
C     Variables from latch lookup tables:
      EA = CABLEEA(PROPNUM)
      RADIUS = LATCHBEADR(PROPNUM)
      H = LATCHH(PROPNUM)
      LATXHOR = LATCHXHORIZ(PROPNUM)
      EX = LB-L10;
      DELTRH = SQRT((RADIUS+CYLR)**2-EX**2)
      DELTA = DELTRH - H - CYLR
```

The first row describes the constitutive relationship for cable A.

$$T_A = \begin{cases} 0 & L_A \leq L_A^0 \\ EA\frac{L_A - L_A^0}{L_A^0} & L_A > L_A^0 \end{cases} \tag{C.1}$$

```
      IF (L1.GE.L10) THEN
         ALPHA(1,1)=L10
         ALPHA(1,2)=ZERO
         ALPHA(1,3)=T1+EA
         ALPHA(1,4)=ZERO
         BETA(1)=-(T1*L10-EA*L1+EA*L10)
C     If slack:
      ELSE
         ALPHA(1,1)=ONE
         ALPHA(1,2)=ZERO
         ALPHA(1,3)=ZERO
         ALPHA(1,4)=ZERO
         BETA(1)=-T1
      END IF
```

The second row describes the constitutive relationship for cable B.

$$T_B = \begin{cases} 0 & L_B \leq L_B^0 \\ EA\frac{L_B - L_B^0}{L_B^0} & L_B > L_B^0 \end{cases} \tag{C.2}$$

```
      IF (L2.GE.L20) THEN
         ALPHA(2,1)=ZERO
         ALPHA(2,2)=L20
         ALPHA(2,3)=ZERO
         ALPHA(2,4)=T2+EA
         BETA(2)=-(T2*L20-EA*L2+EA*L20)
      ELSE
C     If slack:
         ALPHA(2,1)=ZERO
         ALPHA(2,2)=ONE
         ALPHA(2,3)=ZERO
         ALPHA(2,4)=ZERO
         BETA(2)=-T2
      END IF
```

The third row describes conservation of total unstretched cable length.

$$L_A^0 + L_B^0 = L^0 \tag{C.3}$$

```
      ALPHA(3,1)=ZERO
      ALPHA(3,2)=ZERO
      ALPHA(3,3)=ONE
      ALPHA(3,4)=ONE
      BETA(3)=L0-L10-L20
```

The fourth row describes the impact of the latch on the system. `LATCHHANDLER` (page 137) is called to produce these values.

$$T_B - T_A = \Delta T(x), \quad x = L_b - L_A^0 \tag{C.4}$$

```
      CALL LATCHHANDLER (T1, T2, L10, L20, PARAMS,
     *     F, MINDT, MAXDT,DFDT1, DFDT2, DFDL10, DFDL20,
     *     PROPNUM)

      ALPHA(4,1)=DFDT1
```

```
ALPHA(4,2)=DFDT2
ALPHA(4,3)=DFDL10
ALPHA(4,4)=DFDL20
BETA(4)=-F
RETURN
END
```

The stiffness matrix is complex and calculated in its own subroutine.

```
SUBROUTINE STIFFNESS(A, N, V1, V1LENGTH, V2, V2LENGTH,
1     SOLN, PARAMS, PROPNUM)
IMPLICIT NONE
INTEGER I, J, K, L
INTEGER INDX, D, FN, DN, N, PROPNUM
REAL*8 ZERO, HALF, ONE, TWO, THREE, FOUR, FIVE, SIX, TEN
REAL*8 A, DERIVMAT, DERIVRHS
REAL*8 T1, T2, L10, L20, EA, Lb, RADIUS, Fmax
REAL*8 L1, L2, L0, V1, V2, V1LENGTH, V2LENGTH
REAL*8 SOLN, PARAMS, LATCHED
REAL*8 LATCHING, BEADZONE
REAL*8 CYLR, LATK, H, MU, LATXVERT
REAL*8 LATX12, LATX23, LATX45, LATX56
REAL*8 LATF12, LATF23, LATF45, LATF56
REAL*8 EX, DELTA, DELTRH, TVERT, LATXHOR, LZERO
REAL*8 TVERTLAT, TVERTUN, STUCK, LATCHXVERT
REAL*8 DELTRHXVERT, DELTAXVERT
REAL*8 F, MINDT, MAXDT, DFDT1, DFDT2, DFDL10, DFDL20
REAL*8 CABLEEA, LATCHLB, LATCHBEADR, LATCHH, LATCHXHORIZ
DIMENSION A(N,N),INDX(N), DERIVMAT(4,4),DERIVRHS(4)
DIMENSION SOLN(4), PARAMS(7)
DIMENSION V1(3), V2(3)
PARAMETER ( ZERO = 0.D0, HALF = 0.5D0, ONE = 1.D0)
PARAMETER ( TWO=2.D0, THREE=3.D0, FOUR=4.D0, TEN=1.D1 )
PARAMETER ( FIVE=5.D0, SIX=6.D0 )
T1=SOLN(1)
T2=SOLN(2)
L10=SOLN(3)
L20=SOLN(4)
LATCHING=PARAMS(1)
BEADZONE=PARAMS(2)
STUCK=PARAMS(3)
L1=PARAMS(4)
L2=PARAMS(5)
EA = CABLEEA(PROPNUM)
L0 = PARAMS(6)
RADIUS = LATCHBEADR(PROPNUM)
LB = PARAMS(7)
H = LATCHH(PROPNUM)
LATXHOR = LATCHXHORIZ(PROPNUM)
EX = LB-L10;
DELTRH = SQRT((RADIUS+CYLR)**2-EX**2)
DELTA = DELTRH - H - CYLR

DO I=1,4
```

```
         DO J=1,4
            DERIVMAT(I,J)=ZERO
         END DO
      END DO
      DO I=1,N
         DO J=1,N
            A(I,J)=ZERO
         END DO
      END DO
      DERIVMAT(1,1)=L10**TWO
      DERIVMAT(1,3)=EA*L1
      IF (T1.EQ.ZERO) THEN
         DERIVMAT(1,1)=ONE
         DERIVMAT(1,3)=ZERO
      END IF
      DERIVMAT(2,2)=L20**TWO
      DERIVMAT(2,4)=EA*L2
      IF (T2.EQ.ZERO) THEN
         DERIVMAT(2,2)=ONE
         DERIVMAT(2,4)=ZERO
      END IF
      DERIVMAT(3,3)=ONE
      DERIVMAT(3,4)=ONE
      IF ((STUCK.GT.ZERO).OR.(EX.LE.LATCHXVERT(PROPNUM))) THEN
         DERIVMAT(4,3)=ONE
      ELSE
         CALL LATCHHANDLER (T1, T2, L10, L20, PARAMS,
     *        F, MINDT, MAXDT,DFDT1, DFDT2, DFDL10, DFDL20,
     *        PROPNUM)

         DERIVMAT(4,1)=DFDT1
         DERIVMAT(4,2)=DFDT2
         DERIVMAT(4,3)=DFDL10
         DERIVMAT(4,4)=DFDL20
      END IF

C     Do the LU decomposition first because it only needs to be done once
C     Within the loop LUBKSB will be called several times

      CALL LUDCMP(DERIVMAT, 4, 4, INDX, D)
      DERIVRHS(3)=ZERO
      DERIVRHS(4)=ZERO

C     "I" will be the force point number
C     "J" will be the force direction number
C     "K" will be the displacement point number
C     "L" will be the displacement direction number
C     Will calculate values for F at points 1 and 3 and add them for 2

      DO J=1,3
         DO K=1,3
            DO L=1,3
               DERIVRHS(1)=ZERO
               DERIVRHS(2)=ZERO
```

```
               DERIVRHS(3)=ZERO
               DERIVRHS(4)=ZERO
               DN = 3*(K-1)+L
C     Cases (1,1-3),(2,1-3),(3,1-3),(7,7-9),(8,7-9),(9,7-9) (i.e. 18 cases)
               IF (K.EQ.1) THEN
                  DERIVRHS(1)=EA*SOLN(3)*V1(L)
                  DERIVRHS(2)=ZERO
                  IF (T1.EQ.ZERO) THEN
                     DERIVRHS(1)=ZERO
                  END IF
                  IF (T2.EQ.ZERO) THEN
                     DERIVRHS(2)=ZERO
                  END IF
                  IF ((T1.EQ.ZERO).AND.(T2.EQ.ZERO)) THEN
                     DERIVRHS(1)=ZERO
                     DERIVRHS(2)=ZERO
                     DERIVRHS(3)=ZERO
                     DERIVRHS(4)=ZERO
                  ELSE
                     CALL
     *                    LUBKSB(DERIVMAT, 4, 4, INDX, DERIVRHS)
                  END IF
                  IF (J.EQ.L) THEN
                     A(J, DN)
     *                    =T1*(ONE-V1(J)*V1(L))/V1LENGTH
     *                    + V1(J)*DERIVRHS(1)
                  ELSE
                     A(J, DN)
     *                    =T1*(-V1(J)*V1(L))/V1LENGTH
     *                    + V1(J)*DERIVRHS(1)
                  END IF
                  A(6+J, DN)= V2(J)*DERIVRHS(2)
               ELSE IF (K.EQ.2) THEN
                  DERIVRHS(1)=-EA*SOLN(3)*V1(L)
                  DERIVRHS(2)=-EA*SOLN(4)*V2(L)
                  IF (T1.EQ.ZERO) THEN
                     DERIVRHS(1)=ZERO
                  END IF
                  IF (T2.EQ.ZERO) THEN
                     DERIVRHS(2)=ZERO
                  END IF
                  IF ((T1.EQ.ZERO).AND.(T2.EQ.ZERO)) THEN
                     DERIVRHS(1)=ZERO
                     DERIVRHS(2)=ZERO
                     DERIVRHS(3)=ZERO
                     DERIVRHS(4)=ZERO
                  ELSE
                     CALL
     *                    LUBKSB(DERIVMAT, 4, 4, INDX, DERIVRHS)
                  END IF
                  IF (J.EQ.L) THEN
                     A(J, DN)
     *                    =-T1*(ONE-V1(J)*V1(L))/V1LENGTH
     *                    + V1(J)*DERIVRHS(1)
```

```
                  A(3+J, DN)
     *                 =-(-T1*(ONE-V1(J)*V1(L))/V1LENGTH
     *                 + V1(J)*DERIVRHS(1)
     *                 -T2*(ONE-V2(J)*V2(L))/V2LENGTH
     *                 + V2(J)*DERIVRHS(2))
                  A(6+J, DN)
     *                 =-T2*(ONE-V2(J)*V2(L))/V2LENGTH
     *                 + V2(J)*DERIVRHS(2)
               ELSE
                  A(J, DN)
     *                 =T1*(V1(J)*V1(L))/V1LENGTH
     *                 + V1(J)*DERIVRHS(1)
                  A(3+J, DN)
     *                 =-(T1*(V1(J)*V1(L))/V1LENGTH
     *                 + V1(J)*DERIVRHS(1)
     *                 + T2*(V2(J)*V2(L))/V2LENGTH
     *                 + V2(J)*DERIVRHS(2))
                  A(6+J, DN)
     *                 =T2*(V2(J)*V2(L))/V2LENGTH + V2(J)*DERIVRHS(2)
               END IF
            ELSE IF (K.EQ.3) THEN
               DERIVRHS(1)=ZERO
               DERIVRHS(2)=EA*SOLN(4)*V2(L)
               IF (T1.EQ.ZERO) THEN
                  DERIVRHS(1)=ZERO
               END IF
               IF (T2.EQ.ZERO) THEN
                  DERIVRHS(2)=ZERO
               END IF
               IF ((T1.EQ.ZERO).AND.(T2.EQ.ZERO)) THEN
                  DERIVRHS(1)=ZERO
                  DERIVRHS(2)=ZERO
                  DERIVRHS(3)=ZERO
                  DERIVRHS(4)=ZERO
               ELSE
                  CALL
     *                 LUBKSB(DERIVMAT, 4, 4, INDX, DERIVRHS)
               END IF
               IF (J.EQ.L) THEN
                  A(6+J, DN)
     *                 =T2*(ONE-V2(J)*V2(L))/V2LENGTH
     *                 + V2(J)*DERIVRHS(2)
               ELSE
                  A(6+J, DN)
     *                 =T2*(-V2(J)*V2(L))/V2LENGTH
     *                 + V2(J)*DERIVRHS(2)
               END IF
               A(J, DN)= V1(J)*DERIVRHS(1)
            END IF
         END DO
      END DO
   END DO
C    The remaining cases: (4-6,1-9) (i.e. 27 cases)
   DO I=4,6
```

```
      DO J=1,9
         A(I,J) = -(A(I-3,J)+A(I+3,J))
      END DO
    END DO
    RETURN
    END
```

The code after this point is generated from within Matlab for a variety of reasons. `LATCHHANDLER` is used for sorting out whether the lookup tables or analytical function should be used to describe the current state of the latch and also handles the shape of the curve $\Delta T(x)$ for values x outside the current zone.

```
      SUBROUTINE LATCHHANDLER(T1, T2, L10, L20, PARAMS,
     1      F, MINDT, MAXDT,
     2      DFDT1, DFDT2, DFDL10, DFDL20, PROPNUM)
      IMPLICIT NONE
      REAL*8 T1, T2, L10, L20, L1, L2
      REAL*8 DFDT1, DFDT2, DFDL10, DFDL20
      REAL*8 F, MAXDT, MINDT
      REAL*8 EX, DT, PARAMS
      REAL*8 ZERO, HALF, ONE
      REAL*8 TWO, THREE, FOUR, FIVE, SIX, TINY, HUGE
      REAL*8 X12, X23, X45, X56, XLOOKUP, DFDX, LATCHXHORIZ
      REAL*8 LATCHLB, LB, LATCHING, ZONE
      REAL*8 LATCHXVERT, LATCHFVERTLA, LATCHFVERTUN
      INTEGER PROPNUM, NPROPNUM
      DIMENSION PARAMS(7)
      PARAMETER ( ZERO = 0.D0, HALF = 0.5D0, ONE = 1.D0)
      PARAMETER ( TWO=2.D0, THREE=3.D0, FOUR=4.D0 )
      PARAMETER ( FIVE=5.D0, SIX=6.D0 )
      PARAMETER ( TINY=1.D-6, HUGE=1.D8 )
      LB = PARAMS(7)
      EX = LB-L10
      LATCHING=PARAMS(1)
      ZONE=PARAMS(2)
      L1=PARAMS(4)
      L2=PARAMS(5)
      DFDL10= ZERO
      DFDL20= ZERO
      DFDT1= ZERO
      DFDT2= ZERO
      F= ZERO
      DT = T2-T1
         DFDT1=-1
         DFDT2= 1
       IF ((ZONE.LT.(SIX+TINY)).AND.(ZONE.GT.(SIX-TINY))) THEN
        IF (XLOOKUP(PROPNUM).LT.LATCHXVERT(PROPNUM)) THEN
         IF (((T2-T1).LE.LATCHFVERTLA(PROPNUM)).
     * AND.(EX.LT.X56(PROPNUM))) THEN
          DFDL10= 1
          F= -(EX-LATCHXVERT(PROPNUM))
          IF (EX.LT.LATCHXVERT(PROPNUM)) THEN
           MAXDT=-HUGE
           MINDT=-HUGE
          ELSE IF (EX.EQ.LATCHXVERT(PROPNUM)) THEN
```

```
      MAXDT=LATCHFVERTUN(PROPNUM)
      MINDT=-HUGE
     ELSE
      CALL ANACASE(EX, DT, LATCHING, MAXDT, MINDT,
* DFDX, F, PROPNUM, NPROPNUM)
     END IF
     DFDT1=ZERO
     DFDT2=ZERO
    ELSE IF (EX.LE.LATCHXVERT(PROPNUM)) THEN
     CALL ANACASE(LATCHXVERT(PROPNUM), DT, LATCHING, MAXDT, MINDT,
* DFDX, F, PROPNUM, NPROPNUM)
     DFDL10= 1
     DFDT1=-1
     DFDT2= 1
     IF (EX.EQ.LATCHXVERT(PROPNUM)) THEN
      MAXDT=LATCHFVERTUN(PROPNUM)
      MINDT=-HUGE
     ELSE
     MAXDT=-HUGE
     MINDT=-HUGE
     END IF
     F=(T2-T1-F)-(EX-LATCHXVERT(PROPNUM))
    ELSE IF (EX.LE.X56(PROPNUM)) THEN
     CALL ANACASE(EX, DT, LATCHING, MAXDT, MINDT,
* DFDX, F, PROPNUM, NPROPNUM)
     DFDL10= DFDX
     F=(T2-T1-F)
    ELSE
     CALL ANACASE(X56(PROPNUM), DT, LATCHING, MAXDT, MINDT,
* DFDX, F, PROPNUM, NPROPNUM)
     DFDL10= ZERO
     DFDL20= ZERO
     F=(T2-T1-F)
    END IF
   ELSE
    IF (EX.LT.XLOOKUP(PROPNUM)) THEN
     CALL LOOKUPU(PROPNUM, EX, F, DFDX)
     MAXDT=F
     CALL LOOKUPL(PROPNUM, EX, F, DFDX)
     MINDT=F
     DFDL10= DFDX
     F=(T2-T1-F)
    ELSE IF (EX.LT.X56(PROPNUM)) THEN
     CALL ANACASE(EX, DT, LATCHING, MAXDT, MINDT,
* DFDX, F, PROPNUM, NPROPNUM)
     DFDL10= DFDX
     F=(T2-T1-F)
    ELSE
     CALL ANACASE(X56(PROPNUM), DT, LATCHING, MAXDT, MINDT,
* DFDX, F, PROPNUM, NPROPNUM)
     DFDL10= ZERO
     F=(T2-T1-F)
    END IF
   END IF
```

```
  ELSE IF ((ZONE.LT.(FIVE+TINY)).AND.(ZONE.GT.(FIVE-TINY))) THEN
   IF (EX.LT.X56(PROPNUM)) THEN
    CALL ANACASE(X56(PROPNUM), DT, LATCHING, MAXDT, MINDT,
* DFDX, F, PROPNUM, NPROPNUM)
    DFDL10= ZERO
    F=(T2-T1-F)
   ELSE IF (EX.LT.X45(PROPNUM)) THEN
    CALL ANACASE(EX, DT, LATCHING, MAXDT, MINDT,
* DFDX, F, PROPNUM, NPROPNUM)
    DFDL10= DFDX
    F=(T2-T1-F)
   ELSE
    CALL ANACASE(X45(PROPNUM), DT, LATCHING, MAXDT, MINDT,
* DFDX, F, PROPNUM, NPROPNUM)
    DFDL10= ZERO
    F=(T2-T1-F)
   END IF
  ELSE IF ((ZONE.LT.(FOUR+TINY)).AND.(ZONE.GT.(FOUR-TINY))) THEN
   IF (EX.LT.X45(PROPNUM)) THEN
    CALL ANACASE(X45(PROPNUM), DT, LATCHING, MAXDT, MINDT,
* DFDX, F, PROPNUM, NPROPNUM)
    DFDL10= ZERO
    F=(T2-T1-F)
   ELSE IF (EX.LT.LATCHXHORIZ(PROPNUM)) THEN
    CALL ANACASE(EX, DT, LATCHING, MAXDT, MINDT,
* DFDX, F, PROPNUM, NPROPNUM)
    DFDL10= DFDX
    F=(T2-T1-F)
   ELSE
    DFDL10= ZERO
    F=(T2-T1)
    MINDT= ZERO
    MAXDT= ZERO
   END IF
   DFDL20= ZERO
  ELSE IF ((ZONE.LT.(ONE+TINY)).AND.(ZONE.GT.(ONE-TINY))) THEN
   IF (XLOOKUP(PROPNUM).LT.LATCHXVERT(PROPNUM)) THEN
    IF (((T2-T1).LE.LATCHFVERTUN(PROPNUM)).
* AND.(EX.LT.X12(PROPNUM))) THEN
     DFDL10= 1
     F= -(EX-LATCHXVERT(PROPNUM))
     IF (EX.LT.LATCHXVERT(PROPNUM)) THEN
      MAXDT=-HUGE
      MINDT=-HUGE
     ELSE IF (EX.EQ.LATCHXVERT(PROPNUM)) THEN
      MAXDT=LATCHFVERTUN(PROPNUM)
      MINDT=-HUGE
     ELSE
      CALL ANACASE(EX, DT, LATCHING, MAXDT, MINDT,
* DFDX, F, PROPNUM, NPROPNUM)
     END IF
     DFDT1=ZERO
     DFDT2=ZERO
    ELSE IF (EX.LE.LATCHXVERT(PROPNUM)) THEN
```

```
     CALL ANACASE(LATCHXVERT(PROPNUM), DT, LATCHING, MAXDT, MINDT,
* DFDX, F, PROPNUM, NPROPNUM)
     DFDL10= 1
     DFDT1=-1
     DFDT2= 1
     IF (EX.EQ.LATCHXVERT(PROPNUM)) THEN
      MAXDT=LATCHFVERTUN(PROPNUM)
      MINDT=-HUGE
     ELSE
      MAXDT=-HUGE
      MINDT=-HUGE
     END IF
     F=(T2-T1-F)-(EX-LATCHXVERT(PROPNUM))
    ELSE IF (EX.LE.X12(PROPNUM)) THEN
     CALL ANACASE(EX, DT, LATCHING, MAXDT, MINDT,
* DFDX, F, PROPNUM, NPROPNUM)
     DFDL10= DFDX
     F=(T2-T1-F)
    ELSE
     CALL ANACASE(X12(PROPNUM), DT, LATCHING, MAXDT, MINDT,
* DFDX, F, PROPNUM, NPROPNUM)
     DFDL10= ZERO
     DFDL20= ZERO
     F=(T2-T1-F)
    END IF
   ELSE
    IF (EX.LT.XLOOKUP(PROPNUM)) THEN
     CALL LOOKUPL(PROPNUM, EX, F, DFDX)
     MINDT=F
     CALL LOOKUPU(PROPNUM, EX, F, DFDX)
     MAXDT=F
     DFDL10= DFDX
     F=(T2-T1-F)
    ELSE IF (EX.LT.X12(PROPNUM)) THEN
     CALL ANACASE(EX, DT, LATCHING, MAXDT, MINDT,
* DFDX, F, PROPNUM, NPROPNUM)
     DFDL10= DFDX
     F=(T2-T1-F)
    ELSE
     CALL ANACASE(X12(PROPNUM), DT, LATCHING, MAXDT, MINDT,
* DFDX, F, PROPNUM, NPROPNUM)
     DFDL10= ZERO
     DFDL20= ZERO
     F=(T2-T1-F)
    END IF
   END IF
  ELSE IF ((ZONE.LT.(TWO+TINY)).AND.(ZONE.GT.(TWO-TINY))) THEN
  .
  .
  .
  ELSE IF ((ZONE.LT.(THREE+TINY)).AND.(ZONE.GT.(THREE-TINY))) THEN
  .
  .
  .
```

```
 ELSE
END IF
RETURN
END
```

The properties of the latch can be looked up through these functions. The transition points between zones are location at bead positions $x =$ `X12`, `X23`, `X45` and `X56`. The point in zone one of transition to the lookup table is `XLOOKUP`. `LATCHXVERT` is the position of the backstop, and the values ΔT at this transition point of zone one are `LATCHFVERTLA` and `LATCHFVERTUN`. `LATCHLB` is the initial position of the bead on the (un-stretched) cable, which can be modified through the control nodes. The latch dimentions and constitutive properties used in the analytical fit are encoded here as `LATCHMU`, `CABLEEA`, `LATCHK`, `LATCHH`, `LATCHBEADR`, and `LATCHCYLR`. The bead position at which the bead is no longer contacting the latch is `LATCHXHORIZ`.

```
REAL*8 FUNCTION X12(PROPNUM)
INTEGER PROPNUM
IF (PROPNUM.EQ.1) THEN
 X12=-1.34928301e-003
 RETURN
END IF
.
.
.
RETURN
END

REAL*8 FUNCTION X23(PROPNUM)
INTEGER PROPNUM
IF (PROPNUM.EQ.1) THEN
 X23=1.47257260e-003
 RETURN
END IF
.
.
.
RETURN
END

REAL*8 FUNCTION X45(PROPNUM)
INTEGER PROPNUM
IF (PROPNUM.EQ.1) THEN
 X45=1.34928301e-003
 RETURN
END IF
.
.
.
RETURN
END

REAL*8 FUNCTION X56(PROPNUM)
INTEGER PROPNUM
IF (PROPNUM.EQ.1) THEN
 X56=-1.47257260e-003
 RETURN
```

```
END IF
.
.
.
RETURN
END

REAL*8 FUNCTION XLOOKUP(PROPNUM)
INTEGER PROPNUM
IF (PROPNUM.EQ.1) THEN
 XLOOKUP=-1.59238457e-003
 RETURN
END IF
.
.
.
RETURN
END

REAL*8 FUNCTION LATCHXVERT(PROPNUM)
INTEGER PROPNUM
IF (PROPNUM.EQ.1) THEN
 LATCHXVERT=-1.15923846e-002
 RETURN
END IF
.
.
.
RETURN
END

REAL*8 FUNCTION LATCHFVERTLA(PROPNUM)
INTEGER PROPNUM
IF (PROPNUM.EQ.1) THEN
 LATCHFVERTLA=-1.23056128e+003
 RETURN
END IF
.
.
.
RETURN
END

REAL*8 FUNCTION LATCHFVERTUN(PROPNUM)
INTEGER PROPNUM
IF (PROPNUM.EQ.1) THEN
 LATCHFVERTUN=1.23056128e+003
 RETURN
END IF
.
.
.
RETURN
END
```

```
REAL*8 FUNCTION LATCHLB(PROPNUM)
INTEGER PROPNUM
IF (PROPNUM.EQ.1) THEN
 LATCHLB=1.34395634e-001
 RETURN
END IF
.
.
.
RETURN
END

REAL*8 FUNCTION LATCHMU(PROPNUM)
INTEGER PROPNUM
IF (PROPNUM.EQ.1) THEN
 LATCHMU=1.48090600e-001
 RETURN
END IF
.
.
.
RETURN
END

REAL*8 FUNCTION CABLEEA(PROPNUM)
INTEGER PROPNUM
IF (PROPNUM.EQ.1) THEN
 CABLEEA=7.30420292e+004
 RETURN
END IF
.
.
.
RETURN
END

REAL*8 FUNCTION LATCHK(PROPNUM)
INTEGER PROPNUM
IF (PROPNUM.EQ.1) THEN
 LATCHK=5.88400315e+004
 RETURN
END IF
.
.
.
RETURN
END

REAL*8 FUNCTION LATCHH(PROPNUM)
INTEGER PROPNUM
IF (PROPNUM.EQ.1) THEN
 LATCHH=1.34240199e-003
 RETURN
```

```
 END IF
 .
 .
 .
 RETURN
 END

 REAL*8 FUNCTION LATCHBEADR(PROPNUM)
 INTEGER PROPNUM
 IF (PROPNUM.EQ.1) THEN
  LATCHBEADR=2.38500000e-003
  RETURN
 END IF
 .
 .
 .
 RETURN
 END

 REAL*8 FUNCTION LATCHCYLR(PROPNUM)
 INTEGER PROPNUM
 IF (PROPNUM.EQ.1) THEN
  LATCHCYLR=2.06157324e-004
  RETURN
 END IF
 .
 .
 .
 RETURN
 END

 REAL*8 FUNCTION LATCHXHORIZ(PROPNUM)
 INTEGER PROPNUM
 IF (PROPNUM.EQ.1) THEN
  LATCHXHORIZ=2.07751301e-003
  RETURN
 END IF
 .
 .
 .
 RETURN
 END
```

If the event that we are using the analytical model of the latch, `ANACASE` is called.

```
 SUBROUTINE ANACASE(EX, DT, LATCHING,
*MAXDT, MINDT, DFDX, F, PROPNUM, NPROPNUM)
 IMPLICIT NONE
 INTEGER PROPNUM, NPROPNUM
 REAL*8 T1, T2, L10, L20
 REAL*8 DFDT1, DFDT2, DFDL10, DFDL20
 REAL*8 F, DFDX, MAXDT, MINDT
 REAL*8 EX, DT, PARAMS, LATCHING
 REAL*8 MU, K, H, RADIUS, CYLR, DELTRH, DELTA
```

```
 REAL*8 LATCHMU, LATCHK, LATCHH, LATCHBEADR
 REAL*8 LATCHCYLR
 REAL*8 ZERO, HALF, ONE, TWO, THREE, FOUR, FIVE, SIX
 DIMENSION PARAMS(3)
 PARAMETER ( ZERO = 0.D0, HALF = 0.5D0, ONE = 1.D0)
 PARAMETER ( TWO=2.D0, THREE=3.D0, FOUR=4.D0 )
 PARAMETER ( FIVE=5.D0, SIX=6.D0 )
 MU=LATCHMU(PROPNUM)
 K=LATCHK(PROPNUM)
 H=LATCHH(PROPNUM)
 RADIUS=LATCHBEADR(PROPNUM)
 CYLR=LATCHCYLR(PROPNUM)
 IF (((RADIUS+CYLR)**2-EX**2).LT.ZERO) THEN
    PRINT *, "In ANACASE, SQRT of", (RADIUS+CYLR)**2-EX**2
    PRINT *, "In ANACASE, EX=", EX
  MAXDT = -ONE
  MINDT = ONE
  RETURN
 END IF
 DELTRH = SQRT((RADIUS+CYLR)**2-EX**2)
 DELTA = DELTRH - H - CYLR
 MAXDT = -(TWO*K*DELTA * (EX-MU*DELTRH)
*              /(DELTRH+MU*EX))
 MINDT = -(TWO*K*DELTA * (EX+MU*DELTRH)
*              /(DELTRH-MU*EX))
 IF (LATCHING.GT.ZERO) THEN
  DFDX = TWO*K/(DELTRH-MU*EX)*ONE/DELTRH *
*              ( (EX+MU*DELTRH)*(EX-DELTA*(EX+MU*DELTRH)
*              /(DELTRH-MU*EX))
*              + DELTA*(MU*EX-DELTRH) )
  F=MINDT
 ELSE
  DFDX = TWO*K/(DELTRH+MU*EX)*ONE/DELTRH *
*              ( (EX-MU*DELTRH)*(EX-DELTA*(EX-MU*DELTRH)
*              /(DELTRH+MU*EX))
*              + DELTA*(-MU*EX-DELTRH) )
  F=MAXDT
 END IF
 RETURN
 END
```

The lookup table subroutine for the latching direction is coded by first defining vectors `YS` $= \Delta T$ and `XS` $= x$ for each `PROPNUM`. Local cubic interpolation is then used to find the correct value to return to the calling function.

```
 SUBROUTINE LOOKUPL(PROPNUM, X, Y, M)
 IMPLICIT NONE
 REAL*8 X, Y, M
 REAL*8 X1, X2, XA
 REAL*8 XS, YS, XPERC
 REAL*8 T, FB, FA, Y1, Y2, M1, M2
 REAL*8 MA, MB, MC
 REAL*8 ZERO, ONE, TWO
 INTEGER A1, A2, A, XDIM, PROPNUM
```

```
DIMENSION XS(377), YS(377)
PARAMETER ( ZERO = 0.D0, ONE = 1.D0)
PARAMETER ( TWO=2.D0 )
XDIM=377
IF (PROPNUM.EQ.1) THEN
 XS(1)=-0.0018719946
 XS(2)=-0.0018619946
 .
 .
 .
 XS(377)=-0.0015745964
 YS(1)=-80.450367
 YS(2)=19.549633
 .
 .
 .
 YS(377)=33.25599
END IF
.
.
.
IF (PROPNUM.EQ.4) THEN
 XS(1)=-0.00198774
 .
 .
 .
 YS(377)=32.987726
END IF
```

A bisection algorithm is used here to find the two defined points `X1` and `X2` between which the desired return value `Y(X)` can be found.

```
A1=1
A2=377
X1=XS(A1)
X2=XS(A2)
IF (X.LE.X1) THEN
 A1=1
 A2=2
 X1=XS(A1)
 X2=XS(A2)
 Y = YS(A1)+(YS(A2)-YS(A1)) * (X-X1)/(X2-X1)
 M = (YS(A2)-YS(A1))/(X2-X1)
 RETURN
END IF
IF (X.GE.X2) THEN
 A1=XDIM-1
 A2=XDIM
 X1=XS(A1)
 X2=XS(A2)
 Y = YS(A1)+(YS(A2)-YS(A1)) * (X-X1)/(X2-X1)
 M = (YS(A2)-YS(A1))/(X2-X1)
 RETURN
END IF
```

```
DO WHILE ((A2-A1).GT.1)
 XPERC =(X-X1)/(X2-X1)
 A = A1 + (A2-A1) * XPERC
 XA =XS(A)
 IF (XA.LT.X) THEN
  IF (A1.EQ.A) THEN
   IF (XS(A+1).LE.X) THEN
    A1 = A+1
   ELSE
    A2 = A+1
   END IF
  ELSE
   A1=A
  END IF
 END IF
 IF (XA.GT.X) THEN
  IF (A2.EQ.A) THEN
   IF (XS(A-1).GE.X) THEN
    A2 = A-1
   ELSE
    A1 = A-1
   END IF
  ELSE
   A2=A
  END IF
 END IF
 IF (XA.EQ.X) THEN
  Y = YS(A)
  M = (YS(A+1)-YS(A-1))/(XS(A+1)-XS(A-1))
 END IF
 X1=XS(A1)
 X2=XS(A2)
 XPERC = (X-X1)/(X2-X1)
END DO
```

At this point we know we need to find a value `Y` between the two index values `YS(A1)` and `YYS(A2)`. To perform the cubic interpolation we define slopes at `X1` and `X2` for a number of special cases and also as described in 5.2.3.2.

```
Y1 = YS(A1)
Y2 = YS(A2)
IF (A1.EQ.1) THEN
 M1 = (YS(A1+1)-YS(A1))/(XS(A1+1)-XS(A1))
 MB = (YS(A2)-YS(A1))/(XS(A2)-XS(A1))
 MC = (YS(A2+1)-YS(A2))/(XS(A2+1)-XS(A2))
 IF (MC.LT.MB) THEN
  M2 = MC
 ELSE
  M2 = MB
 END IF
ELSE IF (A2.EQ.377) THEN
 M2 = (YS(A2)-YS(A2-1))/(XS(A2)-XS(A2-1))
 MA = (YS(A1)-YS(A1-1))/(XS(A1)-XS(A1-1))
 MB = (YS(A2)-YS(A1))/(XS(A2)-XS(A1))
```

```
       IF (MA.LT.MB) THEN
        M1 = MA
       ELSE
        M1 = MB
       END IF
      ELSE
       MA = (YS(A1)-YS(A1-1))/(XS(A1)-XS(A1-1))
       MB = (YS(A2)-YS(A1))/(XS(A2)-XS(A1))
       MC = (YS(A2+1)-YS(A2))/(XS(A2+1)-XS(A2))
       IF (MA.LT.MB) THEN
        M1 = MA
       ELSE
        M1 = MB
       END IF
       IF (MC.LT.MB) THEN
        M2 = MC
       ELSE
        M2 = MB
       END IF
      END IF
C From the wikipedia article on cubic splines
      T = XPERC
       IF (XPERC.GT.ONE) THEN
        PRINT *, "Error, XPERC=",XPERC
        Y=ONE/ZERO
       END IF
       IF (XPERC.LT.ZERO) THEN
        PRINT *, "Error, XPERC=",XPERC
        Y=ONE/ZERO
       END IF
      FA =  M1*(X2-X1)-(Y2-Y1)
      FB = -M2*(X2-X1)+(Y2-Y1)
      Y = (1-T)*Y1 + T*Y2 + T*(1-T)*(FA*(1-T)+FB*T)
      M = (Y2-Y1)/(X2-X1) + (ONE- TWO*T)*
     * (FA*(1-T)+FB*T)/(X2-X1)
     * + T*(1-T)*(FB-FA)/(X2-X1)
      RETURN
      END
```

The lookup table subroutine for the unlatching direction is functionally identical to that in the latching direction.

```
      SUBROUTINE LOOKUPU(PROPNUM, X, Y, M)
      .
      .
      .
      END
```

Appendix D

Abaqus `.inp` sample file

This is an abbreviated Abaqus `.inp` file for a one-bay mast.

```
**
** Nodal coordinates section
**
*PREPRINT, MODEL=YES
*PART, NAME=Mast
*NODE
1, 0.019, 0, 0
.
.
.
193, 0, 0.0385, 0.171
*NSET, NSET=corner1
1, 3, 4, 66, 67, 2
*RIGID BODY, REF NODE=1, TIE NSET=corner1
.
.
.
*RIGID BODY, REF NODE=61, TIE NSET=corner4
*NSET, NSET=pulley1
12, 13, 14, 15, 16
*RIGID BODY, REF NODE=12, TIE NSET=pulley1
*NSET, NSET=pulley2
.
.
.
*RIGID BODY, REF NODE=72, TIE NSET=pulley4
*NSET, NSET=ControlBody
89, 100, 68, 9, 11,
92, 91, 8, 29, 31,
95, 94, 28, 49, 51,
98, 97, 48, 69, 71,
101
*NSET, NSET=ControlNode
101
*RIGID BODY, REF NODE=101, TIE NSET=ControlBody
*NSET, NSET=BattenNodes
1, 122,
```

```
.
.
.
193, 100
*ELEMENT, TYPE=B33, ELSET=Battens
1, 1, 122
.
.
.
80, 193, 100
*BEAM GENERAL SECTION, SECTION=CIRC, ELSET=Battens, DENSITY=4537.68
0.003055

2.2e+011, 80.E9
*SECTION POINTS
0, 0
0, 0
*NSET, NSET=LongeronNodes
5, 102,
.
.
.
121, 70
*ELEMENT, TYPE=B33, ELSET=Longerons
81, 5, 102
.
.
.
104, 121, 70
*BEAM GENERAL SECTION, SECTION=CIRC, ELSET=Longerons, DENSITY=2520.3
0.004785
1, 0, 0
7e+010,80.E9
*SECTION POINTS
0, 0
0, 0
*USER ELEMENT, NODES=3, TYPE=U2, PROPERTIES=3, COORDINATES=3, VARIABLES=6
1,2,3
*ELEMENT, TYPE=U2, ELSET=Cables1
105, 3, 12, 81
.
.
.
*ELEMENT, TYPE=U2, ELSET=Cables8
112, 66, 73, 88
*UEL PROPERTY, ELSET=Cables1
9.3e+010, 7.85398e-007, 0.127991
.
.
.
*UEL PROPERTY, ELSET=Cables8
9.3e+010, 7.85398e-007, 0.128089
*USER ELEMENT, NODES=7, TYPE=U3, PROPERTIES=20, I PROPERTIES=1, COORDINATES=3, VARIABLES=8
1,2,3
```

```
*NSET, NSET=U3CableNodes
8, 16, 11, 17, 18, 19, 20,
28, 36, 31, 37, 38, 39, 40,
48, 56, 51, 57, 58, 59, 60,
68, 76, 71, 77, 78, 79, 80
*NSET, NSET=U3dummy1
17,
37,
57,
77
*NSET, NSET=U3dummy2
18,
38,
58,
78
*NSET, NSET=U3dummy3
19,
39,
59,
79
*NSET, NSET=U3CableDummyNodes
17,
.
.
.
80
*ELEMENT, TYPE=U3, ELSET=U3_OddCablesBay1Side1
121, 8, 16, 11, 17, 18, 19, 20
```

Properties of latch user elements are no longer actually used by the subroutine, but included for legacy reasons.

```
*UEL PROPERTY, ELSET=U3_OddCablesBay1Side1
7.85398e-007, 9.3e+010, 0.271729, 0, 0.002385, 60, 0.134327, 0.000240261,
57601.7, 0.00131063, 0.134621, -0.00138458, 64.5301, 0.00149611, -35.7076, 0.00138458,
-64.5301, -0.00149611, 35.7076, -0.0115261, 1
** The above cable uses lookup table 3
.
.
.
*NSET, NSET=LongeronConnectorNodes
4, 5,
.
.
.
69, 70
*ELEMENT, TYPE=CONN3D2, ELSET=LongeronConnectors_1_1_1
125, 4, 5
*CONNECTOR SECTION, ELSET=LongeronConnectors_1_1_1, BEHAVIOR=BallEnd_1_1_1
join,rotation
.
.
.
*ELEMENT, TYPE=CONN3D2, ELSET=LongeronConnectors_1_4_2
```

```
132, 69, 70
*CONNECTOR SECTION, ELSET=LongeronConnectors_1_4_2, BEHAVIOR=BallEnd_1_4_2
join,rotation
*END PART
**Connector behaviors ********************
*CONNECTOR BEHAVIOR, NAME=BallEnd_1_1_1
*CONNECTOR DERIVED COMPONENT, NAME=normal
1,2,3
1,1,1
*CONNECTOR FRICTION, CONTACT FORCE=normal
*CONNECTOR POTENTIAL
4, 0.004
5, 0.004
6, 0.004
*FRICTION
0.13028
.
.
.
**Assembly section ********************************
*ASSEMBLY, NAME=OnlyAssembly
*INSTANCE, NAME=Mast_Inst, Part=Mast
0,0,0
*END INSTANCE
*END ASSEMBLY
**********************************
*STEP, NLGEOM=YES, INC=300000, EXTRAPOLATION=NO, NAME=INI_STB_0_BAY_1_ssc1_side4
*****
*STATIC, STABILIZE, FACTOR=0
0.2, 1, 10e-8, 0.5
*CONTROLS, PARAMETERS=TIME INCREMENTATION
8, 10, 9, 16, 10, 4, 12, 10, 6, 3, 50, 50, 6
0.25, 0.5, 0.75, 0.85, 0.25, 0.25, 1.5, 0.75
0.8, 1.5, 1.25, 2.0, 0.95, 0.1, 1.0, 0.95
*BOUNDARY, OPT=NEW
**Fixed joints
OnlyAssembly.Mast_Inst.1, 1
OnlyAssembly.Mast_Inst.1, 2
OnlyAssembly.Mast_Inst.1, 3
OnlyAssembly.Mast_Inst.1, 4
OnlyAssembly.Mast_Inst.1, 5
OnlyAssembly.Mast_Inst.1, 6
.
.
.
**Fixed joints: dummy nodes (U3)
OnlyAssembly.Mast_Inst.17, 1
OnlyAssembly.Mast_Inst.17, 2
OnlyAssembly.Mast_Inst.17, 3
.
.
.
OnlyAssembly.Mast_Inst.80, 1, , 0
OnlyAssembly.Mast_Inst.80, 2, , 0.000403521
```

```
OnlyAssembly.Mast_Inst.80, 3, , 0.000807043
**Locked DOFs of the control nodes
*BOUNDARY, TYPE=VELOCITY, OP=NEW
**Temporarily locked joints
OnlyAssembly.Mast_Inst.89, 1
OnlyAssembly.Mast_Inst.89, 2
OnlyAssembly.Mast_Inst.89, 3
OnlyAssembly.Mast_Inst.89, 4
OnlyAssembly.Mast_Inst.89, 5
OnlyAssembly.Mast_Inst.89, 6
.
.
.
**Pulleys locked alone
OnlyAssembly.Mast_Inst.12, 1
OnlyAssembly.Mast_Inst.12, 2
OnlyAssembly.Mast_Inst.12, 3
OnlyAssembly.Mast_Inst.12, 4
OnlyAssembly.Mast_Inst.12, 5
OnlyAssembly.Mast_Inst.12, 6
.
.
.
*BOUNDARY, TYPE=DISPLACEMENT, OP=NEW
**Fixed U2 dummy nodes
OnlyAssembly.Mast_Inst.81, 1, , 0.000379735
OnlyAssembly.Mast_Inst.81, 2, , 0
OnlyAssembly.Mast_Inst.81, 3, , 0
.
.
.
*****
*OUTPUT, FIELD
*NODE OUTPUT
U, RF
*ELEMENT OUTPUT, VARIABLE=ALL
S11, ESF1
*NODE PRINT, NSET=MAST_INST.CONTROLNODE, SUMMARY=NO, TOTALS=NO
RF
*NODE PRINT, NSET=MAST_INST.CONTROLNODE, SUMMARY=NO, TOTALS=NO
U
*NODE PRINT, NSET=MAST_INST.CONTROLNODE, SUMMARY=NO, TOTALS=NO
CF
*NODE PRINT, NSET=OnlyAssembly.Mast_Inst.U3dummy1, SUMMARY=NO, TOTALS=NO
RF
*NODE PRINT, NSET=OnlyAssembly.Mast_Inst.U3dummy2, SUMMARY=NO, TOTALS=NO
RF
*NODE PRINT, NSET=OnlyAssembly.Mast_Inst.U3dummy3, SUMMARY=NO, TOTALS=NO
RF
*RESTART, WRITE, NUMBER INTERVAL=1, TIME MARKS=NO, OVERLAY
*END STEP
```

Bibliography

[1] Able Engineering (2004a). Able ADAM articulated boom system. http://www.aec-able.com/Booms/adam.html.

[2] Able Engineering (2004b). Able Coilable booms. http://www.aec-able.com/Booms/coilboom.html.

[3] Benton, M. D. and J. William M. Robbins (1985, 15 July). Extendible structures. Patent no. 4599832.

[4] Billings, L., J. H. Curry, and V. Robins (n. d.). Relaxed Newton's method: an elementary example with complicated dynamics.

[5] Caltech (2011). Official NuSTAR homepage. http://www.nustar.caltech.edu/.

[6] Chapman, J. M. (1990). Nonlinear modeling of joint dominated structures. Technical report, Boeing Aerospace.

[7] Coppolino, R. N. and D. S. Adams (2004). Mid-frequency band dynamics of large space structures. In *49th International Symposium on Optical Science and Technology Annual Meeting*, Denver, CO.

[8] Douglas, M. V. (1993). Module for an articulated stowable and deployable mast. Patent no. 5267424.

[9] Duren, R. M. and C. C. Liebe (2001). The SRTM sub-arcsecond metrology camera. In *Aerospace Conference, IEEE Proceedings*, Volume 4, pp. 4/2037–4/2046.

[10] Duren, R. M. and E. F. Tubbs (2000). A modified commercial surveying instrument for use as a spaceborne rangefinder. In *IEEE Aerospace Conference*, Big Sky, Montana.

[11] Edeson, R., G. S. Aglietti, and A. R. L. Tatnall (2010). Conventional stable structures for space optics: The state of the art. *Acta Astronautica 66*, 13–32.

[12] Eiden, M., O. Brunner, and C. Stavrinidis (1987). Deployment analysis of the Olympus Astromast and comparison with test measurements. *Journal of Spacecraft 24*(1), 63–68.

[13] Fleischauer, P. D. (1997). Tribology in the space environment. Technical report, Space and Missile Systems Center, Air Force Materiel Command.

[14] Folkman, S. L., E. A. Roswell, and G. D. Ferney (1995). Influence of pinned joints on damping and dynamic behavior of a truss. *Journal of Guidance, Control, and Dynamics 19*(6), 1398–1403.

[15] Greschik, G. (2008). Truss beam with tendon diagonals: Mechanics and designs. *AIAA Journal 46*(3), 557–567.

[16] Greschik, G. and W. K. Belvin (2007). High-fidelity gravity offloading system for free-free vibration testing. *Journal of Spacecraft and Rockets 44*(1), 132–142.

[17] Gross, D. and D. Messner (1999). The Able deployable articulated mast - enabling technology for the shuttle radar topography mission. In *33rd Aerospace Mechanisms Symposium*, Volume NASA?CP-1999-209259, Pasadena, CA, pp. 15–30.

[18] Hardaway, L. M. R. and L. D. Peterson (2002). Nanometer-scale spontaneous vibrations in a deployable truss under mechanical loading. *AIAA Journal 40*(10), 2070–2076.

[19] Harrison, F. A., S. Boggs, F. Christensen, W. Craig, C. Hailey, D. Stern, W. Zhang, L. Angelini, H. An, V. Bhalereo, N. Brejnholt, L. Cominsky, W. R. Cook, M. Doll, P. Giommi, B. Grefenstette, A. Hornstrup, V. M. Kaspi, Y. Kim, T. Kitaguchi, J. Koglin, C. C. Liebe, G. Madejski, K. K. Madsen, P. Mao, D. Meier, H. Miyasaka, K. Mori, M. Perri, M. Pivovaroff, S. Puccetti, V. Rana, and A. Zoglauer (2010). The nuclear spectroscopic telescope array (NuSTAR). In *Proc. SPIE*, San Diego, California.

[20] Ingham, M. D. (1995). *Microdynamics and thermal snap response of deployable space structures*, Volume Masters thesis of *Aeronautics and Astronautics*. Cambridge, MA: Massachusetts Institute of Technology.

[21] Ingham, M. D., Y. A. Kim, E. F. Crawley, H. L. McManus, and D. W. Miller (1999). Experimental characterization of thermal creak response of deployable space structures. In *40th AIAA/ASME/AHS/ASC Structures, Structural Dynamics, and Materials Conference*, Volume AIAA-99-1269, St. Louis, MO, pp. 688–698.

[22] Kegg, C. M. (1988). Thermally stable deployable structure. In *The 22nd Aerospace Mechanisms Symposium*, NASA Langley Research Center, pp. 45–57.

[23] Koglin, J. E., C. H. Chen, J. C. Chonko, F. E. Christensen, W. W. Craig, T. R. Decker, C. J. Hailey, F. A. Harrison, C. P. Jensen, K. K. Madsen, M. J. Pivovaroff, M. Stern, D. L. Windt, and E. Ziegler (2004). Hard x-ray optics: From HEFT to NuSTAR. *Proc. SPIE 5488*, 856–867.

[24] Kwan, A. S. K. and S. Pellegrino (1994). Matrix formulation of macro-elements for deployable structures. *Computers and Structures 50*(2), 237–254.

[25] Kwok, K. and S. Pellegrino (2011). Viscoelastic effects in tape-springs. In *52nd AIAA/ASME/ASCE/AHS/ASC Structures, Structural Dynamics and Materials Conference*, Denver, CO.

[26] Lake, M. S., L. D. Peterson, and M. R. Hachkowski (1998). Research on the problem of high-precision deployment for large-aperture space-based science instruments. In *Space Technology and Applications International Forum*, Albuquerque, NM.

[27] Levine, M. B. (1999). On-orbit microdynamic behavior of a flexible structure: IPEX II. Technical report, Jet Propulsion Laboratory.

[28] Liebe, C. C., J. Burnham, R. Cook, B. Craig, T. Decker, D. I. Harp, B. Kecman, P. Meras, M. Raffanti, C. Scholz, C. Smith, J. Waldman, and J. Wu (2009). Metrology system for measuring mast motion on the NuSTAR mission. Technical report.

[29] Mallikarachchi, H. M. Y. C. and S. Pellegrino (2011). Quasi-static folding and deployment of ultrathin composite tape-spring hinges. *Journal of Spacecraft and Rockets 48*(1), 187–198.

[30] Marks, G. W., M. T. Reilly, and R. L. Huff (2002). The lightweight deployable antenna for the MARSIS experiment of the Mars Express spacecraft. In *36th Aerospace Mechanics Symposium*, Glenn Research Center.

[31] McEachen, M. (2011). Development of the GEMS telescope optical boom. In AIAA (Ed.), *52nd AIAA/ASME/ASCE/AHS/ASC Structures, Structural Dynamics and Materials Conference*, Denver, CO.

[32] McEachen, M. E., T. A. Trautt, and D. M. Murphy (2005). The ST8 SAILMAST validation experiment. In *46th AIAA/ASME/ASCE/AHS/ASC Structures, Structural Dynamics, and Materials Conference*, Austin, Texas.

[33] NASA (2005). Shuttle Radar Topography Mission. http://www2.jpl.nasa.gov/srtm/mast.html.

[34] Papadimitriou, C., M. Levine, and M. Milman (1998). Application of a finite element model updating methodology on the IPEX-II strucuture. In *16th International Model Analysis Conference*, pp. 952–958.

[35] Peek, R. and N. Triantafyllidis (1992). Worst shapes of imperfections for space trusses with many simultaneously buckling members. *International Journal of Solids and Structures 29*(19), 2385–2402.

[36] Pellegrino, S. (1990). Analysis of prestressed mechanisms. *International Journal of Solids and Structures 26*(12), 1329–1350.

[37] Pellegrino, S. (1993). Structural computations with the singular value decomposition of the equilibrium matrix. *International Journal of Solids and Structures 30*(21), 3025–3035.

[38] Pollard, B. D., E. Rodriguez, A. Kitiyakara, and T. Akins (n. d.). The wide swath ocean altimeter: Algorithm and technology developments for improved ocean topography measurements. Technical report, Jet Propulsion Laboratory.

[39] Pollard, B. D., E. Rodriguez, L. Veilleux, T. Atkins, P. Brown, A. Kitiyakara, M. Zawadski, S. Datthanasombat, and A. Prata, Jr. (2002). The wide swath ocean altimeter: Radar interferometry for global ocean mapping with centimetric accuracy. In *IEEE Aerospace Conference*.

[40] Press, W. H., B. P. Flannery, S. A. Teukolsky, and W. T. Vetterling (1986). *Numerical Recipes: The Art of Scientific Computing*. New York: Cambridge University Press.

[41] Seffen, K. A. and S. Pellegrino (1999). Deployment dynamics of tape springs. *Proc. R. Soc. Lond. A 455*, 1003–1048.

[42] Simulia (2007a). *Analysis User's Manual*, Volume IV: Elements. Dassault Systems.

[43] Simulia (2007b). *User Subroutines Reference Manual*.

[44] Smithsonian (2011). Space shuttle radar topography mission canister, antenna. http://www.nasm.si.edu/collections/artifact.cfm?id=A20040261000.

[45] Stohlman, O. R. and S. Pellegrino (2010). Shape accuracy of a joint-dominated deployable mast. In *51st AIAA/ASME/ASCE/AHS/ASC Structures, Structural Dynamics and Materials Conference*, Orlando, FL, pp. AIAA–2010–2605.

[46] Straubel, M., J. Block, M. Sinapius, and C. Hühne (2011). Deployable composite booms for various gossamer space structures. In *52nd AIAA/ASME/ASCE/AHS/ASC Structures, Structural Dynamics and Materials Conference*, Denver, CO.

[47] Tan, G. E. B. and S. Pellegrino (2008). Nonlinear vibration of cable-stiffened pantographic deployable structures. *Journal of Sound and Vibration 314*, 783–802.

[48] Timoshenko, S. P. and D. H. Young (1965). *Theory of Structures* (Second ed.). New York: McGraw-Hill Book Company.

[49] Umland, J. W. (2001). SRTM mast damping subsystem design and failure investigation. In *35th Aerospace Mechanisms Symposium*, Ames Research Center.

[50] Warren, P. A., L. D. Peterson, and J. D. Hinkle (1999). Submicron mechanical stability of a prototype deployable space telescope support structure. *Journal of Spacecraft and Rockets 36*(5), 765–771.

[51] Williams, J. A. (1994). *Engineering Tribology*. New York: Oxford University Press.

[52] Wong, E., W. Breckenridge, D. Boussalis, P. Brugarolas, D. S. Bayard, J. Spanos, and G. Singh (2001). Post-flight attitude reconstruction for the shuttle radar topography mission. In *AAS/AIAA*, Quebec City.